Two pion correlations at the STAR experiment

Dissertation
zur Erlangung des Doktorgrades
der Naturwissenschaften

vorgelegt beim Fachbereich Physik
der Johann Wolfgang Goethe − Universität
in Frankfurt am Main

von
Dominik Bernhard Flierl
aus Blieskastel

Frankfurt am Main 2002
(DF1)

Vom Fachbereich Physik der Johann Wolfgang Goethe−Universität
als Dissertation angenommen

Dekan: Prof. Dr. Horst Schmidt−Böcking

Gutachter: Prof. Dr. Reinhard Stock

Prof. Dr. Herbert Ströbele

Datum der Disputation: 4. April 2003

Zusammenfassung

Die Physik beschäftigt sich seit jeher mit der Frage nach dem Aufbau und der Struktur der Materie. Die Antworten änderten sich im Laufe der Zeit, der gegenwärtige Stand der Erkenntnis ist im sogenannten Standardmodell zusammengefasst. Dort werden die Elementarteilchen in Leptonen und Quarks unterteilt, die Wechselwirkungen zwischen ihnen beschreibt man durch vier fundamentale Kräfte: die Gravitation, die elektromagnetischen Kraft, die schwache und die starke Kernkraft.

Gemäß dem Standardmodell sind Nukleonen, also Protonen und Neutronen, aus Quarks aufgebaut. Das Proton ist beispielsweise ein gebundener Zustand aus zwei up und einem down Quark. Die Nukelonen bilden ihrerseits die Atomkerne, welche die Systematik der Elemente bestimmen.

Quarks treten in sechs verschiedenen Arten (flavours) auf: up, down, strange, charm, bottom und top. Freie Quarks konnten bislang nicht nachgewiesen werden, sie werden nur als Quark−Antiquark Paar (Meson) oder als Kombination aus drei Quarks (Baryon) beobachtet. Mesonen und Baryonen werden unter dem Begriff Hadronen zusammengefaßt.

Die starke Kernkraft beruht letztlich auf der Wechselwirkung zwischen Quarks, diese wird durch die Quantenchromodynamik (QCD) beschrieben. Ähnlich der Glashow−Salam−Weinberg Theorie (GSW), die die elektromagnetische und die schwache Kernkraft beschreibt, ist die Quantenchromodynamik durch Austauschteilchen charakterisiert. Im Fall der GSW wurden die Photonen bzw. $W^{\pm}$ oder Z−Teilchen als Austauschteilchen identifiziert, in der QCD fungieren Gluonen als Austauschteilchen. Photonen vermitteln die elektromagnetische Kraft zwischen allen Teilchen, die elektrische Ladung tragen. Analog wirkt die Kraft, die durch den Austausch von Gluonen beschrieben wird, zwischen Teilchen, die eine Farbladung tragen. Anders als das neutrale Photon trägt das Gluon selbst Farbe und wechselwirkt daher mit anderen Teilchen, die Farbe tragen. Dieser Umstand zeigt bereits, dass in der QCD ganz andere Phänomene zu erwarten sind als in der GSW.

Die Tatsache, dass Quarks nur in gebundenen Zuständen vorliegen, erschwert die direkte Beobachtung der Wechselwirkung zwischen ihnen. Ein indirekter Weg, um die Wirkungweise diese Kraft zu untersuchen, liegt in der Erzeugung hoher Kernmateriedichten und hoher Kerntemperaturen. Die Idee besteht darin, das Phasendiagramm von Kernmaterie experimentell zu bestimmen (Abbildung 1.3) und dann auf die zugrundeliegende Kraft zu schließen. Unter anderem führen die Kräfte, die zwischen den Einzelteilchen des Mediums herrschen, zu charakteristischen Phasenübergängen. Im Fall der Kernmaterie hofft man insbesondere, den Übergang von gebundenen Zuständen in eine Quark−Gluon−Plasma Phase (QGP), in der sich Quarks und Gluonen frei bewegen, zu beobachten.

Zwei prominente Beispiele demonstrieren, warum die Eigenschaften dieses Materiezustandes − und ob er überhaupt existiert − auch für andere Teilgebiete der Physik von großem Interesse sind. Zum einen geht man davon aus, dass in der Frühphase des Universums, 10^{-12} s nach dem Urknall, die Energiedichte so hoch war,

dass die Materie in einem Plasmazustand vorlag. In diesem Bild führt die Expansion des Raumes zu einer Abkühlung des Plasmas und schließlich zum Ausfrieren in Hadronen. Zum anderen zeigen viele Modellstudien, dass im Innern von Neutronensternen mit extremen Dichten zu rechnen ist. Unter Umständen werden Energiedichten erreicht, die hoch genung sind, um einen Phasenübergang in ein Quark Gluon Plasma zu erzwingen. Die Beschreibung dieser astronomischen Objekte setzt somit auch die Kenntnis der Kräfte zwischen den Quarks voraus.

Der einzige Weg, dichte Kernmaterie im Labor zu erzeugen, stellen Schwerionenreaktionen dar. Wenn zwei ultrarelativistische schwere Kerne zentral kollidieren, entsteht für kurze Zeit eine Region hoher Energiedichte (Abbildung 1.1). QCD−Gitter−Rechnungen deuten darauf hin, dass die Dichte, die man in Schwerionreaktion gegenwärtig erreicht, hoch genung ist, um einen Übergang der Kernmaterie in eine Plasma−Phase zu erzwingen. Aufgrund des hohen Drucks expandiert die verdichtete, heiße Kernmaterie in longitudinaler (entlang des Strahls) und transversaler (senkrecht zum Strahl) Richtung und die Dichte nimmt ab. Vorausgesetzt am Anfang der Reaktion wurde ein Quark−Gluon−Plasma erzeugt, dann friert diese Phase in Hadronen aus (chemisches Ausfrieren), wenn Dichte und Temperatur einen kritischen Wert unterschreiten. Die erzeugten Hadronen wechselwirken zunächst noch elastisch miteinander, d.h. die Impulse der Teilchen ändern sich, die Identität der Teilchen bleibt jedoch erhalten. Schließlich enden auch diese Wechselwirkungen (thermisches Ausfrieren), und die Teilchen verlassen die Reaktionszone (Abbildung 1.4).

Der Ablauf einer solchen Schwerionenreaktion dauert einige 10^{-23}s und ihre räumliche Ausdehnung liegt in der Größenordnung von 10^{-15}m, damit ist die Reaktion selbst nicht beobachtbar. Nur der Endzustand, also die Identitäten und Impluse der emittierten Teilchen, kann bestimmt werden. Um den Ablauf der Reaktion zu rekonstruieren, ist man daher auf Modellrechnungen angewiesen. Aufgrund dieser Modellrechnungen wurden einige Observablen vorgeschlagen, die einen Phasenübergang kennzeichnen. Neben anderen Signaturen führt ein Phasenübergang wahrscheinlich zu einer verlängerten Emissionsdauer. Dieser Effekt kann möglicherweise durch die Analyse von Zwei−Teilchen−Korrelationen sichtbar gemacht werden. Ganz allgemein stellt die Untersuchung von Teilchenkorrelationen die einzige Möglichkeit dar, die raum−zeitlichen Strukturen während des thermischen Ausfrierens experimentell zu bestimmen.

Korrelationen zwischen Teilchen, die von einer hinreichend kleinen Quelle emittiert werden, haben verschiedene Ursachen. Betrachtet man beispielsweise die Häufigkeitsverteilung der Impulsdifferenz zwischen zwei elektrisch gleich geladenen Teilchen, so stellt man fest, dass Paare mit geringer Impulsdifferenz weniger häufig vorkommen, als man anhand der Ein−Teilchen Impulsverteilung vorhersagen würde. Dieser Effekt ist auf die Abstoßung zwischen zwei elektrisch gleich geladenen Teilchen zurückzuführen, die mit kleiner Impulsdifferenz emittiert wurden.

Eine weniger offensichtliche Korrelation wird durch den Quantencharakter identischer Teilchen verursacht. Zwei identische Bosonen, die im Phasenraum nahe beieinander liegen, können gemäß den Prinzipien der Quantentheorie nicht unterschieden werden. Die Wellenfunktion, die diesen Zwei−Teilchen−Zustand beschreibt, muß beim Vertauschen der Teilchen erhalten bleiben.

Diese Forderung führt zu einem Interferenzterm in der Zwei−Teilchen

Intensitätsverteilung. Diese Verteilung ist proportional zur Wahrscheinlichkeit, ein Teilchenpaar mit der Impulsdifferenz q zu messen. Berechnet man die Impulsdifferenzverteilung von Pionenpaaren und berücksichtig nur quanten−statistische Effekte, so findet man, dass Paare mit geringem Impulsunterschied bis zu zweimal häufiger vorkommen, als man aufgrund einfacher statistischer Überlegungen erwarten würde. Um diesen Effekt experimentell sichtbar zu machen, konstruiert man die Korrelationsfunktion, die die gemessene Impulsdifferenzverteilung in Relation zu einer Untergrundverteilung setzt. Experimentell gewinnt man diese Referenzverteilung, indem Paare aus Spuren aus verschiedenen Ereignissen gebildet werden. Die Referenzverteilung entspricht damit der Verteilung, die man messen würde, wenn die Teilchen nicht der Quantenstatistik unterlägen. Die Korrelationsfunktion wird im allgemeinen durch eine Gauß−Funktion angenähert. Das Inverse der Standardabweichung dieser Funktion wird nach den Pionieren der Intensitätsinterferometrie R. Hanbury Brown und R. Twiss als HBT−Radius bezeichnet.

Teilchen interferieren nur dann, wenn sie im Phasenraum nahe beieinander liegen, das heißt sowohl die Impulsdifferenz als auch der räumliche Abstand muß hinreichend klein sein. Diese Bedingung kann genutzt werden, um von der gemessenen Korrelationsfunktion, die nur auf den Impulskomponenten basiert, auf die räumliche Verteilung der Teilchenproduktion zu schließen. Eine detaillierte Betrachtung erlaubt sogar, aufgrund der gemessenen Korrelationsfunktion quantitative Aussagen über die räumlichen Aspekte der Teilchenquelle zu machen. Beispielsweise können im Rahmen eines Modells die Stärke der transversalen Expansion oder die Emissionsdauer in Relation zu den HBT−Radien gesetzt werden. In Kapitel 2 sind die Grundlagen der Teilcheninterferometrie ausführlicher dargestellt.

Der eigentliche Gegenstand dieser Arbeit ist experimentelle Analyse der Zwei−Teilchen−Korrelationen in einer Schwerionenreaktion. Dazu wird zunächst in Kapitel 3 das STAR Experiment am RHIC vorgestellt, in dem die Daten aufgezeichnet wurden, die Grundlage dieser Analyse sind.

Am RHIC−Beschleuniger am BNL in den USA werden AuAu Kollisionen bis zu einer Schwerpunktsenergie von $\sqrt{S_{NN}} = 200\,\mathrm{GeV}$ erzeugt. Figur 3.1 zeigt den Beschleuniger−Ring und die vier Experimente Brahms, Phenix, Phobos und STAR. Der hier analysierte Datensatz wurde bei der Datennahme im Jahr 2000 aufgezeichnet. Zu dieser Zeit wurde am RHIC eine Schwerpunktsenergie von $\sqrt{S_{NN}} = 130\,\mathrm{GeV}$ erreicht.

Bei einer zentralen AuAu Kollision werden mehrere Tausend Teilchen produziert. Der STAR Detektor ist dafür konzipiert, hadronische Teilchen kleiner Rapidität (d.h. großer Winkel zur Strahlachse) zu messen, innerhalb der Akzeptanz werden etwa 80% der produzierten geladenen Teilchen nachgewiesen. Der schematische Aufbau des STAR Detektorsystems ist in Figur 3.2 dargestellt. Der zentrale Detektor ist eine TPC (Zeit−Projektions−Kammer). Dieser Detektor basiert darauf, dass geladene Teilchen beim Durchgang durch ein Messgas eine Spur von Ionen hinterlassen. Ein starkes elektrisches Feld driftet die Elektronen, die bei den Ionisationsprozessen freigesetzt wurden, zu einer Ausleseebene. Der Punkt, an dem die Elektronen auf der Ausleseebene ein Signal erzeugen, entspricht der Projektion des Ionisationpunktes auf die Ausleseebene. Die dritte Komponente, die den Raumpunkt der Ionisation festlegt, ist durch die Driftzeit bei bekannter Driftgeschwindigkeit gegeben. So erscheint eine

Teilchenspur als eine Kette von Ionisationspunkten im Detektorgas. Ein magnetisches Feld parallel zur Strahlachse führt zu einer Ablenkung der geladenen Teilchen. Die Krümmung der Spur ist dabei umgekehrt proportional zum transversalen Impuls. Abbildung 3.6 zeigt ein typisches Ereignis mit etwa 10^5 Ionisationspunkten und den entsprechenden Teilchenspuren.

Der spezifische Energieverlust eines Teilchens beim Durchgang durch das Messgas hängt von seinem Impuls und seiner Masse ab. Die Stärke des auf der Ausleseebene induzierten Signals erlaubt den spezifischen Energieverlust zu bestimmen. Da der Impuls durch die Krümmung der Spur bekannt ist, kann so die Masse und damit die Identität des Teilchens bestimmt werden (siehe Abbildung 3.7).

In Kapitel 4 wird der Datensatz beschrieben, der als Grundlage für diese Analyse dient. Während der Datennahme werden die digitalisierten Daten der TPC auf ein Speichermedium geschrieben. Der erste Schritt bei der Rekonstruktion der Ereignisse besteht darin, die Ionisationspunkte zu lokalisieren. Dies leistet der Clusterfinder−Algorithmus, der in Kapitel 4.1.1 beschrieben ist. Die Spurpunkte werden dann durch den Tracking−Algorithmus zu Teilchenspuren verbunden. Die erreichte Effizienz, Akzeptanz und Impulsauflösung der Rekonstruktion sind in Kapitel 4.1.2 zusammengefaßt.

Die Zwei−Teilchen−Korrelationen werden nur für zentrale Kollisionen betrachtet, das sind Ereignisse mit kleinem Stoßparameter. Die Multipliztät der gemessenen Spuren ist in erster Näherung ein Maß für die Zentralität des Ereignisses. Für diese Analyse werden nur die 12% zentralsten Ereignisse zugelassen. Die Selektion der Ereignisse ist in Kapitel 4.2 beschrieben.

Die Auswahl der Spuren, die in der Analyse verwendet werden, ist in Kapitel 4.3 beschrieben. Es werden nur Spuren zugelassen, deren Impulse in einem Bereich hinreichend hoher Akzeptanz und Effizienz liegen. Außerdem werden die Spuren ausgewählt, die mit hoher Wahrscheinlichkeit von Pionen stammen.

Eine weitere Auswahl wird auf der Paarebene getroffen. Die Korrelationsfunktion wird in einzelnen Intervallen transversalen Paarimpulses k_t und Paarrapidität $Y_{\pi\pi}$ gebildet. Damit kann die Abhängigkeit der HBT−Radien von diesen Größen dargestellt werden.

Zwei weitere Auswahlkriterien sollen die Qualität der Spurpaare garantieren. Zum einen werden solche Paare verworfen, die im Detektor zu nahe beieinander liegen. Für die HBT−Analyse sind Paare mit geringem Impulsunterschied entscheidend, ein geringer Impulsunterschied heißt notwendigerweise, dass die Spuren räumlich nicht sehr weit getrennt sind. Wenn die Spuren aber zu nahe liegen, können sie vom Detektor und von der Rekonstruktionskette nicht mehr aufgelöst werden. Damit verliert man einen Teil der Paare in der Signalverteilung, nicht aber in der Untergrundverteilung, da in diesem Fall die endliche Zwei−Spur−Auflösung keine Rolle spielt. Um die Korrelationsfunktion nicht durch einen Detektoreffekt zu verfälschen, entfernt man die Paare, die im Detektor nahe beieinander liegen, sowohl in der Signal− als auch in der Untergrundverteilung. Ein weiteres Problem stellen "gebrochene" Spuren dar. In einigen Fällen wird eine Teilchenspur von der Rekonstruktionskette nicht als Ganzes erkannt, vielmehr werden zwei Spurstücke im Dektor gefunden. Da diese Spurstücke vom selben Teilchen stammen, haben sie eine sehr geringe Impulsdifferenz. Diese Paare können anhand ihrer Topologie im Detekor

erkannt werden. Wie im Fall der begrenzten Zwei−Spur−Auflösung werden sie sowohl für die Signal− als auch für die Untergrundverteilung nicht zugelassen.

In Kapitel 5 werden schließlich die Ergebnisse der Korrelationsanalyse dargestellt. Die Korrelationsfunktion wird in verschiedenen Parametrisierungen betrachtet. In der einfachsten Form betrachtet man nur den Betrag des Impulsdifferenzvektors. Dieser Ansatz bedeutet aber, dass der entsprechende HBT−Radius alle Raum−Zeit Komponenten mischt und damit nur wenig Aussagekraft bezüglich der Quellfunktion besitzt. Eine differenzierte Analyse in drei unabhängigen Komponenten ermöglichen die Pratt−Bertsch (PB) und die Yano−Koonin−Podgoretskii (YKP) Parametrisierung. Die beiden Parametrisierungen unterscheiden sich in der Zerlegung des Impulsdifferenzvektors in drei unabhängige Komponenten. Im ersten Fall bezeichnet man die Komponenten als q_{out}, q_{long} und q_{side}, im zweiten Fall als q_{para}, q_{perp} und q_0 (Kapitel 2.7 und 2.8). Die entsprechenden Korrelationsfunktionen sind in Gleichung 2.31 bzw. 2.34 gegeben. Die jeweiligen HBT−Radien R_{out}, R_{long} und R_{side} bzw. R_{para}, R_{perp} und R_0 können in Relation zu den Parametern der Quellfunktion (Gleichung 2.43) gesetzt werden. Die beiden Parametrisierungen liefern im Prinzip die gleiche Information und die beiden Sätze von HBT−Radien können in Beziehung zueinander gesetzt werden (Gleichung 2.41). Beispielsweise entspricht der HBT−Radius R_0 in der YKP−Parametrisierung in erster Näherung der Emissionsdauer, während in der PB−Parametrisierung diese Größe Verhältnis von R_{out} zu R_{side} abhängt. Zusätzlich zu den Radien enthält die YKP−Parametrisierung einen Parameter β, der erlaubt, die longitudinale Geschwindigkeit des betrachteten Quellelementes zu bestimmen.

Die Abbildungen 5.7 bis 5.10 zeigen die HBT−Radien beider Parametrisierungen in Abhänigigkeit vom transversalen Paarimpuls k_t und von der Paarrapidität $Y_{\pi\pi}$. Die Größe der gemessenen Radien bewegt sich zwischen 3 und 7 fm. Nur der Radius R_0 verschwindet in den meisten k_t−$Y_{\pi\pi}$ Intervallen. Die anderen Radien nehmen mit steigendem k_t ab und sind unabhängig von $Y_{\pi\pi}$. Abbildung 5.11 demonstriert, dass die beiden Parametrisierungen −dort wo sie vergleichbar sind− konsistente Ergebnisse liefern.

Eine Diskussion der Ergebnisse schließt sich in Kapitel 6 an. Die Abhänigigkeit des Parameters β von $Y_{\pi\pi}$ zeigt eine starke longitudinale Expansion an. Ein ähnliches Verhalten wurde bei niedrigeren Schwerpunktsenergien beobachtet, wo man allerdings eine schwächere longitudinale Expansion erwarten würde.

Die Lebensdauer der Quelle, also die Zeit vom anfänglichen Überlapp der Kerne bis zum thermischen Ausfrieren, bestimmt die k_t−Abhänigigkeit des Parameters R_{long}. Dieser Zusammenhang wurde von Mahklin und Sinyukow formuliert, eine Anpassung der entsprechenden Funktion an die gemessene k_t Abhänigigkeit von R_{long} ergibt eine Lebensdauer von etwa 8 fm/c bei einer Ausfriertemperatur von etwa 126 MeV. Entsprechende Messungen bei niedrigeren Kollisionsenergien lieferten ähnliche Resultate.

Die k_t−Abhängigkeit des Parameters R_{side} ist mit der Stärke der transversalen Expansion gemäß Gleichung 6.3 verknüpft. Da die Relation nicht eindeutig ist, muß entweder eine feste Ausfriertemperatur angenommen werden oder es werden gleichzeitig Einteilchenspektren betrachtet, um die Mehrdeutigkeit zu eliminieren. Eine vorläufige Abschätzung ergibt eine mittlere transversale Expansions−geschwindigkeit von $v_\perp \approx 0.6$ und einen gemetrischen Radius von $R_G \approx 7.4\,\mathrm{fm}$.

Auch diese Ergebnisse sind vergleichbar mit entsprechenden Resultaten bei niedrigeren Kollisionsenergien.

Ein weiterer Parameter der Quellfunktion ist die Emissionsdauer. Die Pionen werden nicht zu einem festen Zeitpunkt emittiert, man geht vielmehr davon aus, dass die Zeitpunkte der letzten elastischen Wechselwirkung in der Quelle gaußförmig verteilt sind. Den Mittelwert dieser Verteilung bezeichnet man als Lebensdauer der Quelle, die Breite als Emissionsdauer. Entsprechend Gleichung 6.4 bzw. 6.5 ist die Emissionsdauer mit dem Radius R_0 bzw. dem Verhältnis R_{out} zu R_{side} verbunden. Wie in Abbildung 5.8 ersichtlich verschwindet der Parameter R_0 , außer im kleinsten k_t Intervall. Dies entspricht in der PB−Parametrisierung der Tatsache, dass das Verhältnis R_{out} zu R_{side} bei hohen k_t kleiner als eins ist. Diese Resultate sind nicht vereinbar mit herkömmlichen Modellen. Insbesondere weil eine verlängerte Emissionsdauer als Signatur für die Bildung eines Quark−Gluon−Plasmas vorgeschlagen wurde, wird dieses Ergebnis derzeit intensiv diskutiert.

Die Ergebnisse dieser Analyse sind sowohl mit bereits publizierten Daten der STAR Kollaboration als auch mit Resultaten von anderen RHIC Experimenten verträglich (siehe Abbildung 6.8).

In Abbildung 6.9 ist die Abhängigkeit der HBT−Radien von k_t bei verschiedenen Schwerpunktsenergien dargestellt. Im Gegensatz zu vielen anderen Observablen ändern sich die HBT Radien nur geringfügig. Da man erwartet, dass die Reaktion bei hohen Energien vollkommen anders abläuft, würde man auch davon ausgehen, dass sich die Ausfrierbedingungen ändern. Dass dies nicht in den Zwei−Teilchen−Korrelationen sichtbar wird, deutet darauf hin, dass die Näherungen die notwendig sind, um die gemessenen Radien mit Modellparametern zu verbinden, nicht gültig sind.

Die Systematik der HBT Parameter als Funktion der Schwerpunktsenergie enthält damit keinen direkten Hinweis, dass die kritische Energiedichte überschritten wurde, ab der die Kernmaterie in einer Plasmaphase vorliegt. Andererseits werden weder die verschwindende Emissionsdauer noch die Tatsache, dass die anderen HBT−Parameter sich nur wenig mit der Schwerpunktsenergie ändern, als Argument dafür gewertet, dass die kritische Energiedichte nicht überschritten wurde. Die Frage, ob ein Quark−Gluon−Plasma im Labor erzeugt und analysiert werden kann, bleibt damit offen. Das thermische Ausfrieren einer Pionenquelle scheint hingegen anders zu verlaufen, als bisher angenommen wurde.

Systematische Studien der Korrelationsfunktion in AA Kollisionen am RHIC in Kombination mit Fortschritten im theoretischen Verständnis der Teilcheninterferometrie in Schwerionenreaktion werden in Zukunft hoffentlich erlauben, die gemessenen Radien in ein konsistentes Bild einzuordnen.

In zukünftigen Experimenten am LHC werden noch weit höhere Dichten erreicht als bisher, damit sollten sich auch die Ausfrierbedingungen stark verändern. Es wird sich dann zeigen, ob die Teilcheninterferometrie das geeignete Instrument ist, um die Quellfunktion einer Schwerionenreaktion zu messen.

Contents

1. Introduction 10

1.1 The standard model..... 10
1.2 The strong force in nuclear matter..... 11
1.3 Particle interferometry..... 14
1.4 Notation..... 15
1.5 Content and structure of this thesis..... 16

2. HBT..... 17

2.1 Historical overview..... 17
2.2 The two particle correlation function..... 18
2.3 Sources of particle correlations..... 19
2.4 Bose Einstein correlations..... 20
2.5 Classical current formalism..... 22
2.6 Approximating the emission function..... 24
2.7 Pratt−Bertsch parametrization..... 25
2.8 Yano−Koonin−Podgoretskii parametrization..... 28
2.9 PB versus YKP parametrization..... 30
2.10 Collective expansion and k_t dependence of HBT radii..... 31
2.11 Coulomb correction..... 32

3 The STAR experiment..... 34

3.1 The Relativistic Heavy Ion Collider (RHIC)..... 34
3.2 The Solenoidal Tracker at RHIC (STAR)..... 36
3.3 The Time Projection Chamber (TPC)..... 38
3.4 Particle Identification..... 43

4. Experimental data set..... 45

4.1 Event reconstruction..... 45

4.1.1 Cluster finding..... 46

4.1.2 Tracking..... 49

4.2 Event selection..... 52

4.3 Track selection..... 55

4.4 Pair selection..... 59

4.4.1 Entrance separation cut..... 60

4.4.2 Split track cut..... 61

4.5 Construction of the correlation function..... 63

5. Experimental results..... 64

5.1 One dimensional correlation functions..... 64

5.2 Fitting three dimensional correlation functions..... 66

5.3 Systematical uncertainties..... 69

5.4 Momentum resolution correction..... 71

5.5 Results for the YKP parametrization..... 74

5.6 Results for the PB parametrization..... 78

5.7 Consistency of PB and YKP parametrization..... 81

6. Discussion..... 82

6.1 Dependencies of HBT parameters on $Y_{\pi\pi}$ 82

6.2 Life time of the source..... 84

6.3 Transverse expansion..... 86

6.4 Emission duration..... 88

6.5 Comparison to published results from RHIC..... 92

6.6 HBT radii from AGS to RHIC..... 94

6.7 Final considerations..... 96

7. Conclusion and outlook..... 97

8. Appendix.....99

Appendix A..... 100

Appendix B..... 104

9. Bibliography.....109

1.Introduction

1.1 The standard model

Since the beginnings of science, the structure of matter itself has been the subject of physical questions: what is it made of, is there a smallest entity, which cannot further be dismanteld ? The answers have changed with time, first atoms were identified as the fundamental components, then it was realised that they themselves were made up out of protons and neutrons forming a nucleus surrounded by a cloud of electrons.

It was not until the 1970s when the picture was established, that we now call our standard model, with quarks and leptons being the fundamental constituents and with four forces acting between them: the strong, the weak, the electromagnetic and the gravitational force [Hoo96].

All particles obey the gravitational force, but in comparison it is by far the weakest and thus only visible when the others vanish. Nevertheless gravitation plays a unique role in physics, it is described by the general theory of relativity [Mis73].

The electromagnetic force acts between all objects carrying electric charge: e.g. quarks and electrons. The fundamental relations that describe electromagnetic phenomena are given by the famous Maxwell equations [Jac62][Fey88].

The weak force is closely related to the electromagnetic force, but it acts on all leptons and quarks. It was discovered that both forces are indeed different aspects of a single electroweak interaction. This unification is called **G**lashow−**S**alam−**W**einberg theory (GSW). Its predictions led to the observation of the $W^{\pm}$ and Z^{0} particles at CERN (**C**onseil **E**uropéen pour la **R**echerche **N**ucléaire) in 1983 [Arn83]. Its success in describing and predicting experimental measurements strongly supported the idea that all theories of fundamental interactions should have the same mathematical structure: they should be renormalizable gauge theories.

Therefore the theory of the strong force was formulated as the renormalizable gauge theory of **Q**uantum **C**hromo **D**ynamics (QCD) [Gre89]. The strong force acts only on constituents carrying color charge, like quarks. Within a nucleon it is the dominant force and its features determine mainly the characteristics of nuclear matter. And vice versa it is the study of nuclear matter that can reveal how this interaction works.

In general, the character of a force is reflected in the qualities of its interaction particle, e.g. the electromagnetic force interacts via the neutral and massless photon whereas the weak force is mediated by the $W^{\pm}$ and Z^{0} particles. The strong force is transmitted via gluons, which themselves carry color charge and thus interact strongly. This feature is one reason why QCD is more complicated than GSW. In fact after a long time of intense study, QCD has shown to be very complex in both its experimental and its theoretical aspects.

Nevertheless QCD is currently the most promising approach to the understanding of the strong force. Neighboring fields like astrophysics will be affected by any progress in understanding and verifying QCD: questions to the evolution of the early universe or to the composition of a neutron star cannot be answered without detailed knowledge of the equation of state of matter; which itself is closely linked to the interaction between the fundamental constituents of matter.

1.2 The strong force in nuclear matter

All common nuclei are built from protons and neutrons which themselves are composed of quarks. So far no isolated quarks have been observed; they are always confined in color neutral entities called hadrons. Either a quark and an antiquark form a meson like the pion, or three quarks form a baryon like the proton. The strong force binding those quarks is such, that even in the middle of a nucleus, in the immediate vicinity of many color charged objects, the protons and neutrons do not loose their identity. The fact, that the density stays constant from light nuclei like oxygen to very heavy like lead, indicates, that quarks confined in a nucleon form a very stable and hard object.

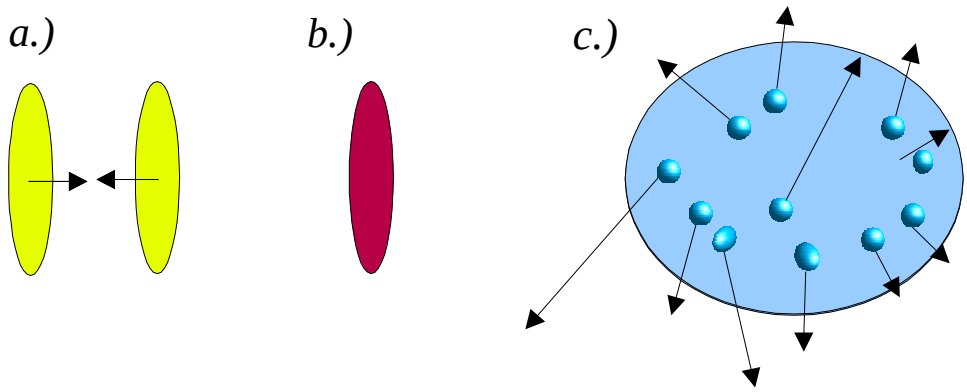

Figure 1.1

Main stages of a nucleus−nucleus collision:

a.) Two colliding lorentz contracted relativistic nuclei.

b.) The highest energy density is reached when they overlap completely.

c.) A multitude of particles is created which finally hit the detectors.

To probe the complex structure of nuclei one bombards them with pointlike entities, e.g. electrons, to observe single fundamental interactions. Another approach is to study the conditions of nuclear matter in nucleus−nucleus collisions. The main steps

of such an event are sketched in figure 1.1. The final state of such a collision is the result of a multitude of particle interactions. The number of participating entities and interactions between them is large enough to allow the use of the terminology of thermodynamics. Size and kinetic energy of the accelerated nuclei determine the initial conditions of the hot and dense state of matter which is created when they collide.

Low beam energies $\left(\sqrt{S_{NN}} \approx 0.100\,\mathrm{GeV}\right)$ lead only to a temperature of 10−20 MeV and a slight compression of the nuclear matter. With ultra relativisic beams, i.e. $\sqrt{S_{NN}} > 10\,\mathrm{GeV}$, the initial density is several times larger than the normal nuclear density and temperatures are well above 100 MeV [Cse94].

The energy density reached in collisions of ultra relativistic heavy ions might even be high enough to force a transition from regular confined matter into a plasma phase: the Quark Gluon Plasma (QGP). Within this phase, quarks no longer belong to a single hadron, they will rather be deconfined and interact with surrounding quarks and gluons. This transition has been already predicted in the 1970s [Shu80] and it is supported by current theoretical QCD studies [Kar01].

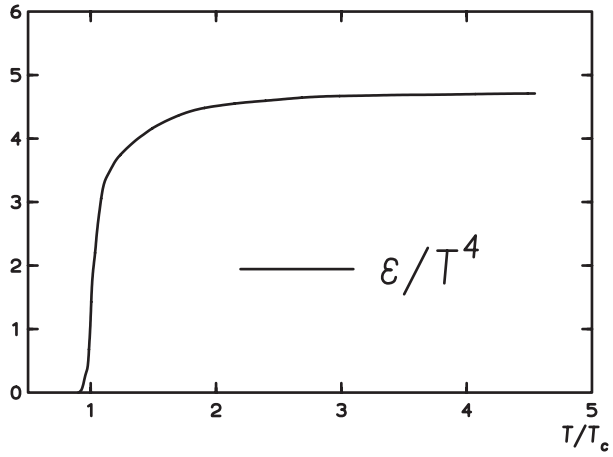

Figure 1.2

If the temperature T of nuclear matter exceeds a certain critical value T_C lattice calculations predict a steep rise in the energy density ϵ : a typical phase transition [Kar01].

The number of degrees of freedom in a QGP (~37) is much higher than in a hadron gas phase (~3), therefore a typical behaviour of thermodynamical variables should indicate a possible phase transition (see figure 1.2). Details of the nature of the transition, e.g. of which order it is, and the characteristics of the new phase, e.g. whether the chiral symmetry is restored, are still discussed [Bla99].

Most of the interactions occuring during the expansion of the highly compressed hadronic matter, created in an heavy ion collision, are associated with relatively small momentum transfers. This kind of process cannot be calculated analytically or using pertubative methods. The most promising approach is lattice QCD [Cre86] where the continuous space−time is approximated by a discrete lattice. Even though these

calculations are still restricted by numerical constraints, they yield quantitative results like the critical temperature, where the phase transition occurs. Recent lattice QCD calculations [Kar01] confirm that a transition should be observed at energy densities reached with today's accelerator facilities.

Thermodynamical variables, like energy density or pressure of hot and dense matter created in an heavy ion collision, are not directly accessible. Most of the observables stem from later stages of the collision when the matter has already cooled down during its expansion into the surrounding vacuum. With the help of phenomenological models it is possible to associate the detected particles with a thermodynamical state and to extrapolate from there to earlier stages of the reaction. The thermodynamical conditions established with the different initial conditions at various experiments are shown in figure 1.3.

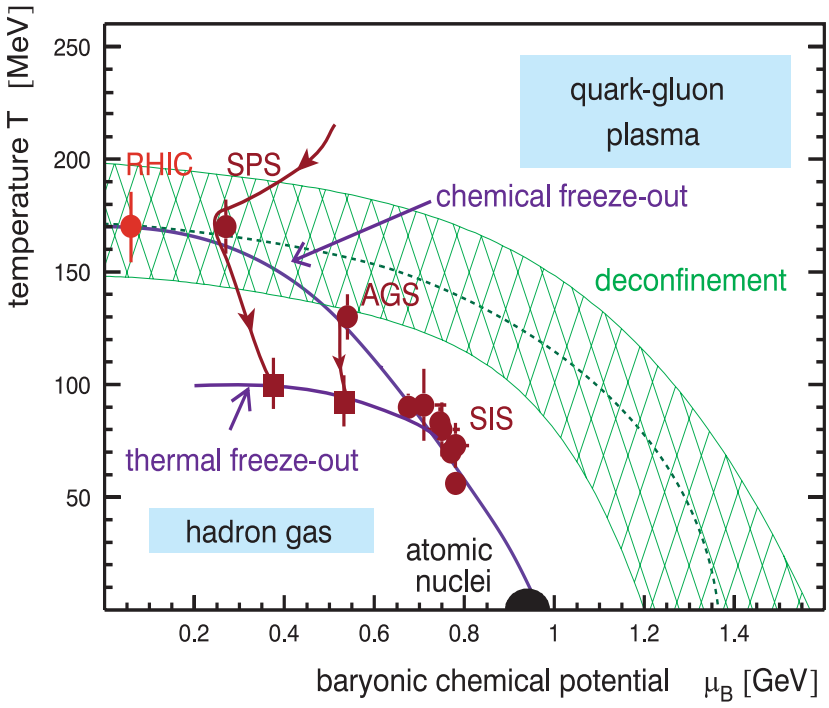

Figure 1.3

The thermodynamical conditions of nuclear matter created in experiments at various accelerator facilities (SIS, AGS, SPS, RHIC) [Bra01]. High initial energy density leads to a plasma phase which hadronizes during the chemical freeze out. The hadron gas expands further until the particles leave the reaction volume and stop interacting with each other. This stage is called thermal freeze out.

Because such a phase transition should be a rather dramatic event it will probably leave measurable traces. Consequently many signatures have been proposed and were experimentally verified [Bas99]. It turned out however that no single observable is sensitive enough to provide evidence for a new state of matter. Only the complete picture of a heavy ion collision based on various measurements from different experiments allows a convincing conclusion. After serveral years of intense studies at the CERN SPS facility strong evidence has been collected to announce that most

likely a new state of matter was observed at a collision energy of $\sqrt{S_{NN}} = 17\,\mathrm{GeV}$ [Hei00].

The kinetic energy of the colliding nuclei and therefore also the initial energy density reached at SPS is much lower than at the **R**elativistic **H**eavy **I**on **C**ollider (RHIC) at Brookhaven where a maxium of $\sqrt{S_{NN}} = 200\,\mathrm{GeV}$ is achieved. The hope with this new facility, dedicated to study heavy ion collisions, is not only to observe the transition, but to study the characteristics of the QGP phase. Eventually only probing nuclear matter at various energy densities will yield the phase diagram which is necessary to formulate the equation of state of nuclear matter.

1.3 Particle interferometry

A QGP phase does not survive in vacuum: it will rather expand and freeze out into hadrons, this stage of the reaction is labeled chemical freeze out or hadronization. Due to the initial pressure the resulting hadron gas expands further and density and temperature drop until the particles stop interacting: this final step is called thermal freeze out.

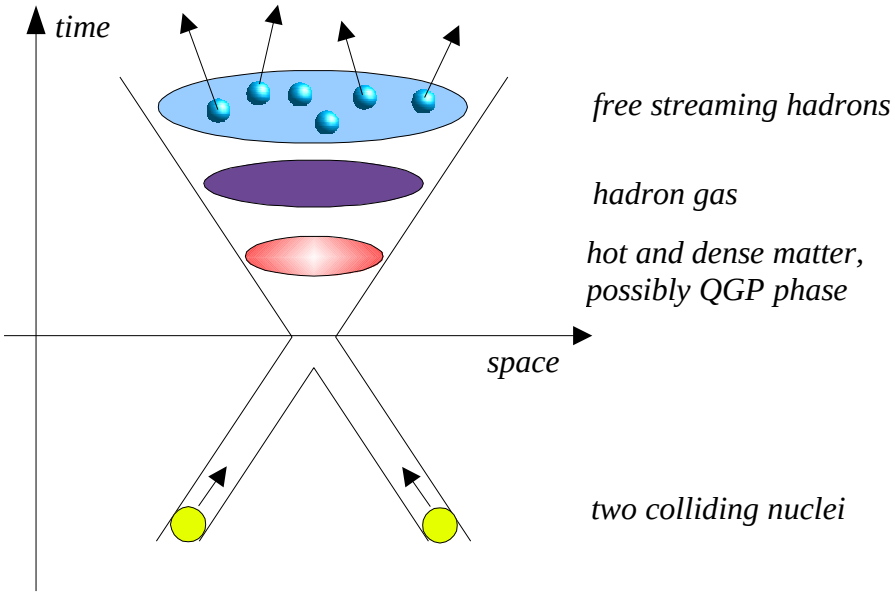

Figure 1.4

Lightcone of the reaction with the different stages.

Most of the emitted particles are pions, the lightest hadrons. Exploiting a quantum mechanical interference effect it is possible to obtain information about the space time conditions at thermal freeze out, e.g. the size of the particle source or the emission duration. Embedded into a hydrodynamical framework these measurements allow even the observation of collective effects during the expansion, e.g. radial flow. The measured freeze out parameters serve consequently as important constraints for model calculations. This particle interferometric technique is the only known way to obtain direct information about the space time structure of the freeze out process.

The method of particle interferometry applied in heavy ion physics is called HBT after the pioneering work of Robert **H**anbury **B**rown and Richard **T**wiss. They applied this method first in astrophysics to measure sizes of stars [Han54], only later it was recognized that a similar effect in particle physics can be used to determine sizes of interaction volumes in heavy ion collisions.

Particle interferometry is not only a valuable tool in the quest for the Quark Gluon Plasma; the underlying principles are quite intriguing themselves: the observation of coherent states. They are found in different chapters of physics from lasers to superconductors. Exploring the exotic features of these "quantum mechanical many particle states" contributes to the basic understanding of quantum theory [Wei00].

1.4 Notation

In this paragraph we introduce conventions and the most frequently used variables in this thesis. We use natural units $\hbar = c = 1$. The coordinate system refers to the STAR system, with the origin in the center of the detector and the z−axis paralell to the beam, the x− and y−axis orthogonal to each other and to the beam (see figure 3.3). **Bold face** denote 3−vectors.

Four momentum : energy and momentum of a particle

$$p_i = (E_i, \mathbf{p}_i) = (E_i, p_x, p_y, p_z)$$

Transverse momentum : momentum transverse to the beam

$$p_T = \sqrt{p_x^{\,2} + p_y^{\,2}}$$

Rapidity: a measure for the longitudinal velocity

$$Y = \frac{1}{2} \ln \frac{E + p_z}{E - p_z}$$

Transverse pair momentum : pair momentum transverse to the beam

$$k_T = \frac{1}{2}(p_{T,1} + p_{T,2})$$

Pairrapidity : longitudinal pair velocity

$$Y_{\pi\pi} = \frac{1}{2}\ln\frac{E_1 + p_{1,z} + E_2 + p_{2,z}}{E_1 - p_{1,z} + E_2 - p_{2,z}}$$

1.5 Content and structure of this thesis

In this work we present the results from pion interferometry with AuAu collisions at $\sqrt{s_{NN}} = 130\,\text{GeV}$. The data were recorded with the STAR detector at the RHIC accelerator in 2000.

The idea of particle interferometry and the HBT formalism is introduced in chapter 2. In chapter 3 we describe the STAR experimental setup and in chapter 4 follows a description of the data used for this analysis. In chapter 5 we present the results of pion interferometry and finally we conclude with a discussion in chapter 6 and an outlook in chapter 7.

2. HBT

Interference effects are well known physical observations. In general, interference occurs whenever waves superimpose, thus it is observed with seismic waves, light waves or sound waves. According to the wave−particle dualism, massive particles also possess wave character and therefore interference effects occur with particles like pions or protons.

The concept of interferometry is to use interference phenomena in order to obtain information about the origin of the "waves", in particular it is applied to measure sizes of objects which are not easily accessible. Michelson interferometry is used in astronomy to measure sizes of stars lightyears away from the observer. In the other extreme, particle interferometry permits the only direct spatial measurement of heavy ion reactions with typical sizes of several 10^{-15} m.

2.1. Historical overview

In the 1950s Robert **H**anbury **B**rown and Richard **T**wiss (HBT) developed a method to overcome technical limitations of Michelson amplitude interferometry [Han54]. Instead of products of sums of amplitudes Ψ:

$$\langle \mathrm{I} \rangle = \langle |\Psi_1 + \Psi_2|^2 \rangle \qquad 2.1$$

they measured average products of intensities:

$$\langle \mathrm{I}_1 \mathrm{I}_2 \rangle = \langle |\Psi_1|^2 |\Psi_2|^2 \rangle \qquad 2.2$$

To demonstrate the technique they showed that photons in an apparently uncorrelated thermal beam tend to be detected in close−by pairs [Han58]. The increased or decreased probablity to measure pairs of particles can be considered as analogue to the "interference patterns" in amplitude interference.

Later it turned out that the discovery of these "second order correlations" was not only a simple technical improvement, but a big step forward towards a new qualitative understanding of the quantum nature of light [Wei00].

In the 1960s G. **G**oldhaber, S. **G**oldhaber, W.Y. **L**ee and A. **P**ais observed in $p\bar{p}$−annihilation experiments that the angular distribution of like charged pion pairs was different from that of unlike charged pairs [Gol59][Gol60]. In particular they observed an enhancement of pion pairs with small relative momenta. Later this "GGLP−effect" was explained with Bose−Einstein correlations of pions and the

analogy to HBT measurements was established.

Since its discovery the HBT effect has been observed in many different systems, i.e. in ee, pp or AA collisions in a wide range of collision energies [Boa90][Hei99]. The theoretical understanding of the underlying principles has made substantial progress (important papers are collected in [Wei97]) and analogies to neigbourhing fields, e.g. laser physics in Quantum Optics, have been discovered.

Very early it was recognized that the HBT effect could be used to study the space−time structure of the pion source established in a heavy ion collision [Kop72, Shu73]. In recent years a comprehensive theoretical framework has been completed in order to interpret particle correlations at experiments with ultra relativistic heavy ion beams, e.g. STAR at RHIC [Gyu79][Pra86][Wie99][Wei00a].

2.2 The two particle correlation function

The measured Lorentz invariant two−particle distribution

$$P(p_1,p_2)=E_1E_2\frac{dN}{d^3\mathbf{p_1}d^3\mathbf{p_2}} \qquad 2.3$$

contains any two particle momentum correlation of the production mechanism in a heavy ion reaction. Here $P(p_1,p_2)$ indicates the probability to measure two particles with momenta p_1 and p_2. This distribution is mainly shaped by the single particle distribution. Hence the correlation function

$$C_2\equiv\frac{P(p_1,p_2)}{P(p_1)P(p_2)} \qquad 2.4$$

is defined. The reference distribution $P(p_1)P(p_2)$ is the probability to measure two particles with momenta p_1 and p_2 derived only from single particle spectrum

$$P(p)=E\frac{dN}{d^3\mathbf{p}} \qquad 2.5$$

The reference distribution mimics the two particle distribution except for any two particle correlation. Although it could be calculated in principle from the single particle spectrum $P(p)$, in experimental analyses usually the "mixed event method" is applied to model the background. That means, pairs defining the background distribution are constructed with particles from two different events. Since usually many events are recorded, the number of "mixed pairs" exceeds by far the number of

"real pairs", i.e. all possible combinations of two particles from the same event. If the number of mixed pairs is chosen to be 10−15 times larger than the number of real pairs the statistical error of the correlation function is given mainly by the statistics of the real pairs distribution.

2.3 Sources of particle correlations

Particle correlations in heavy ion collisions occur for various reasons. HBT is based on momentum correlations between identical particles due to their quantum character. The multiparticle states which describe the source at thermal freeze out obey quantum statistical rules. If the particles are bosons, e.g. pions, Bose Einstein statistics applies. Therefore pion HBT is often referred to as Bose Einstein correlations. In case of fermions, Fermi Dirac statistics is appropriate. The quantum statistical rules lead to pattern in the phase space distribution of the emitted particles. Measuring the momentum component of this phase space distribution allows to draw conclusions about its space component; this is the basic concept of HBT.

It is important to extract the correlations due to quantum statistics only. Possible other correlations superimposing the HBT effect must be considered. In case of an alteration of the correlation function, a correction has to be applied. The main sources for other correlations are [Hei99a]

- Energy momentum conservation constrains the momentum distribution if only a few particles are produced. In relativistic heavy ion collisions, when hundreds of particles are emitted, this becomes negligible. For the same reason conservation laws with respect to quantum numbers, like charge or isospin, are not taken into account.
- Correlations due to the decay products of resonances are very strong. But since resonances rarely decay into two like sign pions they are not taken into account in this analysis.
- Final state interactions due to the strong force between two pions are negligible; especially in the region of small relative momenta which is interesting for HBT.
- Long−range coulomb interactions between two emitted pions have a significant effect on the two particle distribution. Therefore we have to introduce a correction for this distortion. In principle these coulomb interactions are also suited to derive source sizes. This is possible with e.g. unlike sign pions where no quantum statistical effects are observed.

2.4 Bose Einstein correlations

The principle of HBT measurements is demonstrated in the following example [Won94]:

Assume two identical particles with momenta p_1 and p_2 are produced at points x and y within a source volume described by a density $\rho(x)$. After their emission they are recorded with detectors at r_1 and r_2.

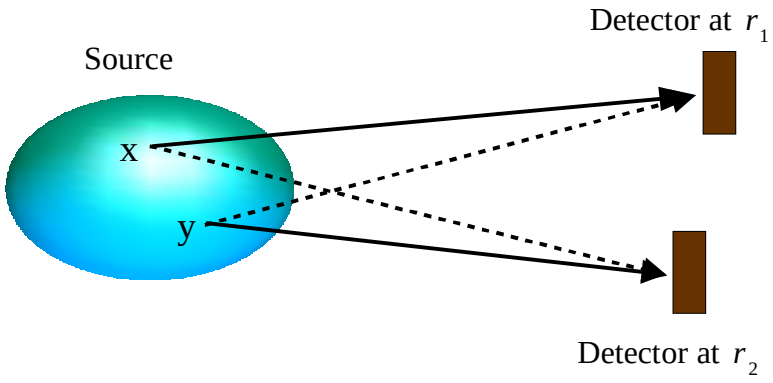

Figure 2.1

Assume two identical particles are produced within a small enough source at x and y. According to Heisenbergs uncertainty principle it is impossible to decide, whether their paths are described by the dashed or the full lines.

First we derive the single particle spectrum. We assume the probability amplitude to produce a pion with momentum p_1 at x is described by $A(p_1,x)$ and the propagation of the particle to the detector at r_1 by $e^{i p_1 (x-r_1)}$. The probability for a pion of momentum p_1 produced in the source volume $\rho(x)$ to arrive at r_1 is then

$$P(p_1)=\left|\int dx\,\rho(x)A(p_1,x)e^{i p_1(x-r_1)}\right|^2=\int dx\,\rho(x)A^2(p_1,x) \qquad 2.6$$

Now we determine the two particle distribution. The indistinguishability of identical particles leads to the requirement that observables of multiparticle states must be independent of the order of the particles. The probability amplitude for bosons must be symmetric with respect to the interchange of particles. Pions obey Bose Einstein statistics, therefore the probability amplitude to produce two pions at x and y with

momenta p_1 and p_2 and to detect them at r_1 and r_2 is given by

$$\Phi = \frac{1}{\sqrt{2}}\left(A(p_1,x)\, e^{\,i p_1 (x-r_1)}\, A(p_2,y)\, e^{\,i p_2 (y-r_2)} \right) + \frac{1}{\sqrt{2}}\left(A(p_1,y)\, e^{\,i p_1 (y-r_1)}\, A(p_2,x)\, e^{\,i p_2 (x-r_2)} \right) \qquad 2.7$$

The meaning of equation 2.7 is illustrated in figure 2.1, the probability amplitude must allow for the particles to follow either the dashed or the full line.

With equation 2.7 the probability to detect two pions can be deduced :

$$P(p_1,p_2) = \int dx\, dy\, \rho(x)\, \rho(y) \left|\Phi\right|^2 = P(p_1)\,P(p_2) + \left| \int dx\, e^{\,i(p_1-p_2)\cdot x}\, \rho(x)\, A(p_1,x)\, A(p_2,x) \right|^2 \qquad 2.8$$

If we introduce the effective density

$$\rho_{\text{eff}}(x) = \frac{\rho(x)\, A(p_1,x)\, A(p_2,x)}{\sqrt{P(p_1)\,P(p_2)}} \qquad 2.9$$

and its fourier transform with the four momentum difference q

$$\tilde{\rho}_{\text{eff}}(q) = \int dx\, e^{\,iqx}\, \rho_{\text{eff}}(x) \qquad 2.10$$

we find

$$P(p_1,p_2) = P(p_1)\,P(p_2)\left(1 + \left| \tilde{\rho}_{\text{eff}}(q) \right|^2 \right) \qquad 2.11$$

Equation 2.11 enables us to relate the correlation function to the density

$$C_2(q) = \frac{P(p_1,p_2)}{P(p_1)\,P(p_2)} = 1 + \left| \tilde{\rho}_{\text{eff}}(q) \right|^2 \qquad 2.12$$

Equation 2.12 is the basic relation of Bose−Einstein interferometry: the measured momentum correlation function $C_2(q)$ provides information about the space−time structure of the particle emitting source.

To further illustrate the method, let us assume the source could simply be described by a Gaussian distribution with a spatiotemporal extension R_{inv}:

$$\rho_{eff}(x)=\frac{1}{R_{inv}^4}e^{-\frac{x^2}{R_{inv}^2}} \qquad 2.13$$

The approriate parametrization of the correlation function in this case is given by

$$C_2(q_{inv})=1+e^{-q_{inv}^2 R_{inv}^2} \qquad 2.14$$

with the four momentum difference $q_{inv}=|p_1-p_2|$.

Extracting the parameter R_{inv} in the measured correlation function $C_2(q)$ yields the width of the source distribution $\rho_{eff}(x)$.

2.5 Classical current formalism

A realistic source function is certainly more complicated than the Gaussian shaped density assumed in the previous paragraph. The longitudinal and transverse expansion for example have a considerable impact on the source function and hence on the correlation function. Furthermore the correlation function can be measured in three independent momentum components and therefore the emission function is not restricted to one dimension as in equation 2.13.

A more comprehensive framework is deduced for example in [Hei99a]. The model is based on a description of the particle emitting source using classical currents. We denote the final pion state of a heavy ion collision with $|J\rangle$ and assume that at kinetic freeze out the emitting source is not affected by the emission of a single particle. $|J\rangle$ is then a coherent state which is by definition an eigenstate of the annihilation operator $\hat{a}_{\mathbf{p}}$

$$\hat{a}_{\mathbf{p}}|J\rangle=i\tilde{J}(\mathbf{p})|J\rangle \qquad 2.15$$

where $\tilde{J}(\mathbf{p})$ is the on shell fourier transform of the current $J(x)$. The latter is a space time function approximating the nuclear current operator defining sources of pions at freeze out $\hat{J}(x)$ [Boa90].

The classical current is approximated by the sum over individual elementary source

functions J_0:

$$\tilde{J}(\mathbf{p}) = \sum e^{i\phi_i} e^{ip\cdot x_i} \tilde{J}_0(p - p_i) \qquad 2.16$$

A "chaotic" source is characterized by random phases ϕ_i. It is currently not known to which degree this independence is established in nuclear collisions, the laser is an example in quantum optics of a completely non−chaotic source. The effect of partial chaoticity on the two particle correlation function could be severe. In the extreme case of a completely non−chaotic source the correlation would even vanish. There is no unambigious evidence from two particle correlations, to which degree the source is chaotic. Perhaps the study of three−pion correlations answers this question [Hei97]. In the following we will assume a completely chaotic source, but a similar formalism can also be derived for a partial chaotic source.

The goal is to gain as much information as possible about the emission function S(x,k), which is the Wigner phase space density of the pion source. When averaged over phase−space volumes which are large compared to the volume of an elementary phase−space cell, this function can be interpreted as the classical phase−space density.

The emission function S(x,k) can be identified as the fourier transform of the covariant quantity

$$\tilde{S}_j(\mathbf{p_1}, \mathbf{p_2}) = \sqrt{E_1 E_2} \left\langle \tilde{J}^+(\mathbf{p_1}) \tilde{J}(\mathbf{p_2}) \right\rangle \qquad 2.17$$

If the emission function has a sufficiently smooth momentum dependence it can be related to the correlation function

$$C_2(\mathbf{q}, \mathbf{k}) = 1 + \frac{\left| \int dx \;\; S(x,k) e^{iq\cdot x} \right|^2}{\left| \int dx \;\; S(x,k) \right|^2} \qquad 2.18$$

Because the emitted particles are on shell, i.e. $E_i = \sqrt{\mathbf{p}_i^2 + m_i^2}$ for all particles, the correlation function $C_2(\mathbf{q}, \mathbf{k})$ depends only on three independent components. Due to this "mass shell constraint" relation 2.18 yields not a unique expression for the emission function $S(x,k)$. To resolve this ambiguity one has to make additional assumptions about the emission process which cannot be derived by two particle interferometry.

The measured correlation function is usually parametrized by a Gaussian function

$$C_2(\mathbf{q}, \mathbf{k}) = 1 + \lambda(\mathbf{k}) \;\; e^{-\sum R_{ij}^2(\mathbf{k}) \mathbf{q_i} \mathbf{q_j}} \qquad 2.19$$

where the HBT radius parameters R_{ij} equal the space−time variances of the emission function $S(x,k)$.

The factor $\lambda(\mathbf{k})$ summarizes several distortions of the correlation function. It is strongly affected by resonance decays, final state interactions and detector uncertainties. But $\lambda(\mathbf{k})$ also indicates to which degree the emission is chaotic, if there were no other influences and the phases introduced in 2.16 were completely random $\lambda(\mathbf{k})$ would equal unity. If on the other hand the emission were correlated and the phases were fixed in equation 2.16, the $\lambda(\mathbf{k})$ parameter would vanish and hence the radii were immeasurable.

2.6 Approximating the emission function

To connect the measured HBT radii from equation 2.19 to the emission function $S(x,k)$ in equation 2.18, we have to make some basic assumptions. First we approximate the emission function by a Gaussian function. Therefore we define effective source centers $\bar{x}^{\mu}(k)$ as the points of maximum emission probability

$$\bar{x}^{\mu}(k)=\langle x^{\mu}\rangle(k) \qquad 2.20$$

where $\langle\ldots\rangle$ denotes the space time average over the emission function. This allows to express the space time coordinates relative to a hypersurface

$$\tilde{x}^{\mu}(k)=x^{\mu}-\bar{x}^{\mu}(k) \qquad 2.21$$

Then we are able to approximate the emission function with

$$S(x,k)\approx S(\bar{x}(k),k)e^{-\frac{1}{2}\tilde{x}^{\mu}(k)B_{\mu\nu}(k)\tilde{x}^{\nu}(k)} \qquad 2.22$$

where $(B^{-1})_{\mu\nu}$ is related to the space time variances by

$$(B^{-1})_{\mu\nu}(k)=\langle\tilde{x}_{\mu}\tilde{x}_{\nu}\rangle(k) \qquad 2.23$$

and with equation 2.19 we derive the correlation function

$$C(\mathbf{q},\mathbf{k})=1+\lambda(\mathbf{k})e^{-q_{\mu}q_{\nu}\langle\tilde{x}_{\mu}\tilde{x}_{\nu}\rangle(\mathbf{k})} \qquad 2.24$$

Obviously the correlation functions yields no information about absolute values of emission points within the source since only distances relative to $\bar{x}^{\mu}(k)$ occur. HBT radii are therefore identified with the size of the "region of homogeneity", the region

from which particle pairs with momentum k are most likely emitted. Only in the special case, that the emission function has no space−momentum correlations the space time variances equal the actual source extensions. Otherwise the HBT radii depend on the expansion dynamics of the source.

Next, we introduce two HBT parametrizations, i.e. choices for decomposing the momentum difference $\mathbf{q}$ in equation 2.24. We explain the actual meaning of the corresponding HBT radii and later these parametrizations will be applied to experimental data.

In chapter 2.9 we introduce a specific emission function with explicit space−momentum correlations and discuss the interpretation of the measured HBT radii in this case.

2.7 Pratt−Bertsch parametrization

A convenient choice for the three independent components of $\mathbf{q}$ in equation 2.24 is give by $\mathbf{q}=(q_{out},q_{side},q_{long})$ with

$$q_{out}=\frac{\left|\mathbf{q}_t\cdot\mathbf{k}_t\right|}{\left|\mathbf{k}_t\right|}$$
$$q_{side}=\frac{\left|\mathbf{q}_T\times\mathbf{k}_t\right|}{\left|\mathbf{k}_t\right|}$$
$$\mathbf{q}_{long}=\mathbf{p}_{z,1}-\mathbf{p}_{z,2} \qquad 2.25$$

and

$$\mathbf{k}_t=\frac{1}{2}(\mathbf{p}_{t,1}+\mathbf{p}_{t,2})=\frac{1}{2}(p_{x,1}+p_{x,2},p_{y,1}+p_{y,2},0)$$
$$\mathbf{q}_t=\mathbf{p}_{t,1}-\mathbf{p}_{t,2}=(p_{x,1}-p_{x,2},p_{y,1}-p_{y,2},0) \qquad 2.26$$

The vectors $\mathbf{q}_{out}$ and $\mathbf{q}_{side}$ lie in the transverse plane, $\mathbf{q}_{out}$ is parallel and $\mathbf{q}_{side}$ perpendicular to $\mathbf{k}_t$. Figure 2.2 shows the decomposition of the transverse components. This parametrization is often referred to as **P**ratt−**B**ertsch (PB) after the references [Pra86][Ber89].

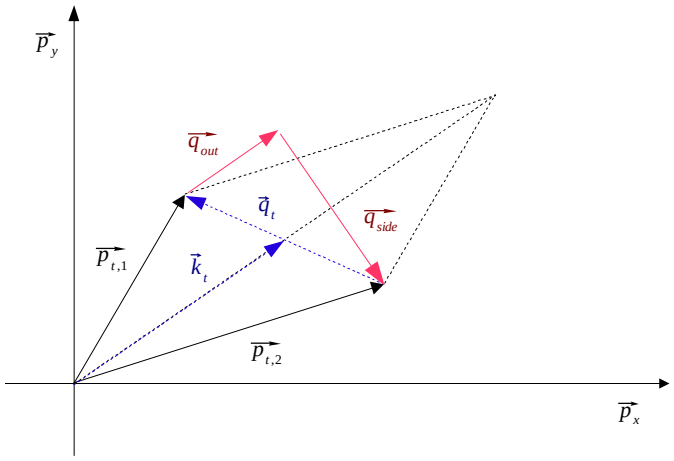

Figure 2.2
Composition of q_{out} and q_{side} according to equation 2.25.

With this choice the mass shell constraint takes the form

$$q_0 = \beta \cdot \mathbf{q} \qquad 2.27$$

with

$$\beta = \frac{\mathbf{k}}{k_0} \quad \text{or} \quad \beta = (\beta_{out}, 0, \beta_{long}) \quad \text{in the out−side−long system.}$$

Hence q_0 is not explicitly measured and the corresponding temporal component is eliminated.

Assuming an azimuthally symmetric source, we can rotate the out−side−long system until $q_x = q_{out}$ and $q_y = q_{side}$. In this case we find $\bar{y} = \langle y \rangle = 0$ and hence three space time variances $\langle \tilde{x}_\mu \tilde{x}_\nu \rangle(\mathbf{k})$ in equation 2.24 linear in $\tilde{y}$ vanish. Four non vanishing space time variances remain which are associated with the HBT radius parameters R_{side}, R_{out}, R_{long} and $R_{outlong}$:

$$
\begin{aligned}
R^2_{side}(\mathbf{k}) &= \langle \tilde{y}^2 \rangle(\mathbf{k}) \\
R^2_{out}(\mathbf{k}) &= \langle (\tilde{x} - \beta_{out}\tilde{t})^2 \rangle(\mathbf{k}) \\
R^2_{long}(\mathbf{k}) &= \langle (\tilde{z} - \beta_{long}\tilde{t})^2 \rangle(\mathbf{k}) \\
R^2_{outlong}(\mathbf{k}) &= \langle (\tilde{x} - \beta_{out}\tilde{t})(\tilde{z} - \beta_{long}\tilde{t}) \rangle(\mathbf{k})
\end{aligned}
\qquad 2.28
$$

Assuming a longitudinal boost invariant Bjorken szenario [Bjo83][Won94] with a freeze out at constant proper time τ_0, the space time position of the emitted particle and its rapidity *Y* are related by

$$z = \tau_0 \sinh Y \qquad 2.29$$

and the emission function is symmetric along z. If we boost the correlation function in the longitudinal comoving system (LCMS), a frame where the longitudinal velocity of the pair vanishes, we find $\beta_{long} = 0$ and expressions 2.28 simplify to

$$
\begin{aligned}
R^2_{side}(\mathbf{k}) &= \langle \tilde{y}^2 \rangle(\mathbf{k}) \\
R^2_{out}(\mathbf{k}) &= \langle (\tilde{x} - \beta_{out}\tilde{t})^2 \rangle(\mathbf{k}) \\
R^2_{long}(\mathbf{k}) &= \langle \tilde{z}^2 \rangle(\mathbf{k}) \\
R^2_{outlong}(\mathbf{k}) &= 0
\end{aligned}
\qquad 2.30
$$

The more symmetries in the emission function are assumed the simpler the expressions for the HBT radii become. If we give up for example the assumption of a vanishing impact parameter, and with it an azimuthal symmetric source, we need a more sophisticated framework, but on the other hand with an appropriate formalism we gain valuable information about exactly this non−symmetry [Lis99][Hei97].

In summary, choosing the Pratt−Bertsch parametrization the correlation function takes the form

$$C(\mathbf{q},\mathbf{k}) = 1 + \lambda(\mathbf{k}) e^{-q^2_{side}R^2_{side} - q^2_{out}R^2_{out} - q^2_{long}R^2_{long} - q_{out}q_{long}R^2_{outlong}} \qquad 2.31$$

and the HBT radii can be interpreted as :

- R_{side} measures the width of the emission region in side direction.
- R_{out} measures a combination of the extension in out direction and the emission duration.
- In the LCMS frame R_{long} measures the longitudinal width of the emission region.

2.8 Yano−Koonin−Podgoretskii parametrization

A different choice for the decompostion of $\mathbf{q}$ in equation 2.24 is given by

$$\begin{aligned} q_{perp} &= \sqrt{q_x^2 + q_y^2} = \sqrt{q_{out}^2 + q_{side}^2} \\ q_{para} &= p_{1,z} - p_{2,z} = q_{long} \\ q_0 &= E_1 - E_2 \end{aligned} \qquad 2.32$$

Assuming an azimuthally symmetric collision region and a longitudinal expansion velocity

$$\begin{aligned} u(\mathbf{k}) &= \gamma(\mathbf{k})\left(1,0,0,\beta_{YKP}(\mathbf{k})\right) \\ \gamma(\mathbf{k}) &= \frac{1}{\sqrt{1-\beta_{YKP}^2(\mathbf{k})}} \end{aligned} \qquad 2.33$$

the correlation function takes the form

$$\begin{aligned} C(\mathbf{q},\mathbf{k}) &= 1+\lambda(\mathbf{k})\, e^{-R_{perp}^2(\mathbf{k})q_{perp}^2 - R_{para}^2(\mathbf{k})\left(q_{para}^2 - q_0^2\right) - \left(R_0^2(\mathbf{k}) + R_{para}^2(\mathbf{k})\right)\left(q\cdot u(\mathbf{k})\right)^2} \\ &= 1+\lambda(\mathbf{k})\, e^{-q_{perp}^2 R_{perp}^2(\mathbf{k}) - \gamma^2(\mathbf{k})\left(q_{para} - \beta_{YKP}(\mathbf{k}) q_0\right)^2 R_{para}^2(\mathbf{k}) - \gamma^2(\mathbf{k})\left(q_0 - \beta_{YKP}(\mathbf{k}) q_{para}\right)^2 R_0^2(\mathbf{k})} \end{aligned} \qquad 2.34$$

This parametrization is based on the work of **Y**ano, **K**oonin [Yan78] and **P**odgoretskii [Pod83] (YKP). Compared to the PB parametrization the YKP formulation takes the longitudinal expansion explicitly into account and the emission duration is given directly by R_0.

The parameters are related to the Gaussian space time variances in 2.24 by

$$\begin{aligned} R_{perp}^2(\mathbf{k}) &= \langle \tilde{y}^{\,2}(\mathbf{k}) \rangle \\ R_0^2(\mathbf{k}) &= A - \beta_{YKP}(\mathbf{k})\, C \\ R_{para}^2(\mathbf{k}) &= B - \beta_{YKP}(\mathbf{k})\, C \end{aligned} \qquad 2.35$$

with

$$\beta_{\mathrm{YKP}}(\mathbf{k})=\frac{\mathrm{A}+\mathrm{B}}{2\mathrm{C}}\left(1-\sqrt{1-\left(\frac{2\mathrm{C}}{\mathrm{A}+\mathrm{B}}\right)^2}\right)$$

$$\mathrm{A}=\left\langle\left(\tilde{\mathrm{t}}-\frac{\tilde{\xi}}{\beta_{\mathrm{out}}}\right)^2\right\rangle(\mathbf{k})$$

$$\mathrm{B}=\left\langle\left(\tilde{\mathrm{z}}-\frac{\beta_{\mathrm{long}}}{\beta_{\mathrm{out}}}\tilde{\xi}\right)^2\right\rangle(\mathbf{k})$$

$$\mathrm{C}=\left\langle\left(\tilde{\mathrm{t}}-\frac{\tilde{\xi}}{\beta_{\mathrm{out}}}\tilde{\xi}\right)\left(\tilde{\mathrm{z}}-\frac{\beta_{\mathrm{long}}}{\beta_{\mathrm{out}}}\tilde{\xi}\right)\right\rangle(\mathbf{k}) \qquad 2.36$$

using the shorthand $\tilde{\xi}=\tilde{\mathrm{x}}+\mathrm{i}\,\tilde{\mathrm{y}}$.

The parameter $\beta_{\mathrm{YKP}}(\mathbf{k})$ is related to the velocity of the source element which emits the particles contributing to the correlation function. In model studies [Hei99a] it was shown that this parameter follows closely the velocity of the Longitudinal Saddle Point System which is the longitudinally comoving Lorentz frame at the point of highest particle emissitivity for a given pair momentum **k**. The relation between the longitudinal pair rapidity $\mathrm{Y}_{\pi\pi}$ and the Yano Koonin rapidity

$$\mathrm{Y}_{\mathrm{YKP}}(\mathbf{k})=\frac{1}{2}\ln\left(\frac{1+\beta_{\mathrm{YKP}}(\mathbf{k})}{1-\beta_{\mathrm{YKP}}(\mathbf{k})}\right) \qquad 2.37$$

illustrates the meaning of this parameter. For a static source, i.e. without any space momentum correlations, $\mathrm{Y}_{\mathrm{YKP}}$ is independent of $\mathrm{Y}_{\pi\pi}$ and identical to the rapidity of the CMS of the whole source:

$$\mathrm{Y}_{\mathrm{YKP}}(\mathbf{k})=\text{const.} \qquad 2.38$$

If we consider however sources with strong longitudinal expansion or even longitudinal boost invariant sources for which the thermal freeze out occurs close to a hypersurface of constant longitudinal proper time, $\mathrm{Y}_{\mathrm{YKP}}$ depends linearly on $\mathrm{Y}_{\pi\pi}$

$$\mathrm{Y}_{\mathrm{YKP}}(\mathbf{k})\approx\text{const.}\cdot\mathrm{Y}_{\pi\pi} \qquad 2.39$$

The linear dependence means not necessarily a boost invariance, it only indicates a longitudinal expansion which is sufficiently strong to overcome the thermal smearing of the particle momenta [Hei99a].

The interpretation of the radii in this parametrization becomes particularly simple if

the correlation function is measured in a frame where the Yano Koonin velocity $\beta(\mathbf{k})$ vanishes. In this case the radius parameters measure directly the transverse, longitudinal and temporal size of the effective source in the rest frame of the source element

$$\begin{aligned} R^2_{\text{perp}}(\mathbf{k}) &\approx \langle \tilde{y}^2(\mathbf{k}) \rangle \\ R^2_{\text{para}}(\mathbf{k}) &\approx \langle \tilde{z}^2(\mathbf{k}) \rangle \\ R^2_0(\mathbf{k}) &\approx \langle \tilde{t}^2(\mathbf{k}) \rangle \end{aligned} \qquad 2.40$$

2.9 PB versus YKP parametrization

The information carried by the correlation function does not depend on the parametrization. Hence radii from PB and YKP parametrizations are related to each other and results from the two methods can be directly compared. These relations can be used as a consistency check.

If we express the PB parameters in terms of YKP parameters we find

$$\begin{aligned} R^2_{\text{side}} &= R^2_{\text{perp}} \\ R^2_{\text{out}} - R^2_{\text{side}} &= \beta^2_{\text{out}} \gamma^2 \left(R^2_0 + \beta^2_{\text{YKP}} R^2_{\text{para}} \right) \\ R^2_{\text{long}} &= \left(1 - \beta^2_{\text{long}}\right) R^2_{\text{para}} + \gamma^2 \left(\beta_{\text{long}} - \beta_{\text{YKP}} \right)^2 \left(R^2_0 + R^2_{\text{para}} \right) \\ R^2_{\text{out,long}} &= \beta_{\text{out}} \left(-\beta_{\text{long}} R^2_{\text{para}} + \gamma^2 \left(\beta_{\text{long}} - \beta_{\text{YKP}} \right) \left(R^2_0 + R^2_{\text{para}} \right) \right) \end{aligned} \qquad 2.41$$

β_{long} vanishes in the longitudinal comoving system (LCMS). If we further assume the source had a strong longitudinal expansion and that therefore β_{YKP} vanished, equations 2.41 simplify to

$$\begin{aligned} R^2_{\text{side}} &= R^2_{\text{perp}} \\ R^2_{\text{out}} - R^2_{\text{side}} &= \beta^2_{\text{out}} R^2_0 \\ R^2_{\text{long}} &= R^2_{\text{para}} \\ R^2_{\text{out,long}} &= 0 \end{aligned} \qquad 2.42$$

2.10 Collective expansion and the k_t−dependence of measured HBT radii

If the particle momenta and emission points are correlated, the space−time variances in 2.24 depend on the pair momentum **k**. The most important mechanism to produce such correlations is collective expansion of the source. Random motion due to the finite temperature of the source tends to weaken the space−momentum correlations caused by collective flow. Assuming a rather general emission function the dependences of HBT radii on **k** can be related to prominent features of the expansion and to the temperature of the source.

A widely used parametrization of the emission function is given by [Hei99]

$$S(x,k)=\frac{m_t\cosh(\eta-Y)}{8\pi^4\Delta\tau}\exp\left(-\frac{K\cdot u(x)}{T(x)}-\frac{(\tau-\tau_0)^2}{2(\Delta\tau)^2}-\frac{r^2}{2R^2}-\frac{(\eta-\eta_0)^2}{2(\Delta\eta)^2}\right) \qquad 2.43$$

Where $r^2=x^2+y^2$, $\eta=0.5\cdot\ln\left((t+z)/(t-z)\right)$ and $\tau=\sqrt{t^2-z^2}$ parametrize the space time coordinates x^μ, and $Y=0.5\cdot\ln\left((E+k)/(E-k)\right)$ and $m_t=\sqrt{m^2+k_t^2}$ the pair momenta k.

R is the transverse radius of the source, τ_0 the average freeze out proper time and $\Delta\tau$ the mean duration of particle emission. $\Delta\eta$ accounts for the finite longitudinal extension of the source.

The space momentum correlations are introduced by the Boltzmann factor $\exp(-k\cdot u(x)/T(x))$ with a velocity field u(x) and a temperature T. Usually the velocity field is decomposed into

$$u(x)=(\cosh\eta_l\cosh\eta_t,\sinh\eta_t\mathbf{e}_r,\sinh\eta_l\cosh\eta_t) \qquad 2.44$$

with longitudinal and transverse flow rapidities $\eta_l(x)$ and $\eta_t(x)$. In longitudinal direction, boost invariant flow is assumed $\eta_l(x)=\eta(v_l=z/t)$ and in transverse direction the flow profile is parametrized by $\eta_t(x)=\eta_f\cdot(r/R)$ with a scale parameter η_f and the transverse radius R.

Using the emission function given in equation 2.43 and employing the saddle point approximation 2.22, the characteristics of the source R, T, τ_0, $\Delta\tau$ and η_f can be related to the **k**−dependence of the measured HBT radii. According to [Hei99] we find the following approximations:

$$R_{side}(m_t) \approx \frac{R}{\sqrt{1+\frac{\eta_f^2}{T} m_t}} \qquad 2.45$$

$$R_{long}(m_t) \approx \tau_0 \sqrt{\frac{T}{m_t}} \qquad 2.46$$

and

$$R_{out}^2(\mathbf{k}) - R_{side}^2(\mathbf{k}) \approx \beta_{out}^2 \Delta\tau \qquad 2.47$$

These relations are highly model dependent, they rely on a number of approximations and assumptions, nevertheless they are often used to associate a specific physical meaning to extracted HBT radii. To test the validity of the approximations above, one has to check whether the resulting source parameters are consitent with other observations. E.g. temperature and transverse expansion also determine the shape of single particle transverse momentum spectra and can therefore be derived via this observable. Only if all observations fit into a consistent picture, we can draw conclusions about the early stages of a heavy ion collision and a possible phase transition.

2.11 Coulomb correction

The coulomb repulsion between like sign charged pions acting when they leave the collision region changes their relative momentum. This effect is corrected for by weighting the mixed pairs with a Coulomb correction factor. It is calculated by taking the square of the nonrelativistic wave function describing a particle in a Coulomb field [Mes61]

$$H(\mathbf{k},\mathbf{r}) = \frac{2\pi\eta}{e^{2\pi\eta}-1} \left| F\left(-i\eta; 1; ik\left(r - \frac{\mathbf{r}\cdot\mathbf{k}}{k}\right)\right)\right|^2 \qquad 2.48$$

with

F: confluent hypergeometric function

$\mathbf{k}$: momentum of a pion in the pair c.m. system

$\mathbf{r}$: relative distance of the two pions at freeze out

$$\eta = \frac{Z_1 Z_2 m_\pi c \alpha}{q_{inv}}$$

m_π: pion mass

α: fine structure constant

For pions emitted from a pointlike source, F equals unity and the Coulomb correction becomes the Gamov factor [Hei99a]. Assuming a finite source size the correction can be calculated numerically. In Fig. 2.3 the correction is displayed for several source sizes.

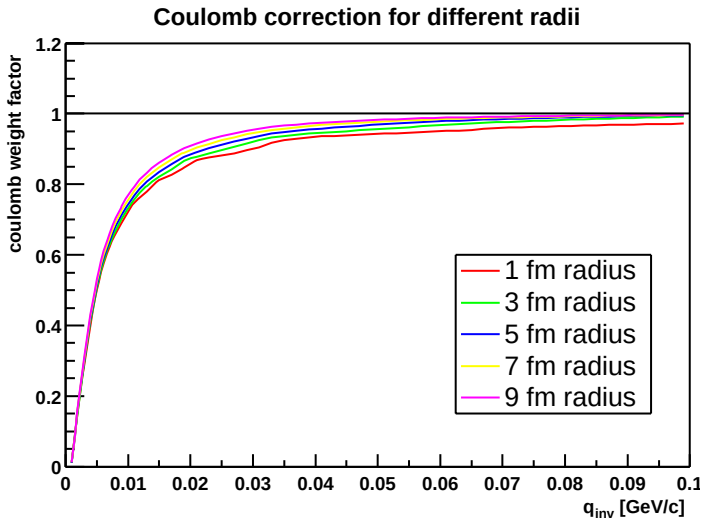

Figure 2.3

Coulomb weight for a pair of mometum difference q_{inv} for different source sizes.

3. The STAR experiment

3.1 The Relativistic Heavy Ion Collider (RHIC)

The **R**elativistic **H**eavy **I**on **C**ollider (RHIC) at Brookhaven National Laboratory in New York, USA, was built to study pp and AA collisions at various energies from $\sqrt{S_{NN}} \approx 20\ \text{GeV}$ up to $\sqrt{S_{NN}} \approx 200\ \text{GeV}$.

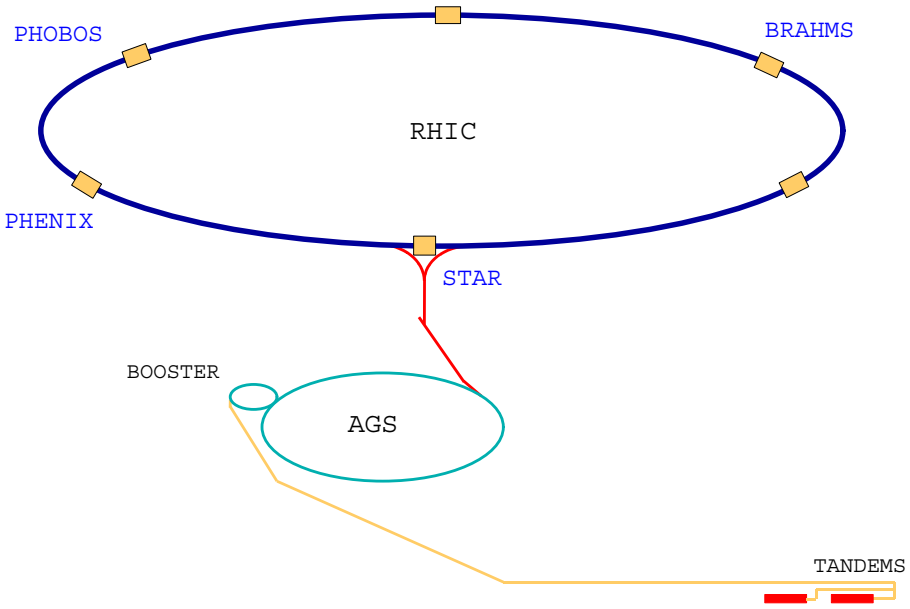

Figure 3.1

The RHIC complex consists of four accelerators:

- *Tandems (top energy 1 MeV/u, charge of a gold ion at top energy Q=+32)*
- *Booster (95 MeV/u, Q=+77)*
- *AGS (10.8 GeV/u, Q=+79)*
- *RHIC (100.0GeV/u, Q=+79)*

At four interaction points detector systems are mounted named BRAHMS, PHOBOS, PHENIX and STAR.

We will focus here on the first AuAu run at RHIC in the year 2000 [Ros02] when the data used in this analysis were collected.

Several steps are necessary to obtain the preaccelerated gold ion beam needed by the Relativistic Heavy Ion Collider (see figure 3.1). A "Tandem Van de Graaff" accelerator delivers an ion beam to the "Booster Synchrotron", which accelerates ions to 37% the speed of light and injects them into the "**A**lternating **G**radient **S**ynchrotron" (AGS). At this facility the nuclei are brought to 99.7% the speed of light and finally transferred to the collider. The gold ions are ionized stepwise as they are acclerated to RHIC injection energy, at which point they are fully ionized.

RHIC consists of two concentric independent rings with 3834 m in circumference. 1740 superconducting magnets cooled down to $4.5^{o}\,\mathrm{K}$ keep the ion beams inside two highly evacuated tubes. In one of the the rings bunches of ions are accelerated clockwise and in the other one counterclockwise. 60 bunches are injected into each collider ring with $\sim 1\cdot 10^{9}$ ions per bunch. This yields a design luminosity of $\mathscr{L} \approx 2\cdot 10^{26}\,\mathrm{cm}^{-2}\mathrm{s}^{-1}$,but in 2000 only an average luminosity of $\mathscr{L} \approx 1.7\cdot 10^{25}\,\mathrm{cm}^{-2}\mathrm{s}^{-1}$ was reached. This luminosity allowed to collect several 10^{5} events during the two month run in 2000.

The filling of the collider with accelerated ion bunches takes approximately 1 min and the acceleration another ~75 s. The beam is than stored up to 10 h before another fill becomes necessary, a typical store in 2000 lasted 5 h. The top energy is 100 GeV per nucleon which was not achieved until the 2001 run period. 65 GeV per nucleon were reached during the 2000 run period.

At four interaction regions, large detector systems named BRAHMS, PHOBOS, PHENIX and STAR are installed. At these interaction points the beams cross each other to generate collisions of ions. The crossing angle at the interaction region is below $1.7\,\mathrm{mrad}$. The design value for the length of the interaction diamond of $\approx 20\,\mathrm{cm}$ was not achieved in 2000. Events occuring too far away from the detector center had to be rejected, since the detectors are optimized for events with the main vertex in their center.

Besides gold ions the collider facility is also capable of accelerating light nuclei and even protons. A whole program is set up to study collisions of polarized protons in order to analyse the spin structure of nucleons [Vig99]. To meet the different requirements from all physics programs the detector systems have to be very flexible. They must be able to handle several thousand particles produced in a single central AuAu collision, and on the other hand they are used to study ultra peripheral collisions where only a few particles are produced.

3.2 The Solenoidal Tracker At RHIC (STAR)

Each of the four experiments at RHIC focuses on different aspects of particle collisions. The **S**olenoidal **T**racker **A**t **R**hic (STAR) [Har02][Nim03OV] is built to measure thousands of particles which can be produced by a single collision at RHIC. STAR consists of several individual detectors with different tasks, figure 3.2 shows a schematic layout.

The curvature of trajectories of charged particles in a magnetic field allows the determination of their momentum. Therefore the tracking detectors are surrounded by a solenoid magnet providing a uniform magnetic field up to 0.5 T. During the run period 2000 it was operated at 0.25 T.

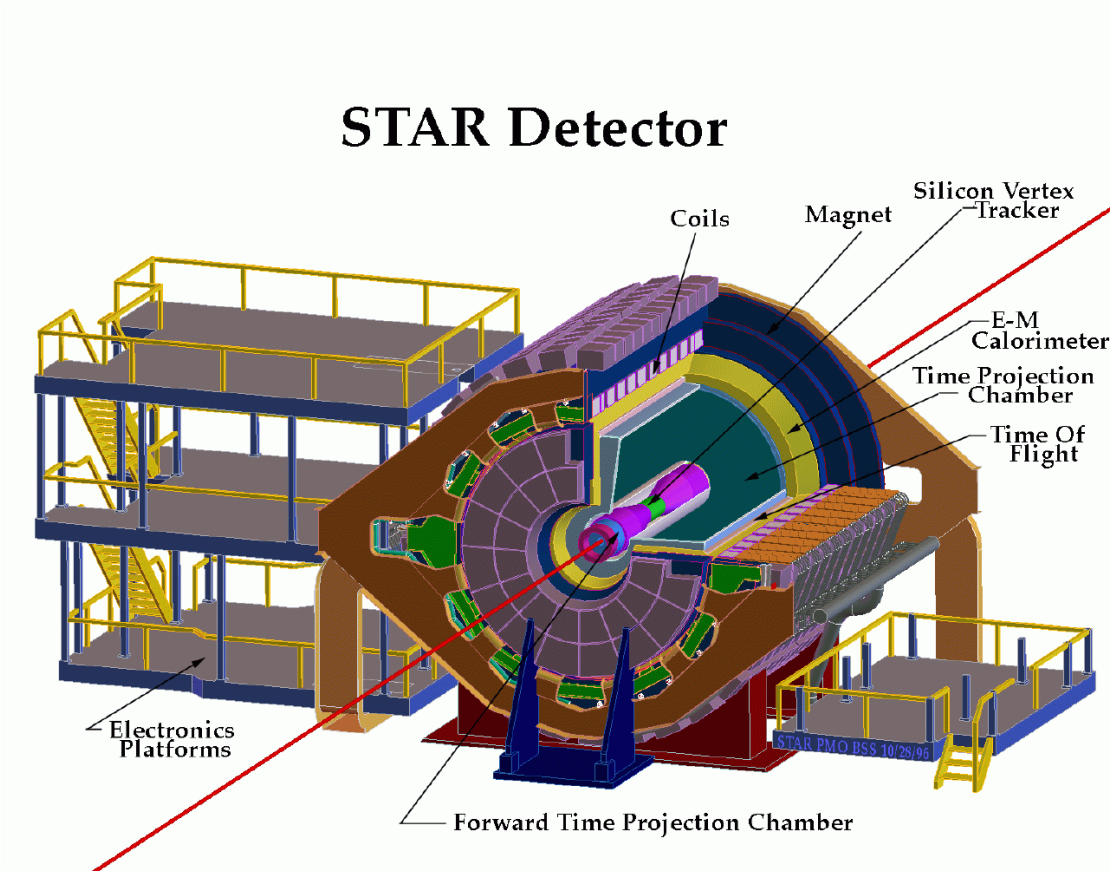

Figure 3.2

STAR layout with the main subdetectors

The central detector of STAR is a **T**ime **P**rojection **C**hamber (TPC) measuring trajectories of charged particles with $|\eta|<1.8$. Analyses presented in this thesis are based only on TPC data, therefore this detector is discussed in detail in chapter 3.3. Several other detectors improve momentum resolution, two track resolution, vertex resolution and particle identification or they increase the acceptance of STAR. Many of these devices were installed after the year 2000 run.

The main subdetecors besides the TPC are listed below :

- **S**ilicon **V**ertex **T**racker (SVT): consists of three concentric barrels of silicon drift detectors 5 cm, 10 cm and 15 cm from the beam with precise position measurement to increase the vertex position resolution as well as the momentum and two track resolution. Additionally energy loss measurements improve the particle identification capabilities [Nim03SVT].
- **S**ilicon **S**trip **D**etector (SSD): another cylindric silicon detector 23 cm from the beam axis further improving momentum resolution as well as particle identification [Nim03SSD].
- **F**orward **T**ime **P**rojection **C**hamber (FTPC): this radial drift TPC measures tracks with $2.5<|\eta|<4.0$ increasing the acceptance of STAR [Nim03FTPC].
- **E**lectro**M**agnetic **C**alorimeter (EMC): the EMC is a lead−scintillator sampling electromagnetic calorimeter in form of a barrel and an end cap calorimeter enclosing the TPC. This detector will extend the capabilities of STAR to study direct photons, certain particle species with high transverse momentum and electrons [Nim03EMC][Nim03EEMC].
- **R**ing **I**maging **CH**erenkov detector (RICH): with a relatively small acceptance this device increases the ability of STAR to identify particles at high momenta [Nim03RICH].

The read out time of most of the detectors is large compared to the bunch crossing frequency. Therefore a set of fast detectors is installed which are able to recognize when a collision has happend and provide rough information about such an event, e.g. the multiplicity around midrapidity. According to this information a trigger is issued and the slower tracking detectors are read out. The two main trigger detectors are :

- **C**entral **T**rigger **B**arrel (CTB): a barrel of 240 scintillator slats surrounding the main TPC yields information about the multiplicity [Nim03TRI].
- **Z**ero **D**egree **C**alorimeters (ZDC): two calorimeters close to the beam but 18.25 m from the main event vertex measure spectator neutrons. These measurements contain information about the z−coordinate of the event vertex as well and about the centrality [Nim03TRI] [Adl01].

If a trigger is issued, the raw data from all subdetectors are collected by the **D**ata **Ac****q**uisition system (DAQ) [Nim03DAQ] and written to tape. The DAQ is capable of writing ~30 MB/s which is equivalent to ~5 central AuAu events per second.

The design luminosity of RHIC and the readout time of the STAR tracking detectors allow an event rate up to 100 events per second. Therefore another trigger layer is introduced called "Level 3" (L3) [Nim03L3][Lan00] [Adl01][Adl02]. This trigger is based on an online analysis of the TPC data and selects events with certain rare features, e.g. an $J/\psi \rightarrow e^+ e^-$ decay candidate. In 2000 the L3 trigger capabilites were only used for monitoring purposes since RHIC design luminositiy was not reached.

3.3 The Time Projection Chamber (TPC)

The central detector in STAR is the TPC [Nim03TPC][Ret02], it is shown schematically in figure 3.3. The TPC is a barrel which is $4.2\ \mathrm{m}$ long and $4.0\ \mathrm{m}$ in diameter, sitting in a homogeneous B field along the z−axis, generated by the solenoidal magnet. The central membrane and the inner and outer cylinder of the TPC form an electrostatic field cage with a field gradient of $\approx 135\ \mathrm{V/cm}$ between the high voltage membrane at the center of the TPC and each endcap. Consequently the E field and the B field are parallel inside the TPC.

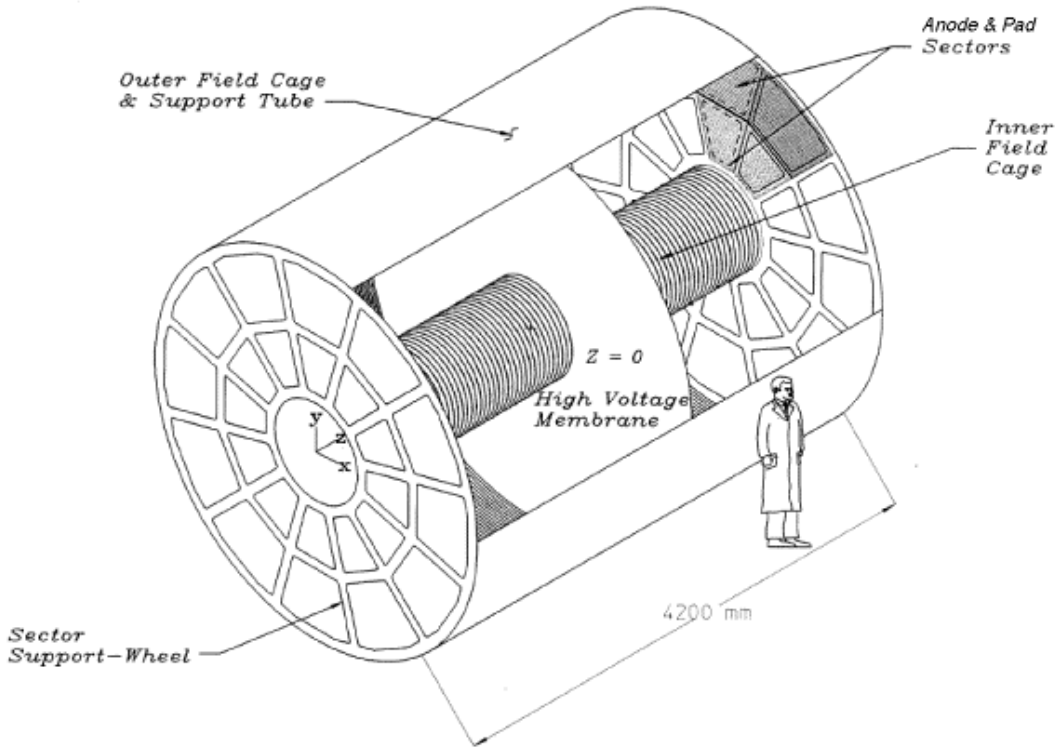

Figure 3.3

Schematic layout of the STAR TPC.

The TPC has a sensitive volume of $48\ \mathrm{m}^3$ filled with P10 gas (10% Methane, 90% Argon). A charged particle travelling through the detector ionizes the gas along its trajectory. Due to the electric field between the central membrane and the endcaps, electrons from this ionization process drift towards the anode endcaps.

The anode endcaps are organized into sectors as shown in figure 3.3 with twelfe inner and outer sectors at each end of the TPC. The readout section consists of the pad plane with three layers of wires : the gating grid, the Frisch grid and the anode grid.

A schematic layout of the read out region is shown in figure 3.4:

- The gating grid is transparent to the drift of the electrons while an event is being read out. It is closed after read out to prevent the drift of positive ions from the amplification region into the TPC drift volume.
- The Frisch grid separates the homogeneous drift field from the strongly inhomogeneous amplification field surrounding the anode wires.
- A strong inhomogeneous electric field around the anode wires accelerates electrons and generates an electron avalanche. In this way the signal is amplified several thousand times while still being proportional to the initial number of drifting electrons. Finally the anode grid absorbs all electrons.

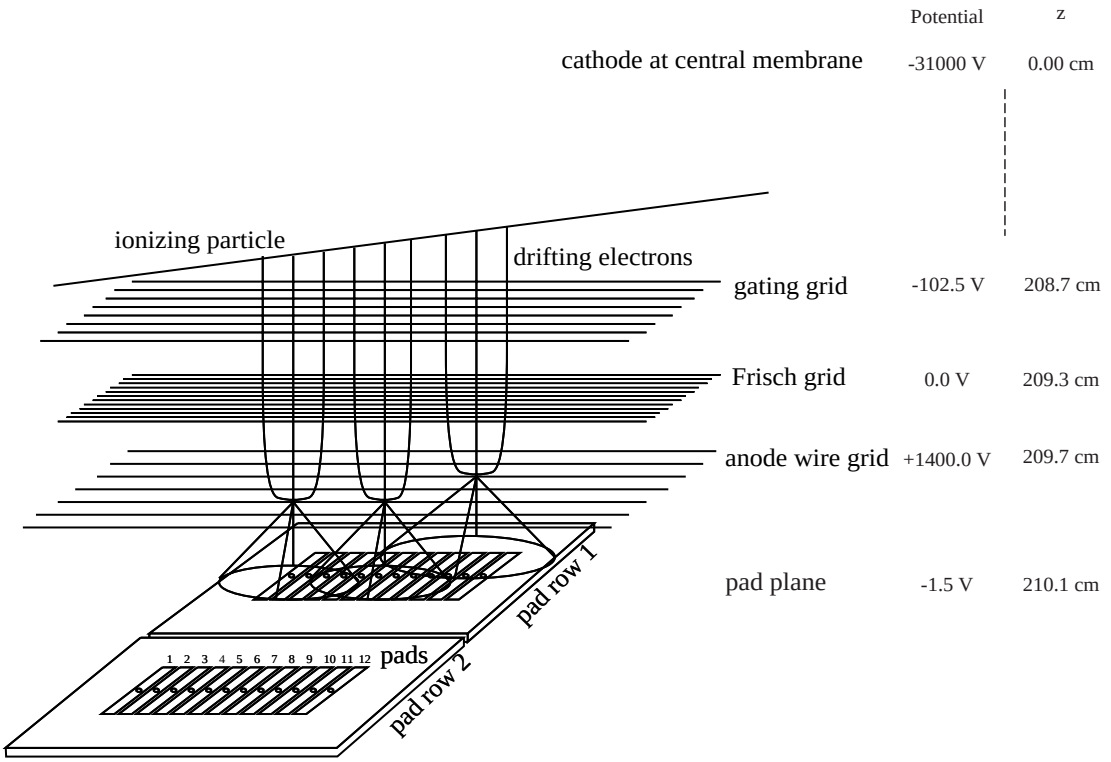

Figure 3.4

Principle of electron drift and signal amplification in a time projection chamber.

The values on the right hand side for the potential and the distance to the central membrane z are typical values for the outer sector of the STAR TPC.

- The remaining positive charge induces a signal in the pad layer. Pads are organized in rows roughly perpendicular to the expected particle track direction, as seen in the schematic drawing of the pad plane in figure 3.5. The signal of each pad is shaped and digitized. The evaluation of the signal induced in several adjacent pads allows a precise two dimensional determination of the point where the particle ionized the detector gas. The third coordinate is given by the drift time of the

electron cloud. The drift velocity of ~5.4 cm/µs and the sampling rate of ~10 MHz divide the maximum drift length of 2.09 m in up to 512 time buckets. The read out electronics assigns a 10 bit ADC value, proportional to the deposited charge, to each time bucket. The resulting pixel image of the TPC constitutes the raw data which is further processed afterwards. The average raw data size of a single AuAu event is ~6 MB after zero suppresion.

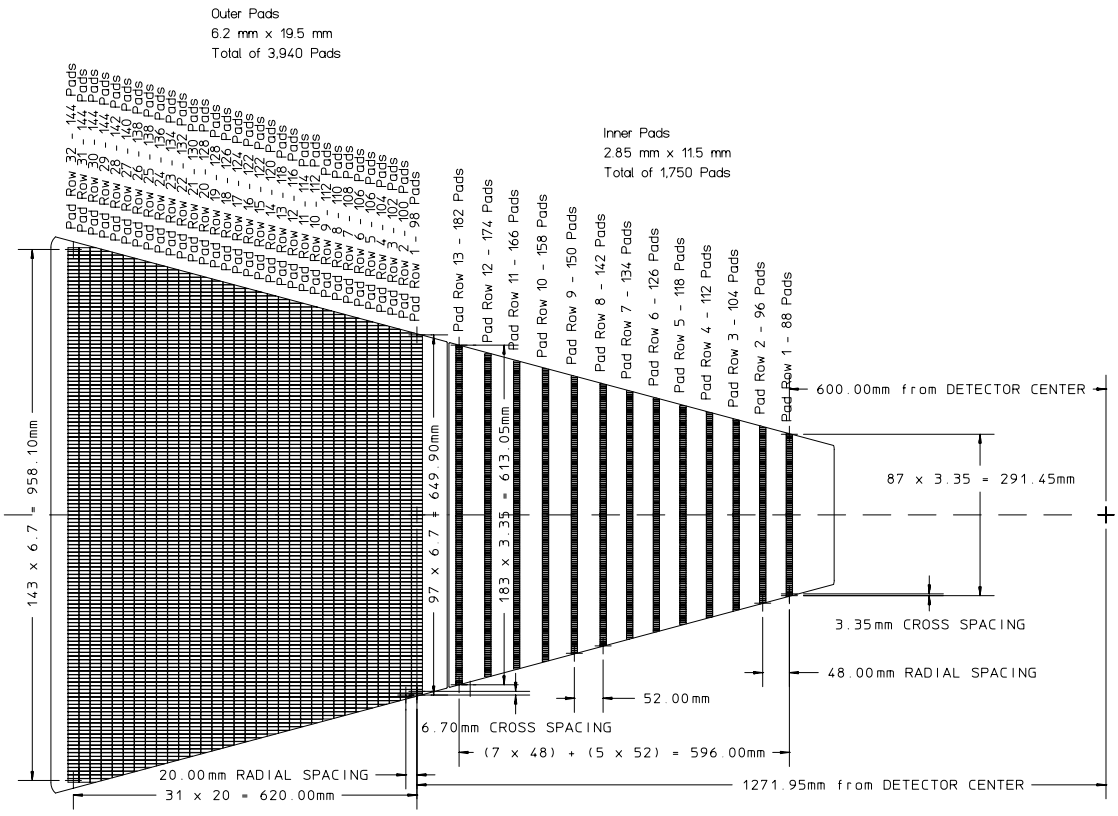

Figure 3.5

The pad plane layout of one complete sector of the STAR TPC. The inner sector (13 innermost padrows) is optimized for good two track resolution, whereas the outer sector (32 outer padrows) is optimized for dE/dx resolution.

The process of reconstructing the three dimensional positions of ionization points during the offline analysis is called cluster finding, since the drifting electron cloud is often referred to as cluster. The cluster finding algorithm applied to the TPC raw data is discussed in detail in chapter 4.1. For each ionization point the three dimensional coordinate and the total amount of charge is determined. The detected amount of charge is proportional to the energy loss of the particle travelling through the detector gas (dE/dx).
The pad plane is optimized to achieve a high momentum resolution as well as an sufficiently high dE/dx resolution. It is subdivided into an inner and outer sector. The layout for one complete sector is shown in figure 3.5.

The inner sub−sector is optimized for good two−track resolution so the readout pads are small and they are placed relatively close together in the region of the highest

track density. The pads are organized in rows that are widely separated in order to reduce the total number of electronic channels.

The track density in the outer sub−sector is lower and so the two−track resolution is not critical. Thus the pads are more densely packed to optimize the dE/dx resolution.

The size of the pads is usually optimized, according to the transverse and longitudinal diffusion of the electron cloud drifting through the detector gas which determines the width of the cluster at the anode plane [Blu93]. To achieve a sufficient precise spatial resolution without an exceedingly high number of electronic channels the pads should be approximately of the size of a typical electron cloud. The exact pad sizes are given in figure 3.5, the total number of electronic channels is:

$$\textit{total number of pads} \times \textit{number of sectors} = (3960 + 1750) \times 24 = 136560$$

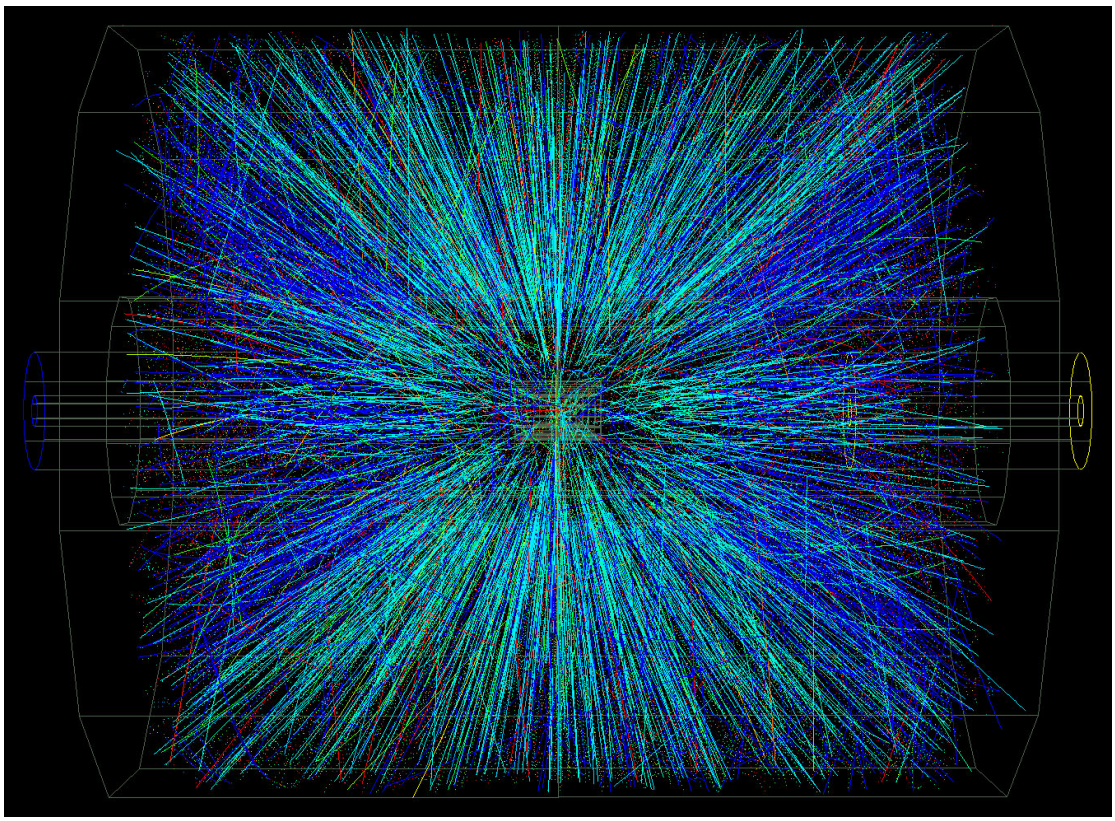

Figure 3.6

L3 online reconstructed central AuAu event with more than 10^5 *found clusters and several hundred reconstructed tracks.*

The absolute position error for any reconstructed point is below 500 µm. After all ionization points are localized by the clusterfinder a tracking algorithm is applied to reconstruct the particle trajectory. The tracking is discribed in chapter 4.1.2 in detail. The relative error between a point and a track−model fit is below 50 µm [Nim03TPC][Cal01].

Figure 3.6 shows a reconstructed central AuAu collision occuring in the center of the TPC with more than 10^5 found clusters and more than 1000 reconstructed tracks.

The parameters for the STAR TPC are summarized in table 1.

Item	**Dimension**	**Comment**
Length of the TPC	420 cm	Two halves, 210 cm long
Outer Diameter of the Drift Volume	400 cm	200 cm radius
Inner Diameter of the Drift Volume	100 cm	50 cm radius
Distance: Cathode to Ground Plane	209.3 cm	Each side
Cathode	400 cm Diameter	At the center of the TPC
Cathode Potential	28 kV	Typical
Drift Gas	P10	10% Methane, 90% Argon
Pressure	Atmospheric + 2 mB	Regulated at 2 mB
Drift Velocity	5.45 cm / μsec	Typical
Transverse Diffusion (sigma)	230 μm / √cm	140 V/cm & 0.5 T
Longitudinal Diffusion (sigma)	360 μm / √cm	140 V/cm
Number of Anode Sectors	24	12 on each end
Number of Pad Rows per Sector	45	
Total Number of Pads per Sector	5690	
Pad Size	2.85 mm x 11.5 mm	Rows 1 – 13
Anode Wire to Pad Plane Spacing	2 mm	Rows 1 – 13
Anode Voltage	1170 Volts	Rows 1 – 13
Anode Gain	3800	Rows 1 – 13
Pad Size	6.20 mm x 19.5 mm	Rows 14 – 45
Anode Wire to Pad Plane Spacing	4 mm	Rows 14 – 45
Anode Voltage	1390 Volts	Rows 14 – 45
Anode Gain	1200	Rows 14 – 45
Anode Wire Diameter	20 μm	Au plated W
Anode Wire Spacing	4 mm	
Ground Grid Wire Diameter	75 μm	Au plated Be-Cu
Ground Grid Wire Spacing	1 mm	
Gating Grid Wire Diameter	75 μm	Au plated Be-Cu
Gating Grid Wire Spacing	1 mm	
Signal to noise	20 : 1	
Electronics Shaping Time	180 nsec	FWHM
Signal Dynamic Range	10 bits	
Sampling Rate	10 MHz	
Sampling Depth	512 time buckets	380 time buckets (typical)
Magnetic Field	0, ± 0.25 T, ± 0.5 T	Solenoid
Magnetic Field Shape - limits	Uniform: ± 0.0040 T	at 0.5 T

Table 1

Critical parameters for the STAR TPC and its associated hardware.

3.4 Particle Identification

The particles most probable energy loss per unit of path length (dE/dx) is linked to its relativistic velocity β. Measuring this quantity along with the momentum allows to determine the particle mass and thus its identity.
From each padrow crossed by a track a dE/dx sample is obtained, therefore the STAR TPC provides a maximum of 45 dE/dx values per track. They are distributed according to a Landau probability distribution. Typically the highest values are discarded to reduce the fluctuations from the long Landau tail. In STAR usually the 30% highest values are discarded. From the remaining samples a mean value for the energy loss per unit path length is calculated. The measured truncated mean values for negatively charged particles pointing back to the main vertex are shown as a function of momentum in figure 3.7.

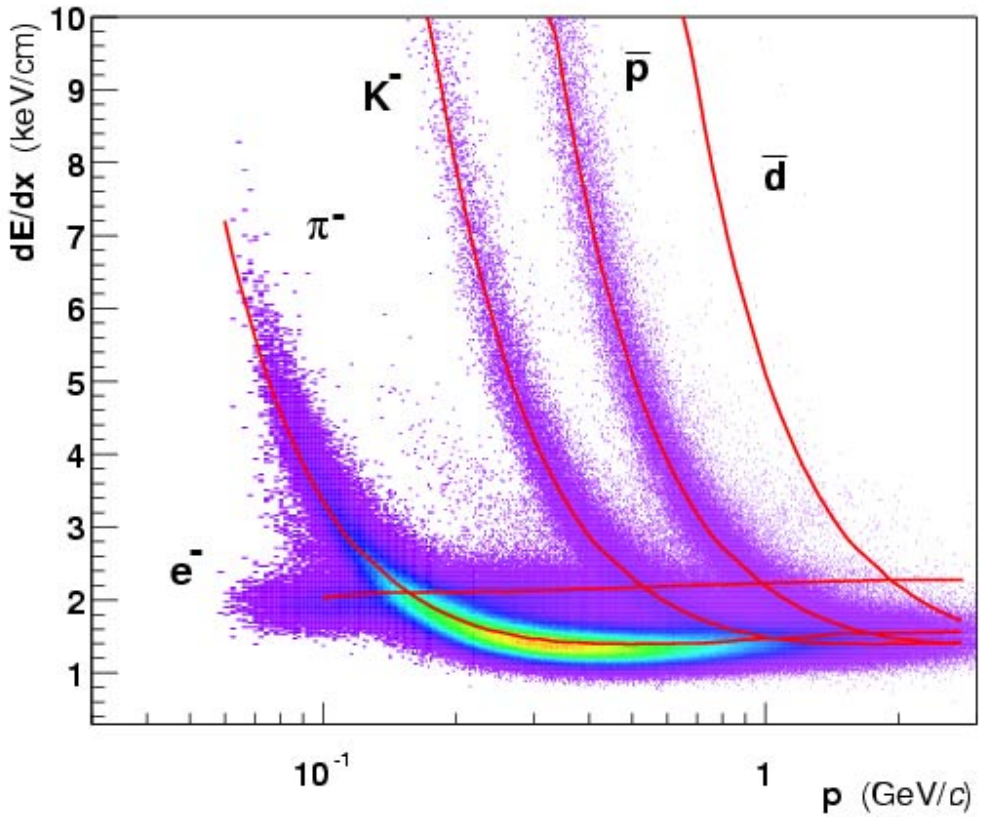

Figure 3.7

The dE/dx versus momentum distribution shows charateristic bands for electrons pions, kaons, protons and deuterons. Red lines indicate the values for these particle species calculated from the Bethe Bloch equation.

The curves in figure 3.7 indicate the expected ionization energy loss for different particle species hypotheses according to the Bethe Bloch equation [Blu93]

$$-\frac{dE}{dx}=\frac{4\pi N e^4}{m_e c^2}\frac{1}{\beta^2}z^2\left(\ln\frac{2 m_e c^2}{I}\beta^2\gamma^2-\beta^2-\frac{\delta(\beta)}{2}\right)$$

with

N = number density of electrons in the matter traversed

z = charge of travelling particle

$m_e c^2$ = rest energy of the electron

β = velocity of the travelling particle

$$\gamma=\frac{1}{1-\beta^2}$$

I = mean excitation energy of the atoms of the chamber gas

$\delta(\beta)$ = relativistic medium polarization term

The measured dE/dx resolution [Cal01]

$$\frac{\sigma_{dE/dx}}{dE/dx}\approx 8.8\%$$

allows at low momenta a separation of pions from all other species except for electrons. The contamination of identified pions with electrons is in the order of a few percent and thus not critical for this analysis [Cal01].

4. Experimental data set

4.1 Event reconstruction

The raw data from the subdetectors are analyzed by an offline analysis chain. Several steps are necessary to reconstruct trajectories of particles traversing the various detectors. Here we will focus on reconstruction and analysis of TPC data only.

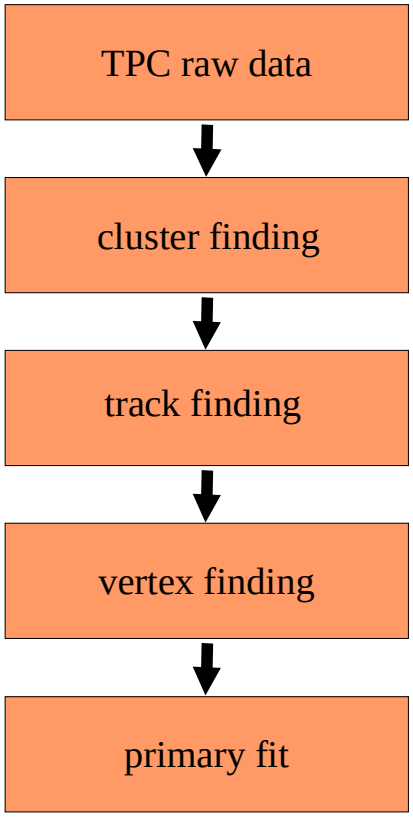

Figure 4.1

Steps of the event reconstruction.

The main steps of event reconstruction are sketched in figure 4.1. The cluster finder algorithm converts TPC raw data to space points. These are input to the tracking algorithm. A particle trajectotry appears as a chain of ionization points pointing toward the event vertex in the detector center. The tracking algorithm recognizes

typical track patterns and connects points from up to 45 pad rows. Every set points associated with a track is fitted with a helix model. Using the helix parameters the track is extrapolated to the beam axis. Combining extrapolations from all tracks the vertex position is calculated. Finally all tracks pointing back towards the vertex are fitted again, now using the vertex as additional point on the track.

4.1.1 Cluster finding

A typical cluster spreads over several time bucktes on adjacent pads. The cluster finder algorithm [Lis96] searches for contiguous regions of deposited charge, i.e. ADC values above a threshold, in the pad−time plane. Figure 4.2 shows typical ADC values in the pad−time plane and found cluster centroids.

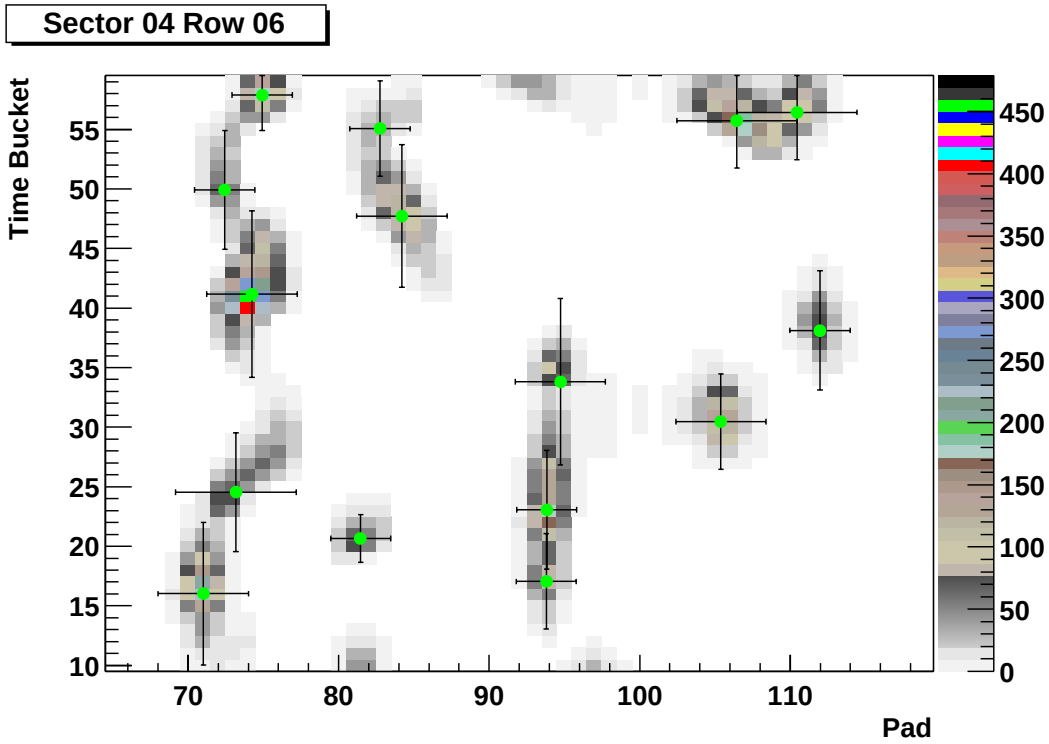

Figure 4.2

ADC pixel in the pad−time plane. ADC values can be decoded using the colour code on the right hand side. Green symbols indicate cluster centroids, black bars calculated cluster widths.

Trajectories of particles with small momentum difference are close in space, hence clusters from two different tracks can overlap. Therefores the cluster finder algorithm searches for maxima in a contiguous region of deposited charge. If only one

maximum is found the cluster is assumed to originate from a single separated track. In case that more maxima are found, a deconvolution procedure is used to separate contributions from different tracks. For each maximum the width of the cluster is calculated as well as its total charge.

The deconvolution procedure cannot resolve clusters that are too close. The efficiency is defined as the ratio of the distributions of the distance separating two clusters from the same event and two clusters from different events. The cluster finding efficiency in pad and time direction is shown in figure 4.3. It reaches a plateau if the clusters are separated more than 1.5 cm in pad direction and more than 3.0 cm in (drift−) time direction.

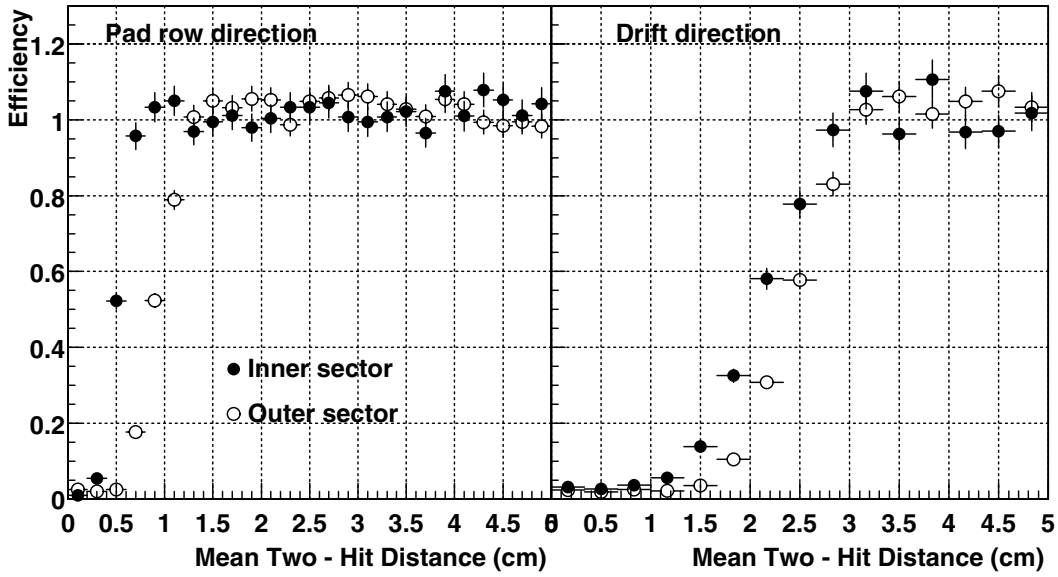

Figure 4.3

Cluster finding efficiency as a function of separation for inner and outer sector [Nim03TPC].

Clusters are more likely to overlap at the innermost padrows, because the track density is higher at padrows closer to the beam. Therefore the pad design is different in the inner and in the outer sector. And consequently the efficiency is different for the inner and outer TPC sector. Figure 4.4 shows found clusters on a padrow in the inner sector (upper panel) and in the outermost padrow (lower panel) in the same event.

Cluster centroids in pad−time space are converted to points in real space using the measured drift velocity and detector geometry. The transformation takes trigger time offsets, detector geometry, electronics response and field inhomogeneities into account. The resulting set of cluster coordinates including the deposited amount of charge is propagated to the track finder algorithm.

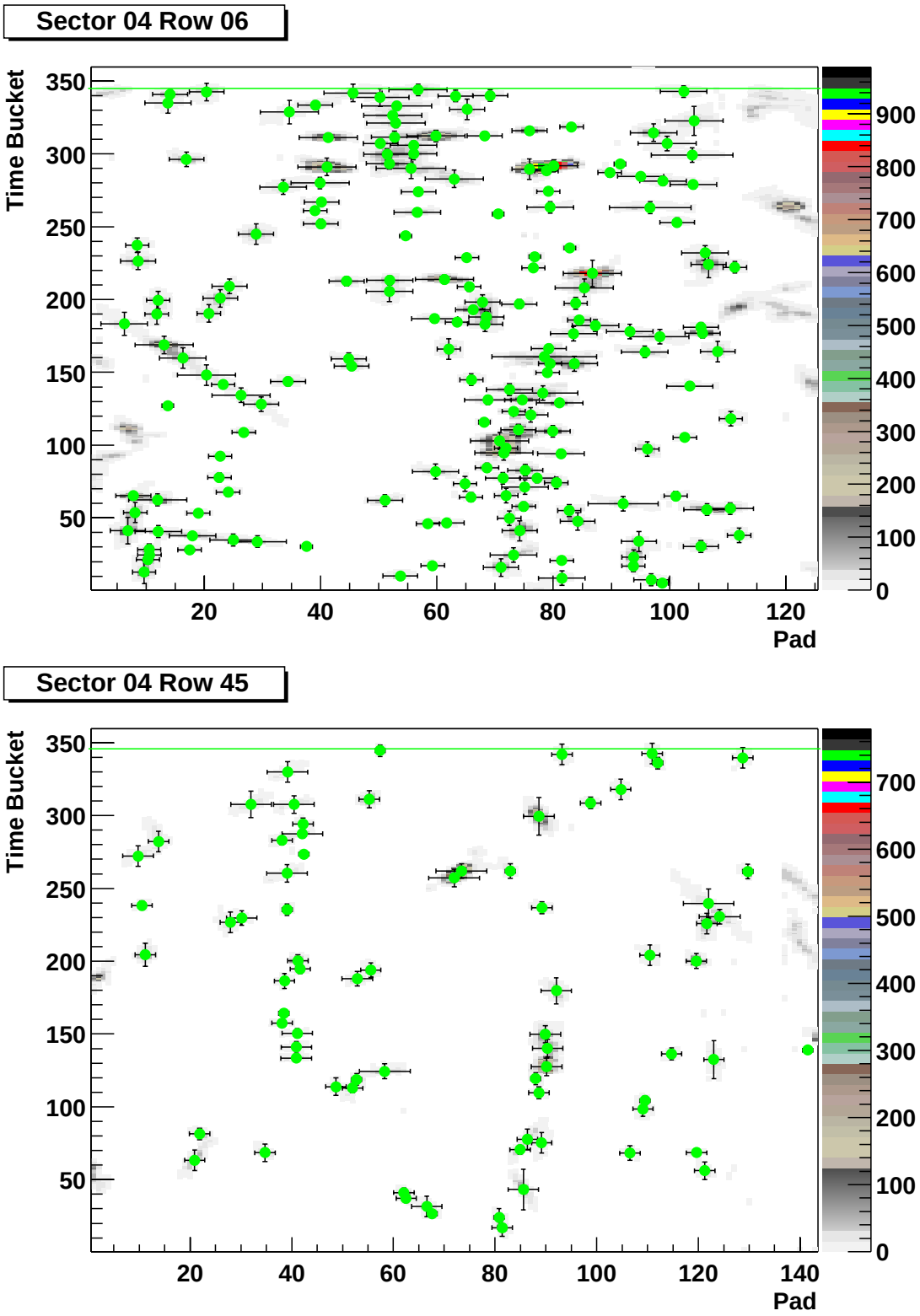

Figure 4.4

ADC values (according to the colour code on the right hand side) and clusters (green symbols) in the pad−time plane. Upper panel: row 6 in the inner sector. Lower panel: row 45 in the outer sector. In the year 2000 setting the maximum drift length was divided into 348 time buckets (green line).

4.1.2 Tracking

The tracking algorithm for the TPC starts from the outermost padrows. Clusters close in space and from successive padrows form track seeds. Using a follow−your−nose approach these seeds are expanded with clusters from padrows closer to the beam. The produced collections of space points associated with a track are called segments. They are fitted with a helix model taking into account multiple scattering and energy loss in the detector gas. Using the fit parameters the segments can be extrapolated and segments obviously belonging to the same track are merged.

The next step is called global track fit. Track information from different subdetectors are matched in this procedure. The dataset analysed here is based on the TPC, in this case only tracks from different TPC sectors are matched.

All global tracks are used to determine the primary vertex. Since the vertex can only be a few millimeters away from the beam axis it is found by projecting global track vectors on the transverse plane. Minimizing the distance of all projections to a point yields the main event vertex.

The vertex resolution is shown in figure 4.5. It is calculated by comparing the position of vertices reconstructed using each side of the TPC separately. The resolution increases with the number of tracks. For events with more than 800 tracks it is below 400 μm.

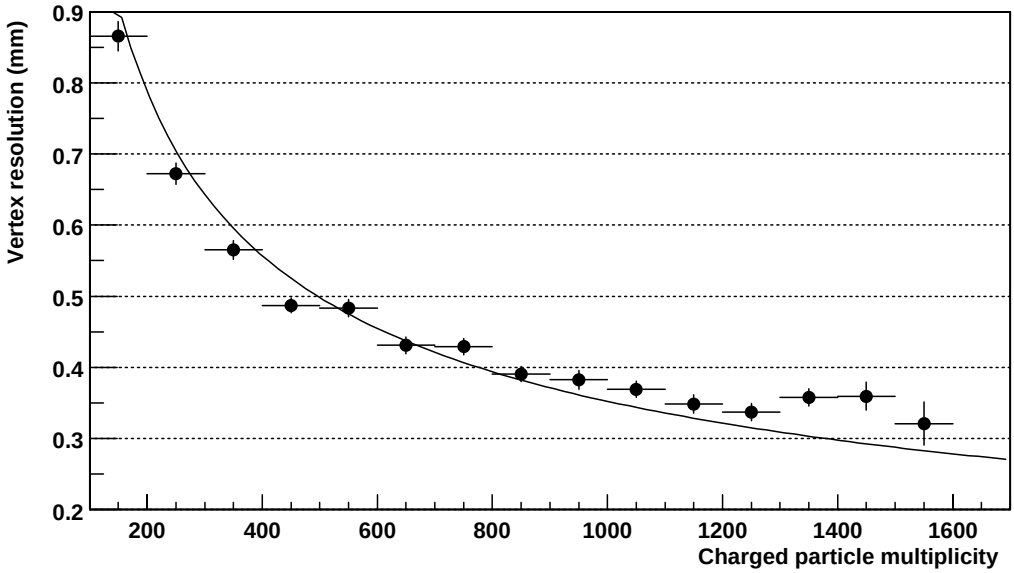

Figure 4.5

Vertex position resolution as a function of event multiplicity [Nim03TPC].

Global tracks whose distance at closest approach to the vertex is less than 3.0 cm are refitted with the vertex as additional point on track. Refitted tracks are called primaries since it is assumed that the respective particles were produced directly at the interaction. Extrapolations of tracks from decay products do usually not point

back to the vertex, therefore they are treated differently. Since for HBT analyses only particles coming directly from the collision region are relevant we concentrate on primaries.

The helix fit is done by two simultaneous two dimensional fits. The projection of a helix on a plane perpendicular to its axis yields a circle where the curvature corresponds to the inverse transverse momentum of the particle in the magnetic field. For a given curvature the bend plane is defined by the vector of the path length of the helix and a vector parallel to the z−axis. In this plane helixes appear as straight lines [Cal01]. Performing a circle fit in the transverse plane and simultaneously a straight line fit in the bend plane the helix parameters are obtained.

Momentum resolution is a crucial value for each tracking device. In this case it is determined by embedding Monte Carlo tracks into real events, running the whole reconstruction chain and comparing the reconstruction with the input. Embedding means to simulate the interaction of a particle with the detector gas, the drift of electron clouds and the complete read out process. Comparing shape and residuals, i.e. distances of cluster centroids to track helixes, from simulated to measured clusters ensures a realistic simulation. The uncertainty in momentum assignment is dominated by the error in the curvature fit [Blu93], hence the relative transverse momentum resolution

$$\frac{\Delta p_\perp}{p_\perp} = \frac{\left| p_{\perp,\,\text{reconstructed}} - p_{\perp,\,\text{embedded}} \right|}{p_{\perp,\,\text{embedded}}}$$

is determined to estimate the the quality of the reconstruction. As shown in figure 4.6 it is roughly 2% for all momenta between 0.2 and 0.6 GeV/c.

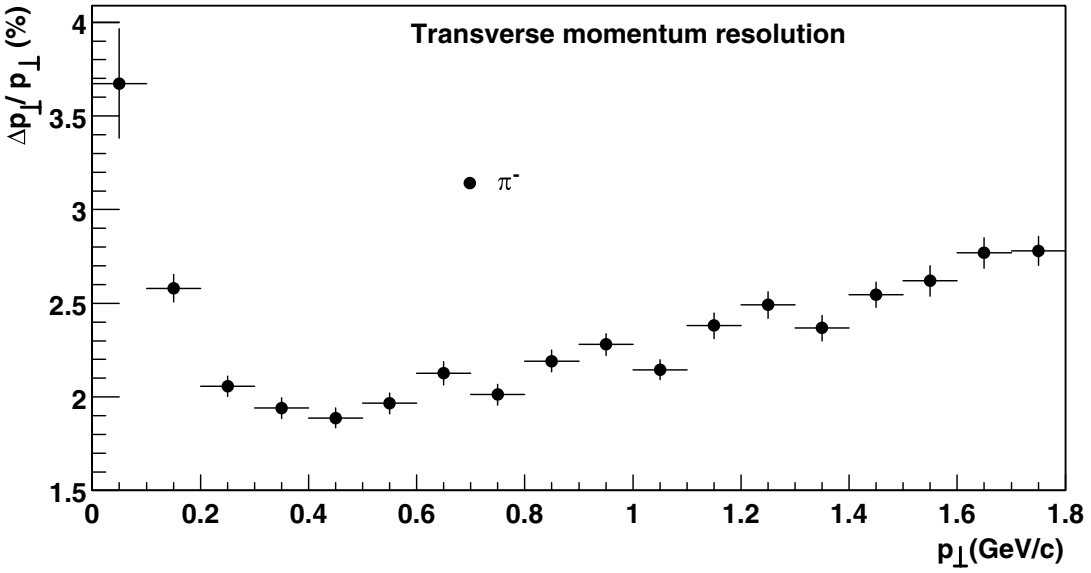

Figure 4.6

Transverse momentum resolution as a function of transverse momentum [Nim03TPC].

Although the STAR TPC completely surrounds the interaction region, not every

charged particle leaves a detectable signal. For example trajectories crossing the sector boundaries cannot be reconstructed completely since clusters are lost in these regions. Also a number of pions decay and hence cannot be detected. The fraction of particles that can be detected is called acceptance. The acceptance of negatively charged pions is displayed in figure 4.7.a. It reaches more than 90% for particles with transverse momenta above 0.300 GeV/c [Cal01].

Another key value for the tracking is its efficiency. It is defined as the ratio of the number of reconstructed tracks that could be matchted to an embedded track over the number of all embedded tracks. In figure 4.7.b the efficiency for negatively charged pions in central events is displayed. The efficiency depends on the momentum parameter of embedded tracks. For higher momenta a plateau of 80% is reached. Low momentum tracks spiral up inside the TPC and do not reach the outer field cage. In addition, these low momentum particles interact with the beam pipe and the inner field cage before entering the tracking volume of the TPC. Hence the efficiency for low momentum tracks drops rapidly.

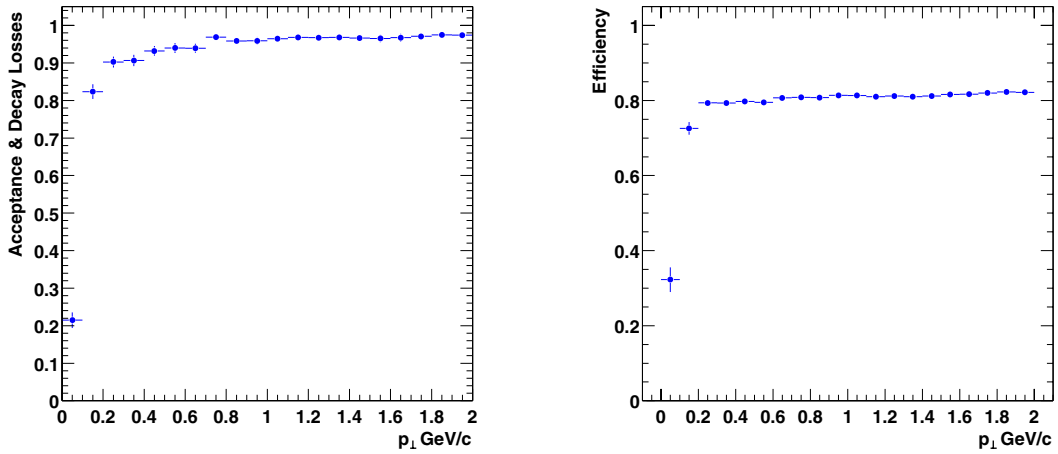

Figure 4.7

a.) lhs: pion acceptance for central events.

b.) rhs: pion reconstruction efficiency for central events [Cal01].

4.2 Event selection

In this analysis we use only events with a small impact parameter. During the year 2000 run these central events were triggered by a combination of the ZDC and CTB detectors. As the impact parameter decreases, the number of forward spectator neutrons grows rapidly, eventually saturating and then decreasing for small impact parameters. At the same time, the CTB multiplicity increases, with the most central collisions corresponding to high CTB multiplicity and a small number of forward spectator neutrons. Figure 4.8 shows the correlation between CTB and ZDC, the central trigger requires a minium multiplicity from the CTB and a maxium number of spectator neutrons in the ZDC. In total 362689 events with this trigger condition were accepted for physical analyses.

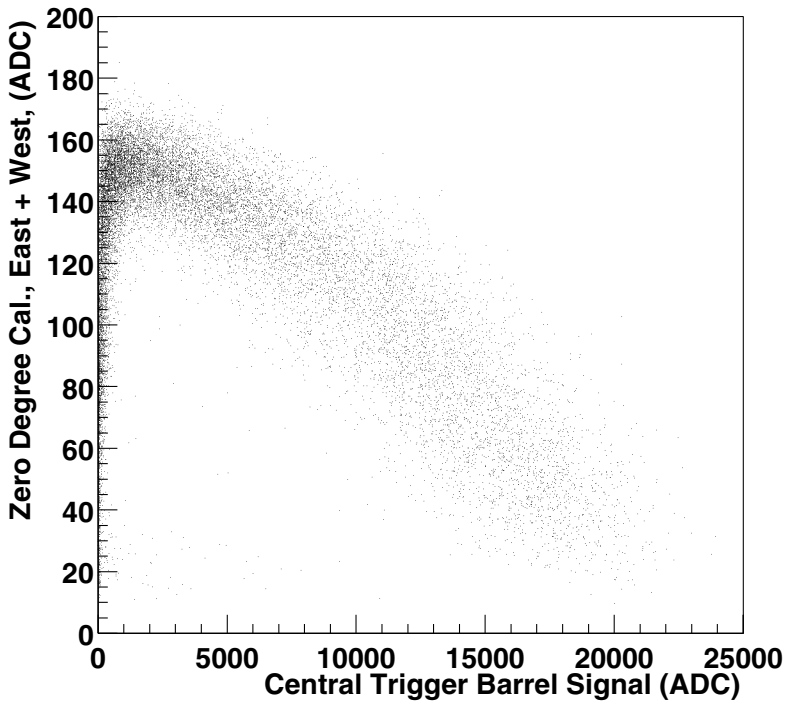

Figure 4.8

ZDC versus CTB signal. For central events only a small number of spectator neutrons is measured in the ZDC, but a high multiplicity is detected by the CTB [Har01].

Between ~700 and ~1800 tracks traversing the TPC are reconstructed for each central event, the corresponding distribution is displayed in figure 4.9.a. The centrality is closely related to the multiplicity of particles. A Glauber model study [e.g. Won94] allows to specify this relation and to select a certain impact parameter range. To determine the centrality in this analysis we use the number of reconstructed negatively charged primary tracks in the pseudorapidity range $|\eta|<0.5$ which have more than nine TPC points on track. The distribution of the number of tracks per

event fulfilling these criteria is shown in figure 4.9.b. Accepting only events that have more than 174 of those tracks yields the 12% most central events [Cal01].

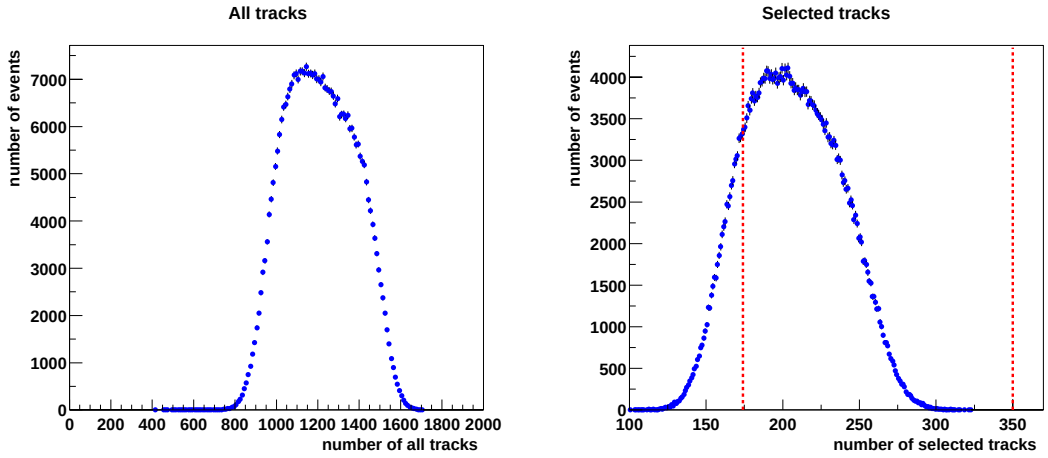

Figure 4.9

a.) lhs: number of all reconstructed TPC tracks per event.

b.) rhs: number of tracks used to determine the centrality, red lines indicate the 12% most central events.

Because of the large interaction diamond in the 2000 run the event vertex is spread over a wide range in z direction. The distribution of the vertex position is shown in figure 4.10. The detector is optimized for events occuring in the center of the TPC, therefore events more than 0.5 m away from the detector center are rejected.

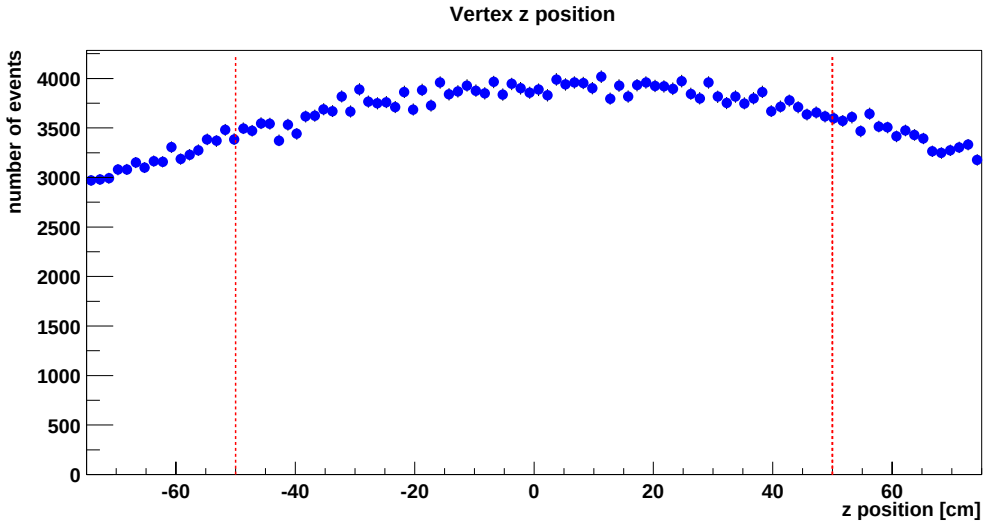

Figure 4.10

Vertex position in z−direction. Red lines indicate events close enough to the detector center, only these are accepted for this analysis.

The distribution of the main vertex position in the x−y plane is shown in figure 4.11.

The profile of the beam yields a width of this distribution of $\mathrm{RMS} \approx 500\,\mu\mathrm{m}$ in x− and y−direction. The distributions show an offset of a few millimeters of the beam from the nominal position at (0,0). This shift has no impact on efficiency or acceptance, since events are accepted independent on the x−y position of their vertex.

After the z−vertex position cut and the centrality cut, the total number of events accepted for this analysis is 206789.

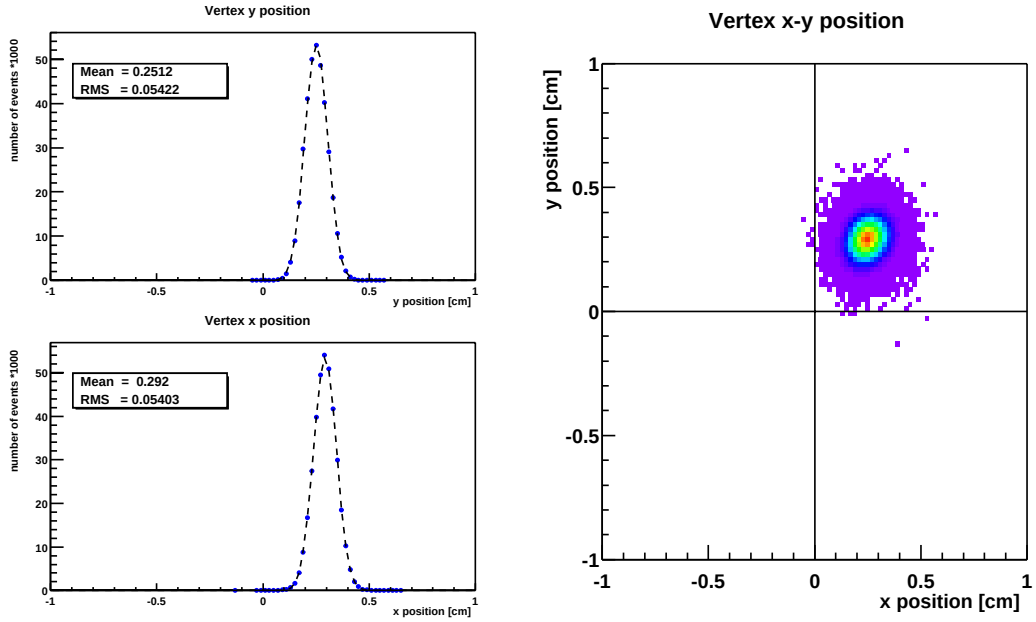

Figure 4.11

Vertex position in x−y plane. Both beams were shifted from the nominal position at (0,0), yielding an offset of the mean vertex position.

4.3 Track selection

The maximum number of points associated with a track depends on its orientation relative to the detector as well as on its curvature. Malfunctions in the readout electronics as well as reconstruction inefficiencies can cause loss of individual points on track. Figure 4.12 shows the distribution of the number of points that were used to fit the track. Only tracks with a minimum of 10 hits were accepted. According to the number of padrows per sector, a maximum of 45 points per track is possible. Most of the tracks are well defined by more than 25 hits. The large fraction of tracks that have less than 13 hits, originates mainly from the sector layout. The gap between the inner and outer sector makes the track finding algorithm split some tracks at this boundary.

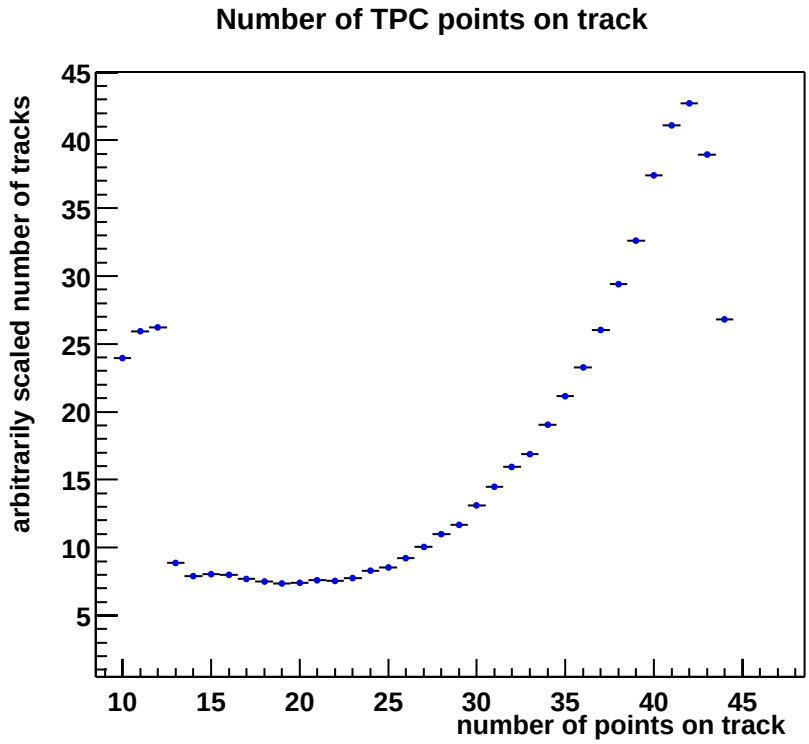

Figure 4.12

Number of TPC points on track.

The **d**istance at **c**losest **a**pproach (DCA) of the track helix to the vertex is calculated for every track before the final helix fit when the vertex is included as an additional point on track. Only tracks with a DCA below 3.0 cm are accepted as primary tracks. The DCA of most of the tracks is only a few millimeters (figure 4. 13) which reflects the accuracy of the space resolution of the TPC as well as the quality of the reconstruction chain.

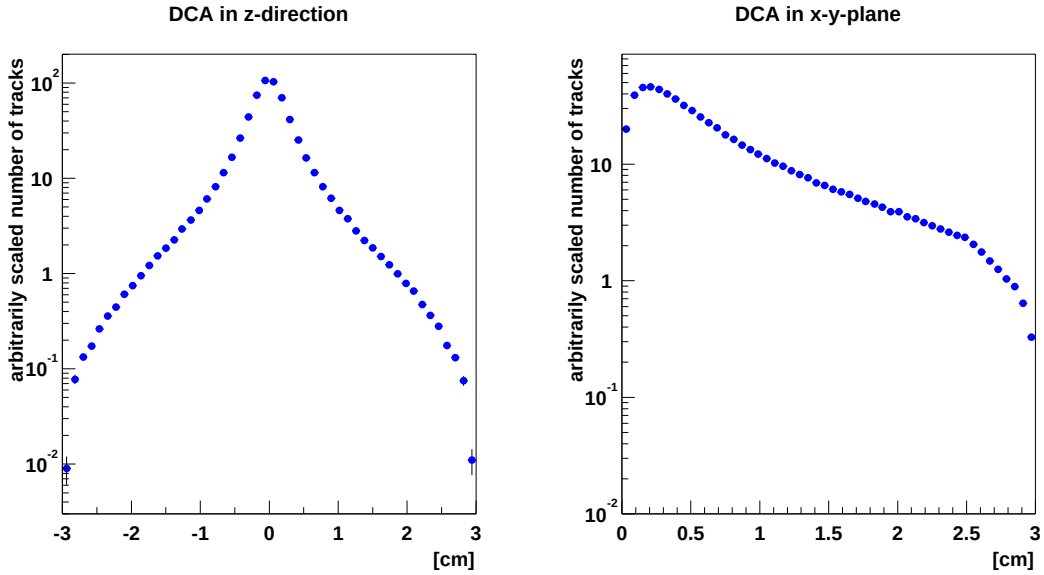

Figure 4.13

Distance at closest approach of the track helix to the vertex before the final fit.

The distribution of the momentum components in all three space directions is shown in figure 4.14. All distributions are centered around zero. The width of the uncorrected yields transverse to the beam in x− and y−direction is about 0.45 GeV/c, whereas in longitudinal direction it is about 0.50 GeV/c. The dip in the transverse distributions at very small momenta is due to the small efficiency and acceptance for particles with small transverse momentum.

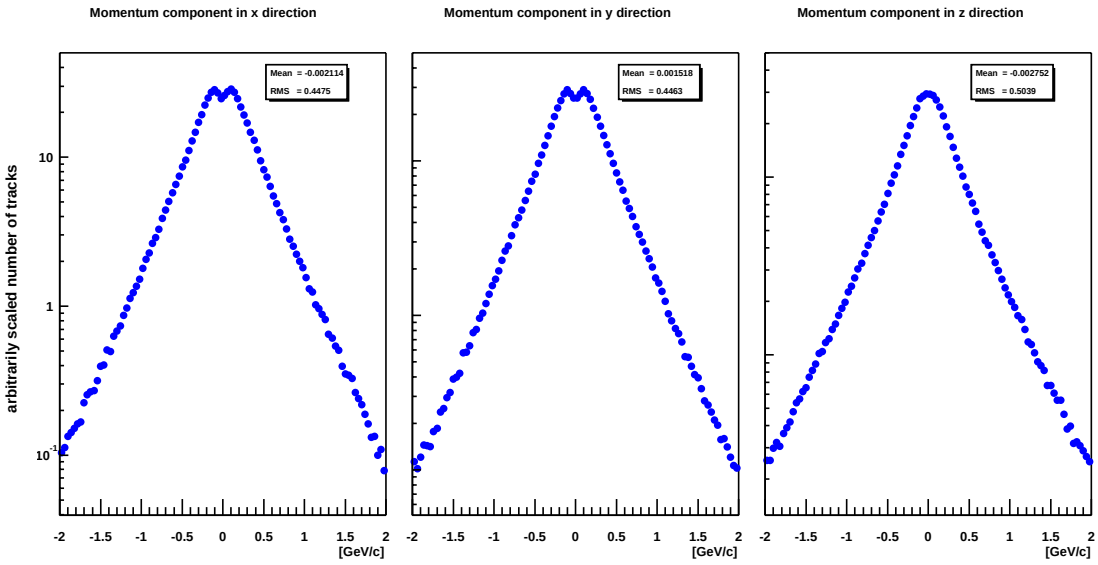

Figure 4.14

The momentum distribution of primary tracks in x−, y− and z−direction.

The corresponding transverse momentum and pion rapidity distributions are shown in figure 4.15. Particle momentum cuts are applied only in these variables. To avoid uncertainties due to the low tracking efficiency and acceptance in the low transverse momentum range only particles with p_t above 0.125 GeV/c are accepted.

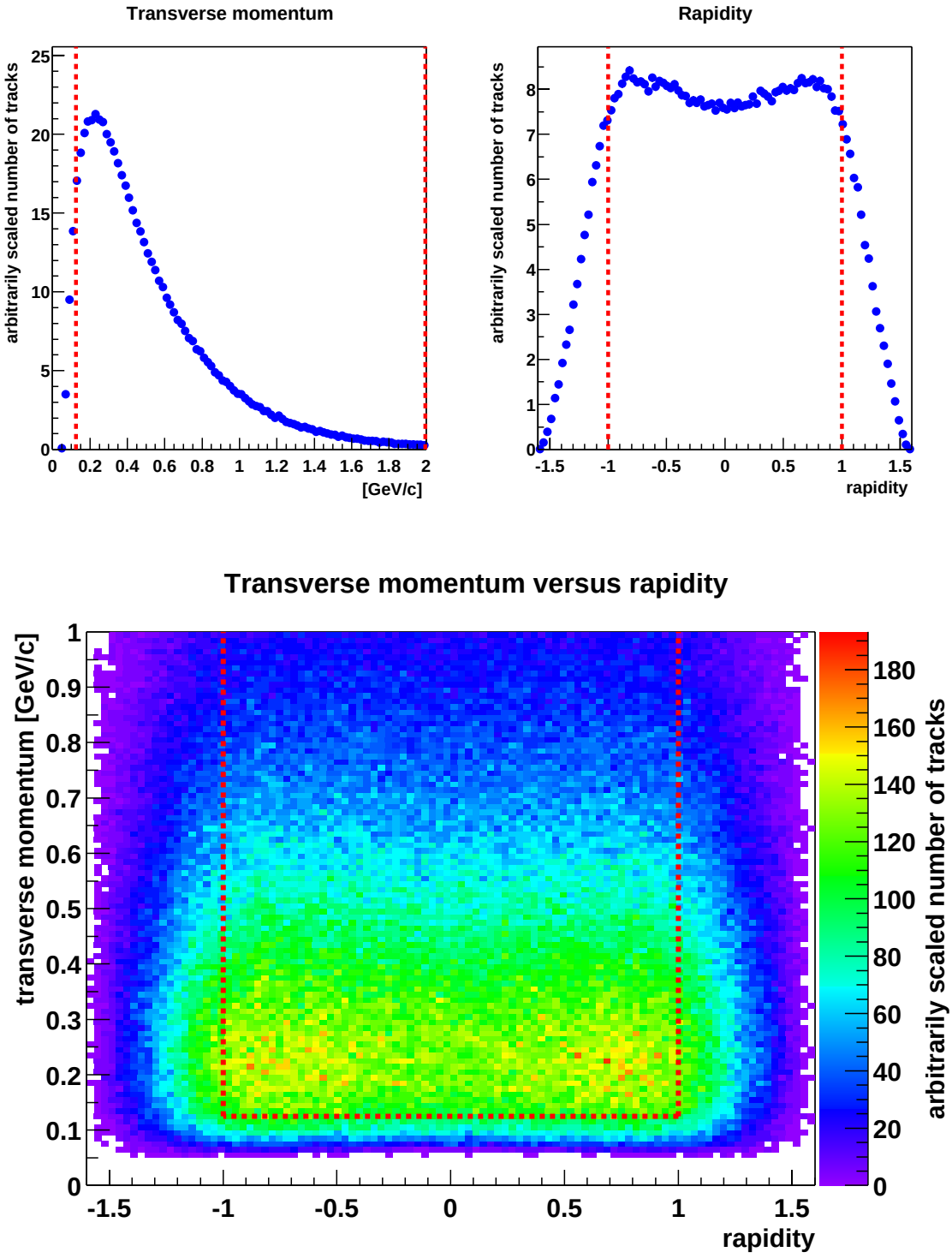

Figure 4.15

Rapidity and p_t distribution. Red lines indicate accepted tracks.

For the same reason, only particles less than one unit of rapidity away from midrapidity are accepted. Particles with high transverse momentum do not contribute to the correlation function, since particle pairs with low momentum difference are very rare in this region. Therefore high p_t particles with more than 2.0 GeV/c are rejected. The idea here was to accept as many tracks as possible since further cuts will be applied to the pair momentum.

Pions are the most frequently produced particles in an ultra relativistic heavy ion collision, but also a number of other particles e.g. electrons, kaons or protons are emitted. To select tracks that correspond most probably to pions, the energy loss per unit path length in the detector gas is used. For a given particle momentum and a given particle species, the most probable energy loss per unit path length in the detector gas can be calculated (see chapter 3.4). The measured dE/dx values are distributed around the most probable value. If the measured value is more than 3 standard deviations away from the most probable dE/dx value for a pion of the same momentum, it is assumed that the track originiates not from a pion and hence it is rejected. In figure 4.16 the distance to the most probable dE/dx value for pions with the same momentum is shown in units of standard deviations.

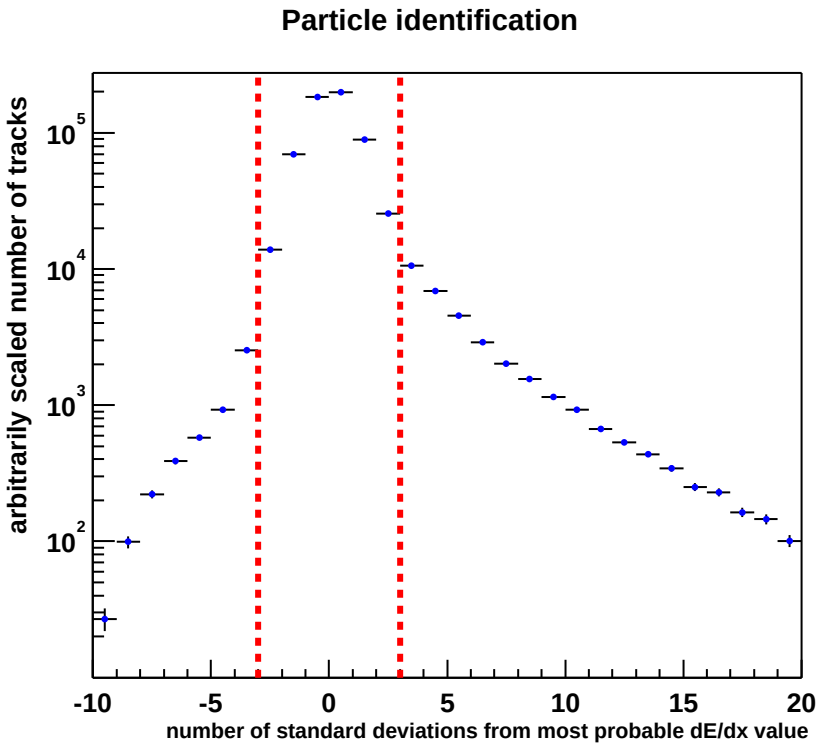

Figure 4.16

Particle identification: number of standard deviations away from the most probable energy loss per unit path length for a pion of this momentum. Red lines indicate the cut values.

From figure 3.7 it is obvious that this method allows to separate pions from kaons and protons, but there will be a fraction of electrons which are misidentified as pions. For this analysis we neglect contributions from misidentified particles. After all track cuts

we find on average ~543 π^- and ~550 π^+ per accepted event which are used to construct the correlation functions.

4.4 Pair selection

Events passing the cuts defined in 4.2 and tracks meeting the criteria defined in 4.3 are used to produce the $k_t - Y_{\pi\pi}$ distribution shown in figure 4.17. The correlation function is calculated in different kinematic regions, because its dependence on pair momentum contains valuable information, e.g. the dependence on transverse pair momentum allows to observe transverse flow. The two dimensional distribution is subdivided into five bins in longitudinal pair rapidity $Y_{\pi\pi}$ and into four bins in transverse pair momentum k_t. This choice ensures a sufficient number of pairs in each bin to observe the HBT correlation and to study the dependence of the correlation function on k_t and $Y_{\pi\pi}$.

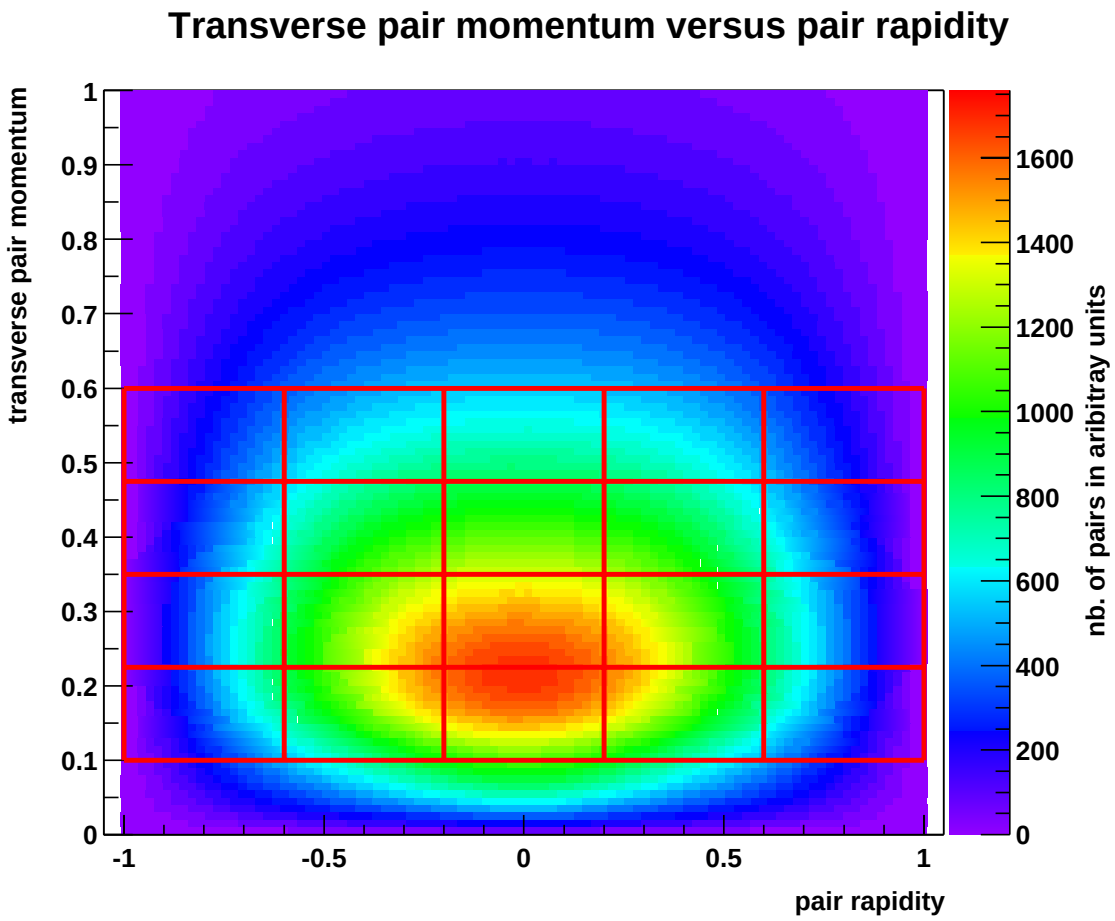

Figure 4.17

Tranverse pair momentum versus pair rapiditiy. Red Lines indicate the twenty bins into which the event sample is subdivided.

4.4.1 Entrance separation cut

If two particle trajectories in the TPC lie too close, their clusters overlap and the analysis chain possibly reconstructs a single track instead of two. This effect occurs only in the signal distribution, not in the mixed event background, where the two tracks are taken from different events.

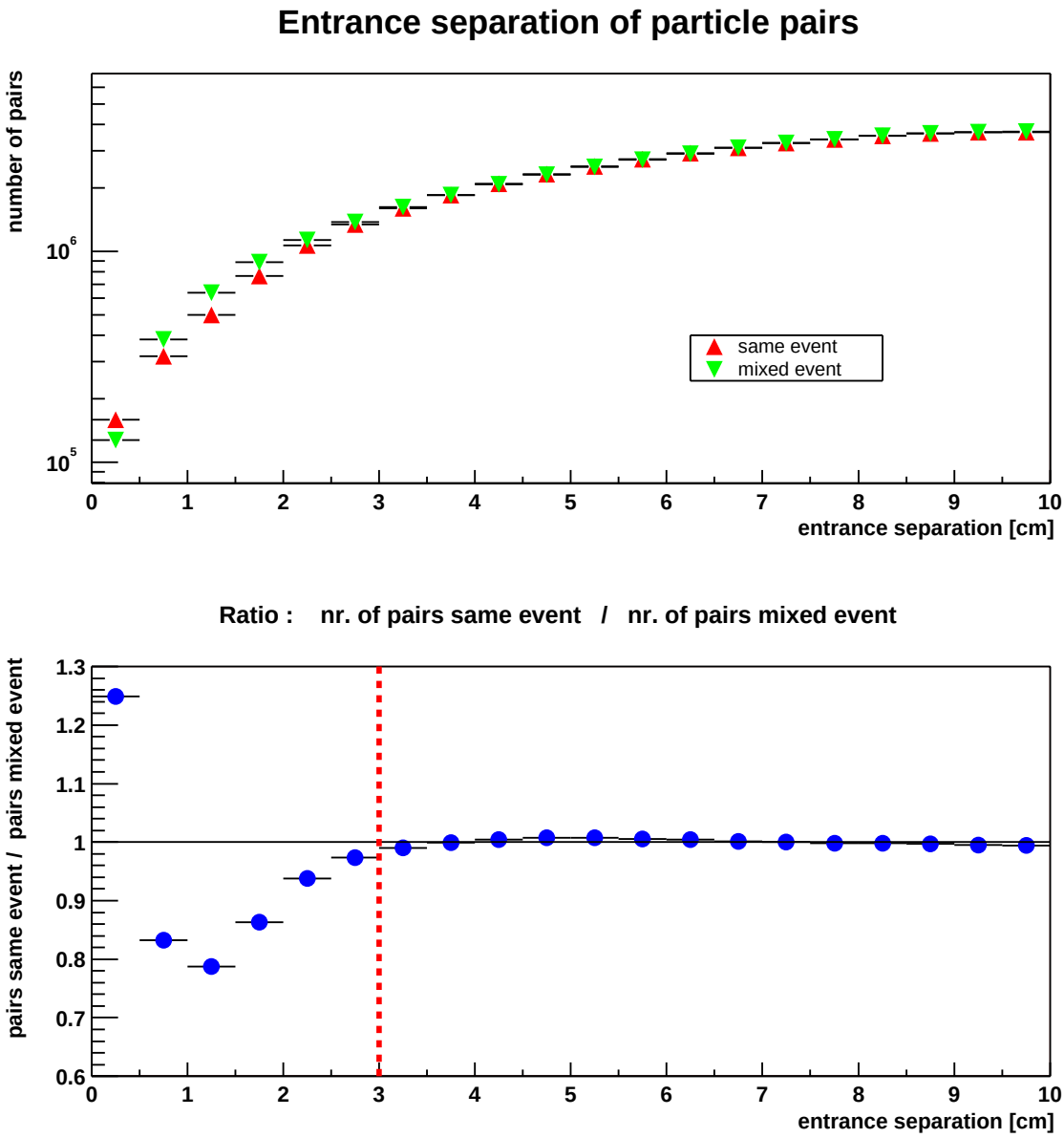

Figure 4.18

a.) upper panel : entrance separation for pairs from the same event and for pairs from mixed events where the mixed event distribution is scaled down.

b.) lower panel: ratio of entrance separation distriubtions. The red line indicates the cut value.

Especially pairs of low momentum difference are affected since they are necessarily close in space. The loss of particle pairs in the signal distribution compared to the mixed event background alters the correlation function in the region of low momentum differences where the HBT effect is observed. To reduce the impact of the finite two track resolution we reject pairs that are too close in space in the signal and likewise in the background distribution. A measure for the distance of two tracks is the nominal entrance separation, which is the spatial distance between the two points where two particles hit the inner field cage.

Figure 4.18.a shows the nominal entrance separation distribution for pairs with tracks from the same event and for pairs with tracks from different events. Only pairs with low momentum difference $q_{inv} < 0.1\,GeV/c$ are accepted. The background is scaled by the ratio of the total number of pairs in the signal to the total number of pairs in the background. The ratio of the two distributions is displayed in figure 4.18.b. We reject pairs that have less than 3.0 cm entrance separation. The same ratio in different $k_t - Y_{\pi\pi}$ bins is given in appendix A, similar distributions are obtained in all momentum regions.

For pairs of very low entrance separation the ratio increases, reaching even values above unity. This behaviour is mainly due to split tracks which are discussed in the next section.

4.4.2 Split track cut

Due to inefficiencies in the cluster finder and track finder algorithms the reconstruction chain produces split tracks. These are track segments in the TPC belonging to the same particle, which are identified as stemming from two independent particles. The relatively large number of tracks with a small number of hits, shown in figure 4.12, is partly due to this effect.

If a track is split, it is reconstructed as two tracks with small momentum difference. Therefore the correlation function is altered in the momentum region which is relevant for HBT. To eliminate pairs consisting of split tracks belonging to the same particle we use the track topology. For each pair a quality factor is calculated in the following way: If both tracks have a hit in a pad row, (−1) is added to the running split quality. If only one track has a hit in a pad row, (+1) is added to the running split quality. After the sum of the split quality is made for the 45 pad rows in the TPC, the number is divided by the sum of the hits in both tracks. This normalizes the split quality to an interval from (−0.5) to (1.0).

In figure 4.19 the distribution of the split quality factor is shown for pairs with small momentum difference: $q_{inv} < 0.1\,GeV/c$ (the ratio in individual $k_t - Y_{\pi\pi}$ bins is given in appendix A). If a pair is made from two split tracks belonging to the same particle, the overlap of the two tracks will be small and hence the quality factor close to 1.0. Comparing the quality factor of pairs of tracks from the same event with pairs of

tracks from different events an enhancement in the ratio is visible for pairs with a quality factor larger than 0.8. To reduce the impact of track splitting we reject pairs with a quality factor above 0.8 in the signal as well as in the background distribution.

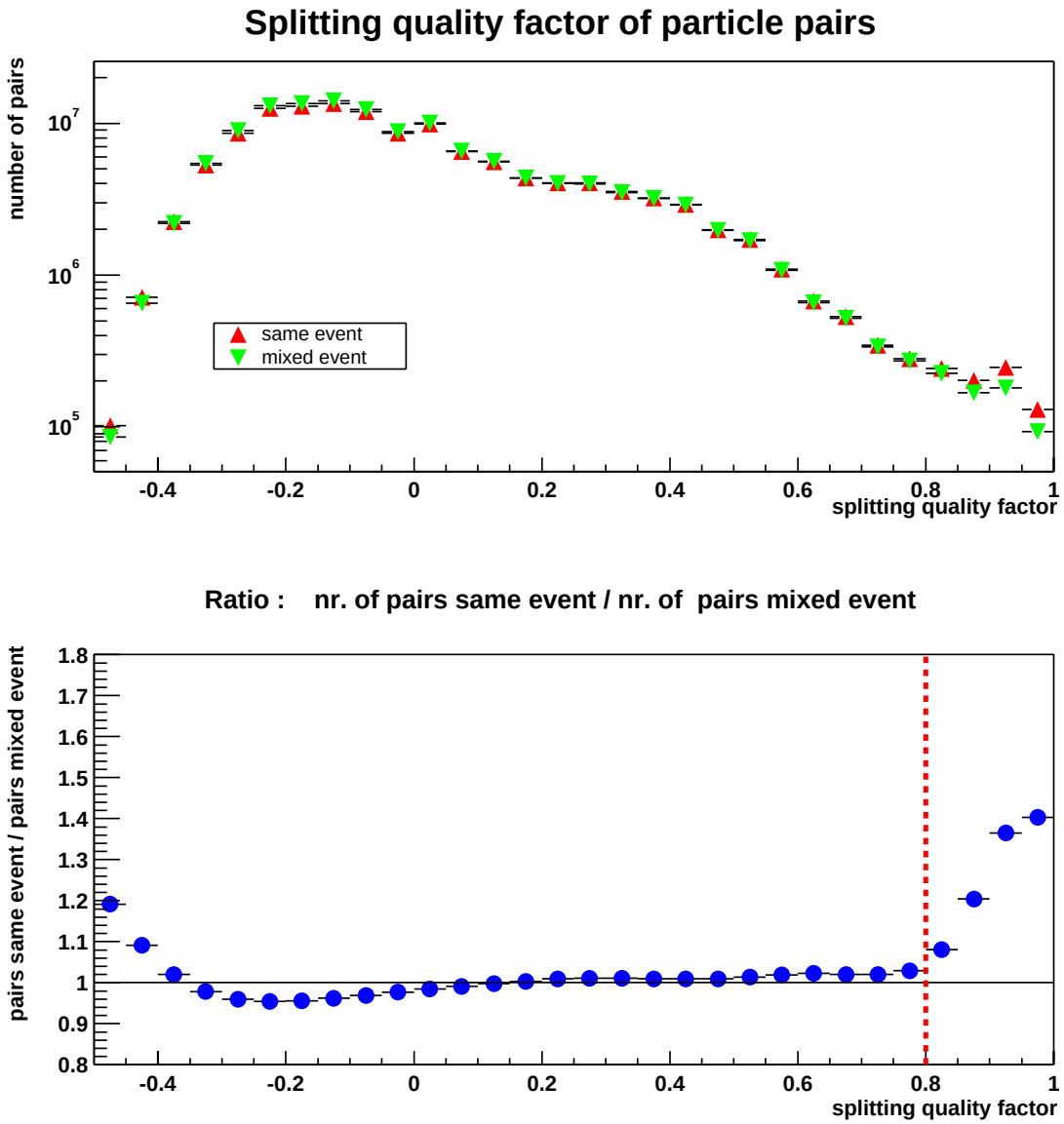

Figure 4.19

a.) upper panel : track splitting quality factor for pairs from the same event and for pairs from mixed events (the mixed event distribution is scaled down).

b.) lower panel: ratio of track splitting quality distributions. The red line indicates the cut value.

Tracks of background pairs do not point to exactly the same point due to varying z position of the main vertex. Besides other effects, like e.g. the HBT correlations, this causes the deviation of the quality factor ratio from unity for values below zero.

4.5 Construction of the correlation function

After event−, track− and pair−cuts we end up with more than $2*10^{10}$ pairs in the signal distribution. Since the statistical error of the correlation function should be dominated by the number of pairs in the signal, we combine every track with all tracks from five different events. These are required to have a z−vertex position in the vicinity of the original z−vertex. Otherwise we would mix events with a different acceptance which alters the shape of the background distribution.

This yields a total of more than $2*10^{11}$ pairs for the background distribution. Because of the large number of pairs we calculate the correlation function not in a single process. The event sample is subdivided into subsamples of roughly 10^4 events, which are handeled by one process. Each of them calculates a signal− and background distribution in the LCMS frame. Afterwards the three dimensional arrays holding these distributions, are added up. The ratio of the total signal distribution over the total background distribution yields the three dimensional correlation function.

Each axis of the three dimensional histogram ranges from 0.0 GeV/c to 0.2 GeV/c. They are subdivided into 20 bins yielding a bin size of 0.01 GeV/c. Choosing larger or smaller bin size, e.g. 0.012 GeV/c or 0.008 GeV/c, has no significant impact on the extracted radii.

5. Experimental results

5.1 One dimensional correlation functions

Figure 5.1 shows the signal and background distribution of q_{inv}, the Lorentz invariant four momentum difference between two particles. Only events, tracks and pairs satisfying the criteria discussed in chapter 4 are accepted. We observe that the overall shape of the signal distribution is well reproduced by the mixed event background over a wide range of relative momentum. Although the number of pairs decreases rapidly with decreasing momentum difference, the enhancement of pairs in the signal distribution due to the Bose−Einstein correlation at small relative momentum is clearly visible.

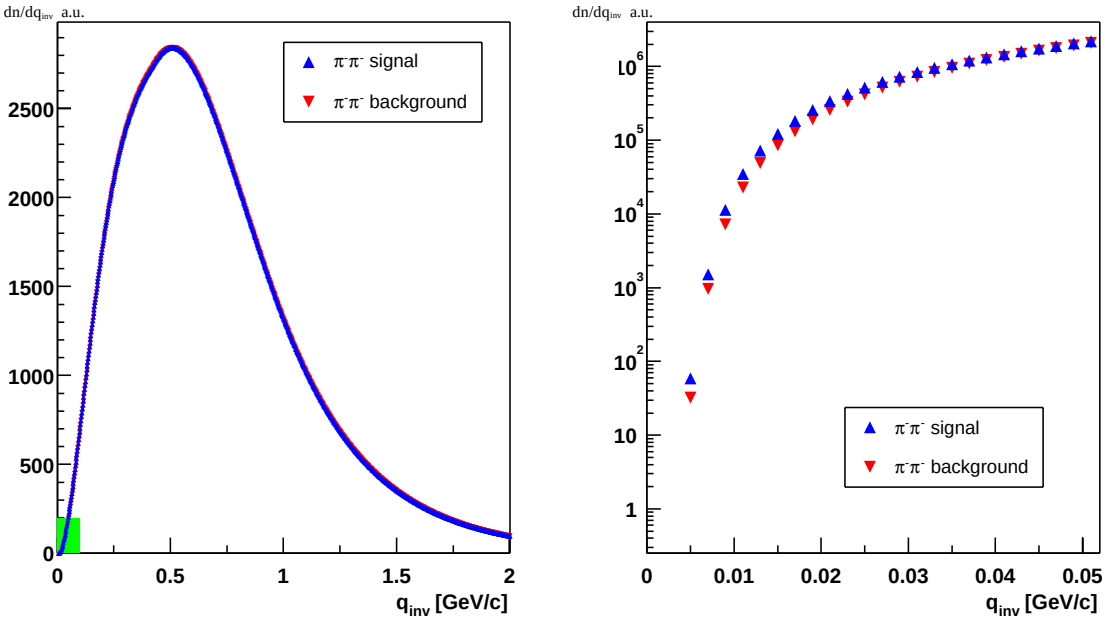

Figure 5.1

lhs : signal and background q_{inv} distribution for $\pi^-\pi^-$ pairs up to 2 GeV/c,

rhs : Bose−Einstein enhancement at low relative momenta

(enlarged green area on lhs).

Ratios of the signal over the normalized background distributions are shown in figure 5.2. The fact, that we observe a strong correlation in the $\pi^+\pi^-$ ratio supports the need to correct the like sign distributions for coulomb repulsion. The influence of the coulomb correction on the correlation function of $\pi^-\pi^-$ pairs is demonstrated in figure

5.2.a. The coulomb correction is done by assuming a 5 fm source and weighting background pairs according to the function introduced in chapter 2.11.

We do not observe any significant deviations between $\pi^+\pi^+$ and $\pi^-\pi^-$ correlation functions as demonstrated in figure 5.2.b.

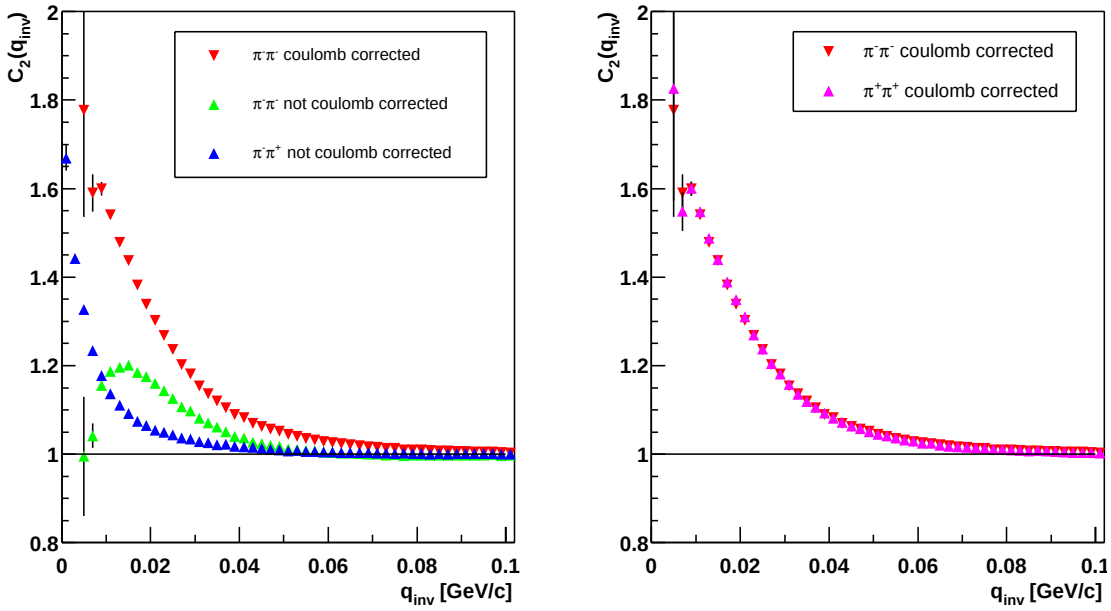

Figure 5.2

lhs : a.) q_{inv} correlation function for $\pi^+\pi^-$ pairs and for $\pi^-\pi^-$ pairs with and without coulomb correction,

rhs : b.) q_{inv} correlation function for $\pi^+\pi^+$ and for $\pi^-\pi^-$ pairs.

In figures 5.1 and 5.2, q_{inv} correlation functions from all $k_t - Y_{\pi\pi}$ bins are added up. In appendix A we show the correlation functions for $\pi^+\pi^+$ and $\pi^-\pi^-$ in individual $k_t - Y_{\pi\pi}$ bins. Since we do not draw any quantitative conclusion from the q_{inv} correlation functions, we do not discuss them further.

5.2 Fitting three dimensional correlation functions

The five parameter function 2.31 respectively 2.34 has to be fitted to the three dimensional correlation function in order to obtain the HBT radii. To reduce fluctuations of the correlation function due to limited statistics we accept only bins in q_{out}, q_{side} and q_{long} (respectively q_{perp}, q_{para} and q_0) which have at least 50 entries in the signal distribution. Since we assume only uncorrelated statistical errors, the χ^2 function is defined as

$$\chi^2(P)=\sum\left(\frac{\frac{s}{b}-t(P)}{e}\right)^2 \qquad 5.1$$

with

s: number of entries in the signal distribution

b: normalized number of entries in the background distribution

t: calculated value at the bin center assuming a parameter set P

e: statistical error

where the statistical error is given by

$$e=\frac{s}{b}\sqrt{\frac{1}{s}+\frac{1}{b}} \qquad 5.2$$

Minimizing this functions using the MINUIT [Min94] software package yields the set of parameters by which the measured data are described best. The error given with each fit parameter indicates the range in which the parameter is likely to be found at a confidence level of 95%. All free fit parameters are considered simultaneously for the error calculation, that means all parameters are in their error range at a given confidence level at the same time.

The background can be normalized by the ratio of the total number of pairs in the signal to the total number in the background distribution. Another approach is to introduce the normalization in the three dimensional fit procedure as an additional sixth free fit parameter. Figure 5.3 demonstrates, that the way of normalizing the background has little impact on the fitting results.

To test the stability of the fit procedure the range of accepted bins was varied. In figure 5.3 the fitting results in the central $Y_{\pi\pi}$ bin are shown using different normalization methods as well as various fitting ranges. A certain fitting range in the PB parametrization means, that all bins satisfying $\sqrt{q_{out}^2+q_{side}^2+q_{long}^2}<\text{fitting range}$ are used for the χ^2 determination.

The change of fit parameters is partly due to the systematical error. It might indicate a deviation of the correlation function from a simple Gaussian distribution. For reasonable cut values and fitting ranges the differences of the absolute values of the

fitting parameters are in the order of 0.5 fm. The k_t dependence and ratios of the radii are more stable than the absolute values of the fit parameters.

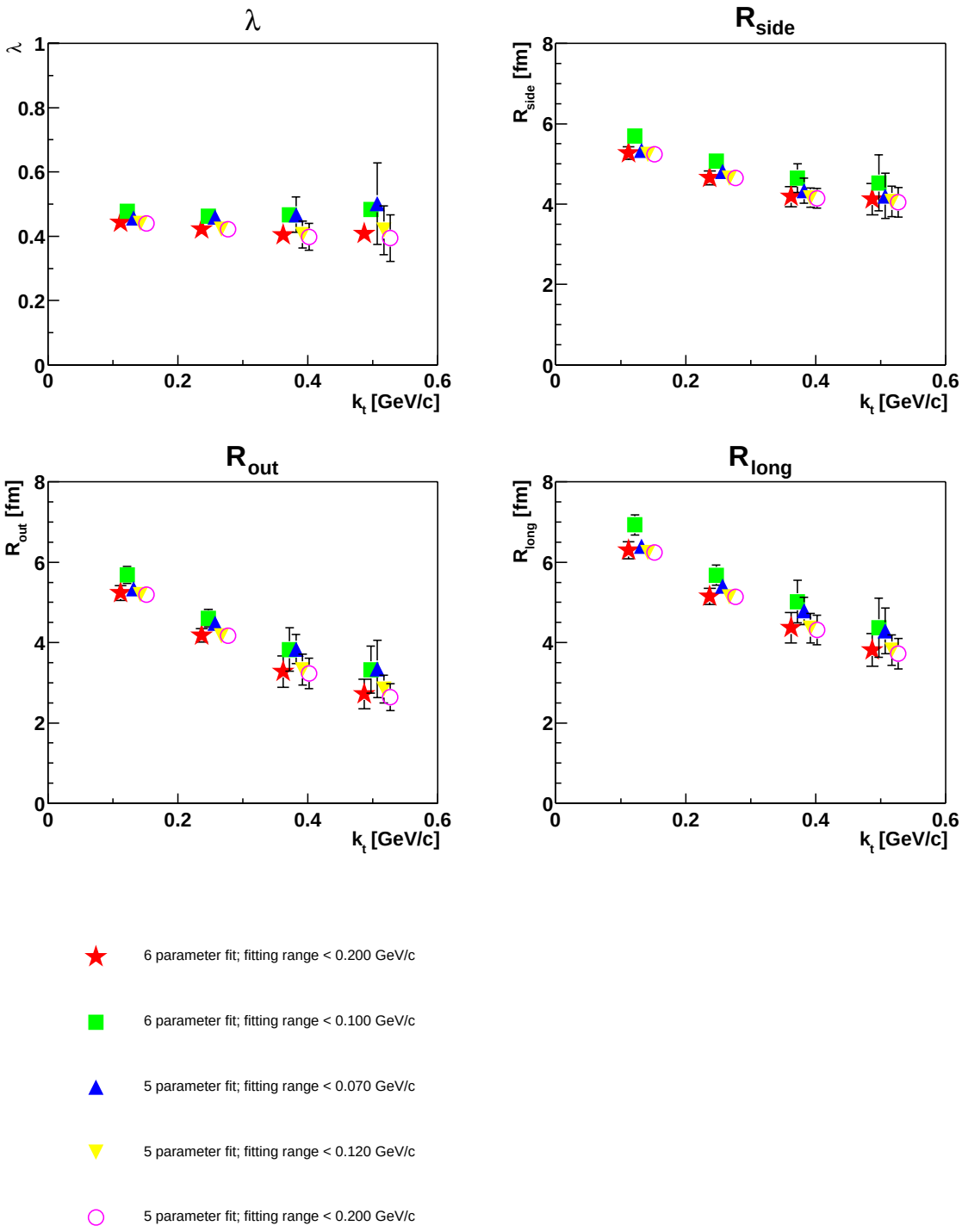

Figure 5.3

k_t dependence of PB fit parameters of $\pi^-\pi^-$ correlation function in the central $Y_{\pi\pi}$ bin for various fit parameters. The symbols are not plotted at exact k_t coordinates to ease the comparison.

Usually the quality of a χ^2 fit is estimated by the ratio of the value of the χ^2 function at its minimum to the number of degrees of freedom (χ^2/DOF). For all fits presented here these ratios are close to unity. This indicates, that the fit functions were reasonable assumptions. It is also instructive, to compare projections of correlation functions to corresponding projections of fit functions. The projection is done by summing over a certain range in the non projected variables, where the bins are weighted by their statistical error. In figure 5.4 we show normalized projections of the PB $\pi^-\pi^-$ correlation function in one $k_t - Y_{\pi\pi}$ bin.

Results presented in the following are determined by using the six parameter fit procedure for the PB as well as for the YKP parametrization. The fitting range in both cases extends to 0.200 GeV/c in all three momentum components.

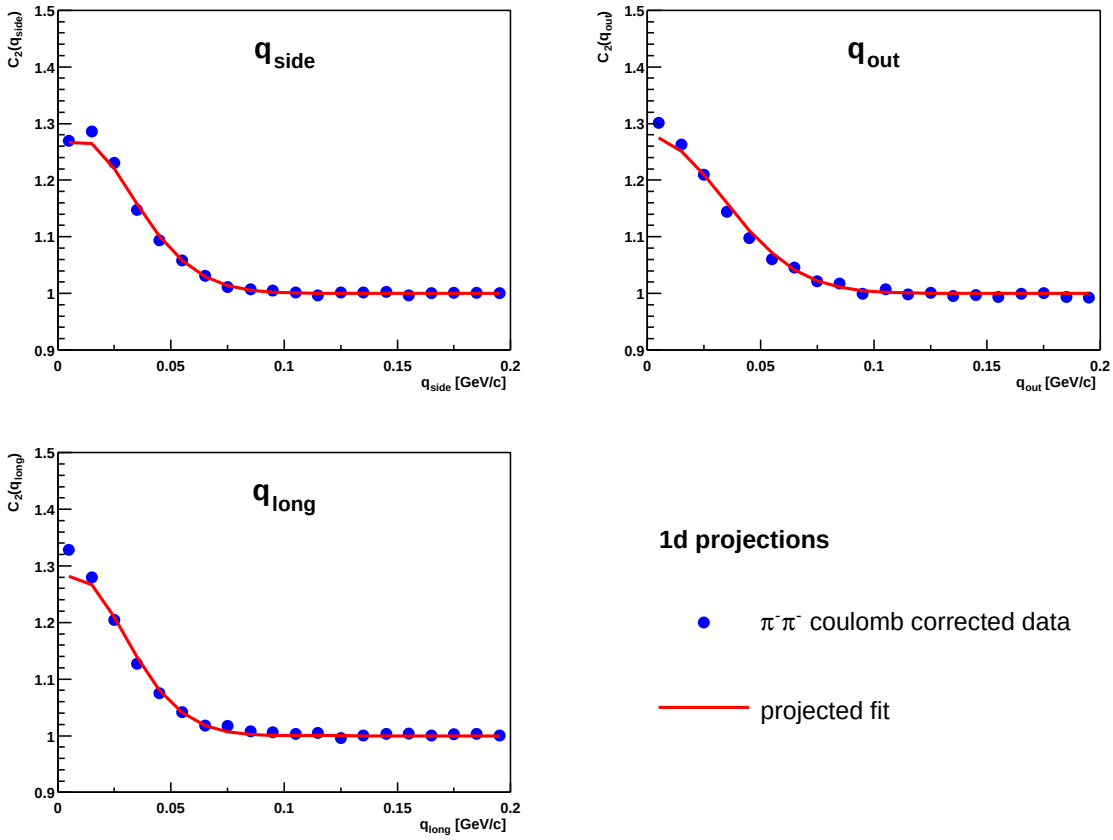

Figure 5.4

Projections of the PB $\pi^-\pi^-$ correlation function and the corresponding projected fit in $k_t - Y_{\pi\pi}$ bin : $0.1 < k_t < 0.2$ *GeV/c* and $-0.2 < Y_{\pi\pi} < 0.2$.

Integration range: 0.0 − 0.030 *GeV/c in each unprojected variable.*

On this scale, statistical errors of data points are smaller than symbols.

5.3 Systematical uncertainties

The systematical error of the measured HBT radii is evaluated by testing the robustness of the correlation function against variations of different analysis parameters. Figure 5.5 shows fit results to $\pi^-\pi^-$ correlation functions in the central $Y_{\pi\pi}$ bin using various pair cuts and assuming different source sizes for the coulomb correction.

Varying the size of the coulomb source causes inevitably different fit parameters. Since the true size is not known, we can only test the impact of reasonable values for the source size on extracted fit parameters. If the correction is based on a smaller source size the mean pair separation is smaller and therefore the correction is stronger. In this case the correlation function becomes broader and hence the radii smaller. On the other hand, if we assume a larger source for the coulomb correction, the radii increase. In figure 5.5 we show fit results for correlation functions with various coulomb corrections, assuming source sizes from 3.0 fm to 7.0 fm. Eventually we chose a source size of 5.0 fm to correct the data, which corresponds roughly to the size of the extracted HBT radii.

Changing pair cuts had no impact on the fit parameters, if the measured correlation functions were exactly described by the fit functions. But limited statistics in combination with little deviations of the measured correlation function to the fit function lead to slight dependences on cut values.

As demonstrated in chapter 4.4.1, the finite two track resolution of the detector makes it necessary to accept only track pairs, that can be resolved by the STAR TPC. Therefore we apply the entrance separation cut. But this selection reduces the number of entries in the signal distribution considerably. If too many pairs are rejected, we loose the whole HBT signal. For this reason it is important to choose the optimal cut value. With respect to the HBT radii we find that a larger cut value means smaller radii, as shown in figure 5.5. For the final analysis we accepted only pairs that have an entrance separation of more than 3.0 cm, which leaves enough entries in the signal distribution and removes all track pairs which cannot be always resolved.

If the reconstruction chain splits a track into two or more pieces, the number of pairs with low momentum difference is artificially increased. Therefore we have to apply the split track cut, which is explained detail in chapter 4.4.2. In figure 5.5 we demonstrate that this cut has little influence on the extracted fit values. In the final analysis we rejected all pairs with a merging quality larger than 0.8.

In summary we find, that changing the analysis parameters alters the correlation function. These changes originate from systematical uncertainties. The fit parameters change up to 10% for reasonable settings of the analysis parameters. In the following presentation of the results we quote only the error from the fit procedure.

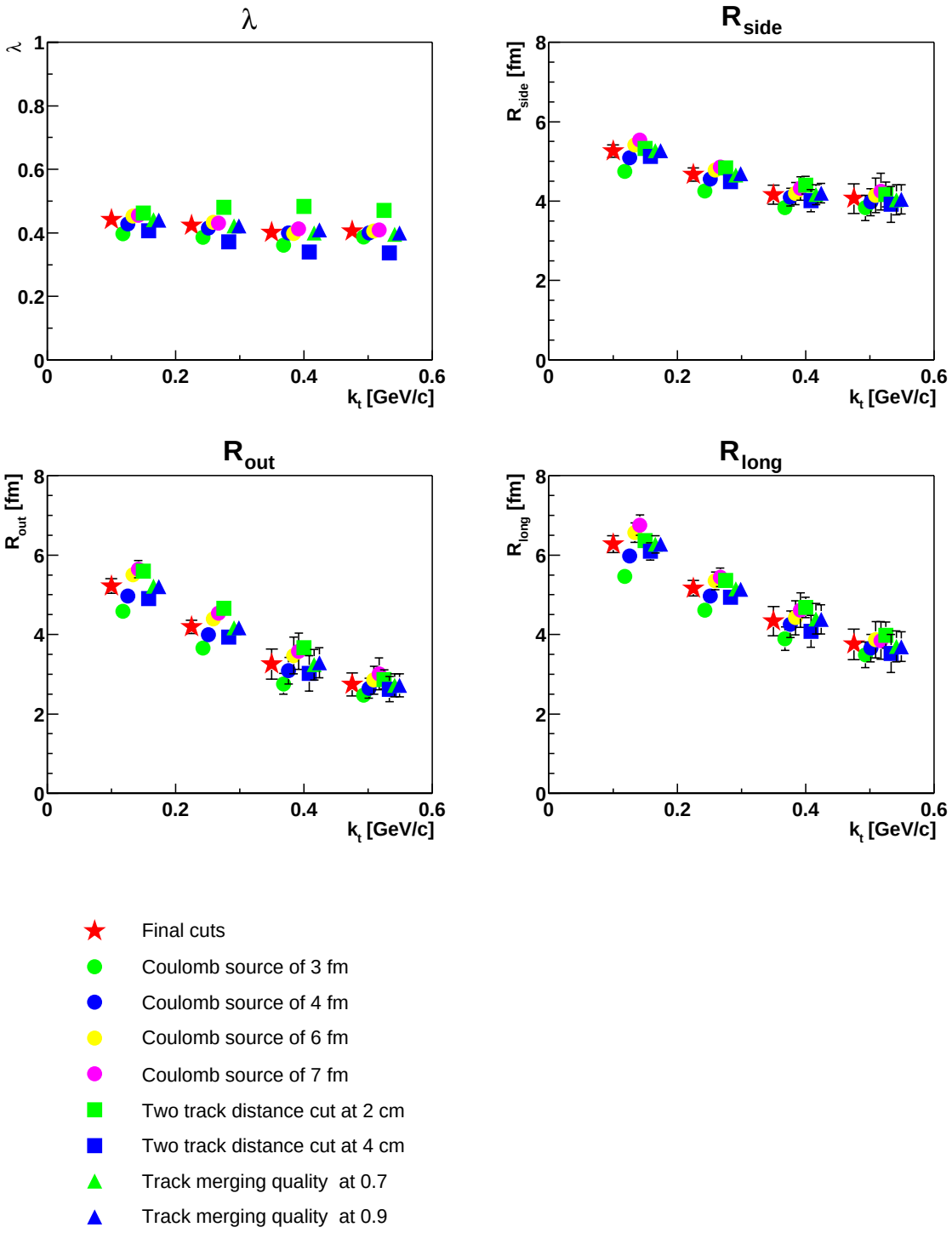

Figure 5.5

Fit parameters for various settings in the analysis chain.

5.4 Momentum resolution correction

In addition to the correction for the coulomb repulsion between pions of the same charge, we have to correct the correlation function for the finite momentum resolution of the detector. Since this correction procedure is very CPU−time consuming we apply it after all other parameters of the analysis procedure are fixed. The finite momentum resolution is corrected for in the following way:

The background pairs are used to construct artificially an "ideal" and a "smeared" correlation function. The former contains no momentum resolution effects the latter does. If the "real" correlation function would be described by the ideal distribution we would measure the smeared one. Therefore, the ratio of these two distributions yields the factor we need to correct the measured correlation function:

$$C_{corrected}(q) = \frac{S_{measured}}{B_{measured}} * \frac{\frac{S_{ideal}}{B_{ideal}}}{\frac{S_{smeared}}{B_{smeared}}} \qquad 5.3$$

here S and B mean respectively signal and background distribution. Below we describe how signal and background of the ideal and smeared correlation functions in the PB parametrization are constructed.

First we have to assume a correlation function

$$C_{model}(q) = 1 + \lambda \exp^{R_{out}^2 q_{out}^2 + R_{side}^2 q_{side}^2 + R_{long}^2 q_{long}^2} \qquad 5.4$$

and reasonable values for the parameters λ, R_{out}, R_{side}, and R_{long}.

For each pair of the the background distribution we calculate the momentum difference $q_{true} = q_{true}(q_{out}, q_{side}, q_{long})$. The three dimensional idealized signal histogram S_{ideal} is then constructed by weighting each entry at q_{true} with the correlation function $C_{model}(q_{true})$.

Since the ideal correlation function should also contain the coulomb effect, we have to weight entries at q_{true} in the background B_{ideal} with the coulomb correction introduced in chapter 2.11.

In order to fill the smeared distributions we have to consider the momentum resolution of the STAR detector. We calculate the momentum of a particle based on the azimuthal angle φ, the polar angle θ and the curvature of the track ($\sim 1/p_t$). Measurement errors of these quantities lead to errors of the momentum components assigned to a track. The main uncertainty in the momentum reconstruction in STAR arises from the determination of the curvature of a track, therefore we neglect errors in φ and θ and consider only the transverse momentum resolution.

The relative momentum resolution of the x component for example, is given by

$$\Delta p_x = p_x * \frac{\Delta p_t}{p_t} \qquad 5.5$$

According to figure 4.6 the relative transverse momentum resolution of the STAR detector is

$$\frac{\Delta p_t}{p_t} \approx 2\% \qquad 5.6$$

To emulate the measurement process we smear the momenta of the background pair, e.g. the x component is smeared by:

$$p_x^{smeared} = p_x^{original} * (1 + g(2\%)) \qquad 5.7$$

with a random value $g(2\%)$ from a gaussian shaped probability distribution centered around zero and with a standard deviation of 2%.

From these values we can calculate the smeared momentum difference $q_{smeared}$. The $S_{smeared}$ distribution is filled by weighting each entry at $q_{smeared}$ with $C(q_{true})$.

Because we correct also the coulomb effect according to the measured momentum difference, we construct the background $B_{smeared}$ by weighting each entry at $q_{smeared}$ with the coulomb weight factor $K(q_{smeared})$.

The impact of the momentum resolution correction on PB radii is demonstrated in figure 5.6. We show the parameters λ, R_{out}, R_{side}, and R_{long} of the $\pi^-\pi^-$ correlation function in the central $Y_{\pi\pi}$ bin with and without momentum resolution correction. R_{side} and R_{long} change very little, but the R_{out} parameter increases up to 8% at high transverse momenta. The finite transverse momentum resolution affects mainly the q_{out} component and therefore we see the largest effect in R_{out}. The relatively large effect on the λ parameter is due to fact, that the finite momentum resolution changes mainly the correlation function at very small momentum differences. Thus the intercept of the correlation function is increased whereas the width of the Bose Einstein enhancement changes less.

For the YKP parametrization we find that R_{perp} and R_{para} change very little, the λ parmeter changes similar to the PB case and R_0 increases up to 5% if it is larger than zero.

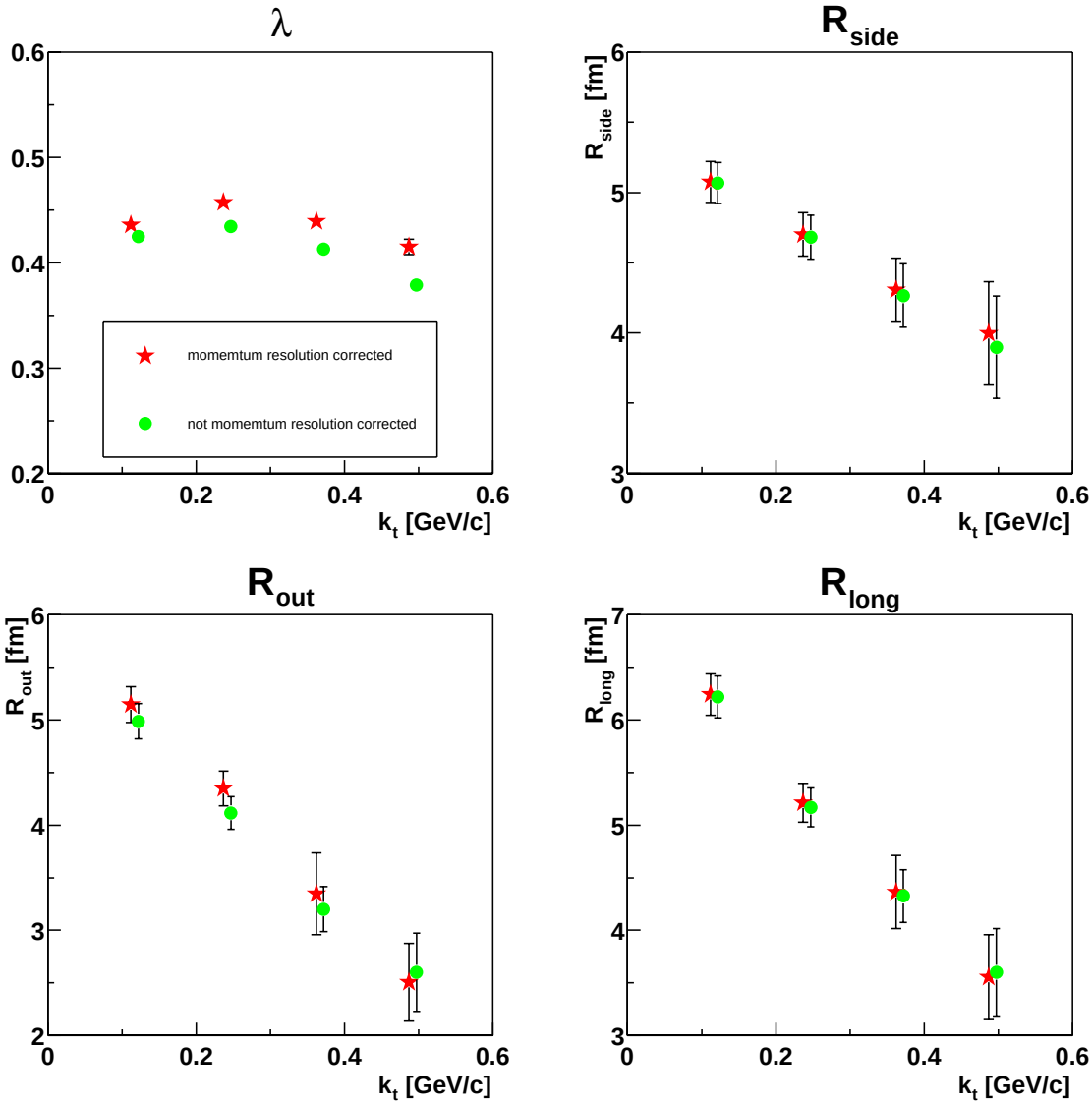

Figure 5.6

$\pi^-\pi^-$ PB fit parameters in the central $Y_{\pi\pi}$ bin with and without momentum resolution correction.

5.5 Results for the YKP parametrization

The three dimensional YKP correlation functions in all $k_t - Y_{\pi\pi}$ bins are constructed for events, tracks and pairs selected according to the criteria discussed in chapter 4. The six parameter function is fitted to each correlation function as described in 5.2. Figure 5.7 shows the dependence of the extracted fit parameters λ, R_{para}, R_{perp}, R_0, and β on pair rapidity $Y_{\pi\pi}$ in four k_t intervals:

$$k_t 1: \quad 0.1 < k_t < 0.2 \quad \text{GeV/c}$$
$$k_t 2: \quad 0.2 < k_t < 0.3 \quad \text{GeV/c}$$
$$k_t 3: \quad 0.3 < k_t < 0.4 \quad \text{GeV/c}$$
$$k_t 4: \quad 0.4 < k_t < 0.5 \quad \text{GeV/c}$$

Since the $k_t - Y_{\pi\pi}$ distribution is not flat (see figure 4.17), we do not use the center of the $Y_{\pi\pi}$ bin as $Y_{\pi\pi}$ coordinate, but the center of gravity in $Y_{\pi\pi}$−direction of the according $k_t - Y_{\pi\pi}$ bin.

The correlation functions are calculated and fitted for $\pi^+\pi^+$ and $\pi^-\pi^-$ pairs separately. Green symbols correspond to $\pi^+\pi^+$ and blue symbols to $\pi^-\pi^-$ results. We do not observe any systematic deviation between the two cases.

None of the fit parameters depends on longitudinal pair rapidity $Y_{\pi\pi}$, they are constant within the observed range.

Since the acceptance of the detector and − we assume − also the pion source itself are symmetric around midrapidity, violations of this symmetry are due to systematic and statistical errors.

We find a λ parameter of ~0.4 which means, that we observe a clearly pronounced Bose Einstein enhancement. The radius R_{para} ranges from ~3.5 fm in the lowest k_t bin to ~6.5 fm in the highest. We see a similar behaviour for R_{perp} with slightly smaller values, a maximum of ~5.1 fm and a minimum of ~3.5 fm.

Except for the first k_t bin the parameter R_0 equals zero. The physical implications of this result will be discussed in chapter 6. At this point we only remark, that a vanishing parameter often interferes with a proper fit. But the PB parametrization shows compatible parameters and there we don't have this complication.

The velocity parameter β is always close to zero. It is trivial, that we find non zero values if the correlation function is not measured in the LCMS frame, but in the rest frame of the source.

Figure 5.8 shows the dependence of the YKP fit parameters on transverse pair momentum k_t. For the same reason as above, the k_t coordinate is not the center of the bin but the center of gravity in k_t−direction of the according $k_t - Y_{\pi\pi}$ bin. The k_t dependence of all five parameters is shown for five rapidity intervals:

$Y_{\pi\pi}1$: $-1.0 < Y_{\pi\pi} < -0.6$

$Y_{\pi\pi}2$: $-0.6 < Y_{\pi\pi} < -0.2$

$Y_{\pi\pi}3$: $-0.2 < Y_{\pi\pi} < 0.2$

$Y_{\pi\pi}4$: $0.2 < Y_{\pi\pi} < 0.6$

$Y_{\pi\pi}5$: $0.6 < Y_{\pi\pi} < 1.0$

Blue symbols correspond to $\pi^-\pi^-$ and green to $\pi^+\pi^+$ correlation functions. We observe a decrease of λ, R_{para} and R_{perp} with increasing k_t in all rapidity bins, while the decrease for R_{para} is strongest. Values for the fit parameters are tabulated in appendix B. The meaning of these results with respect to the source function will be discussed in chapter 6.

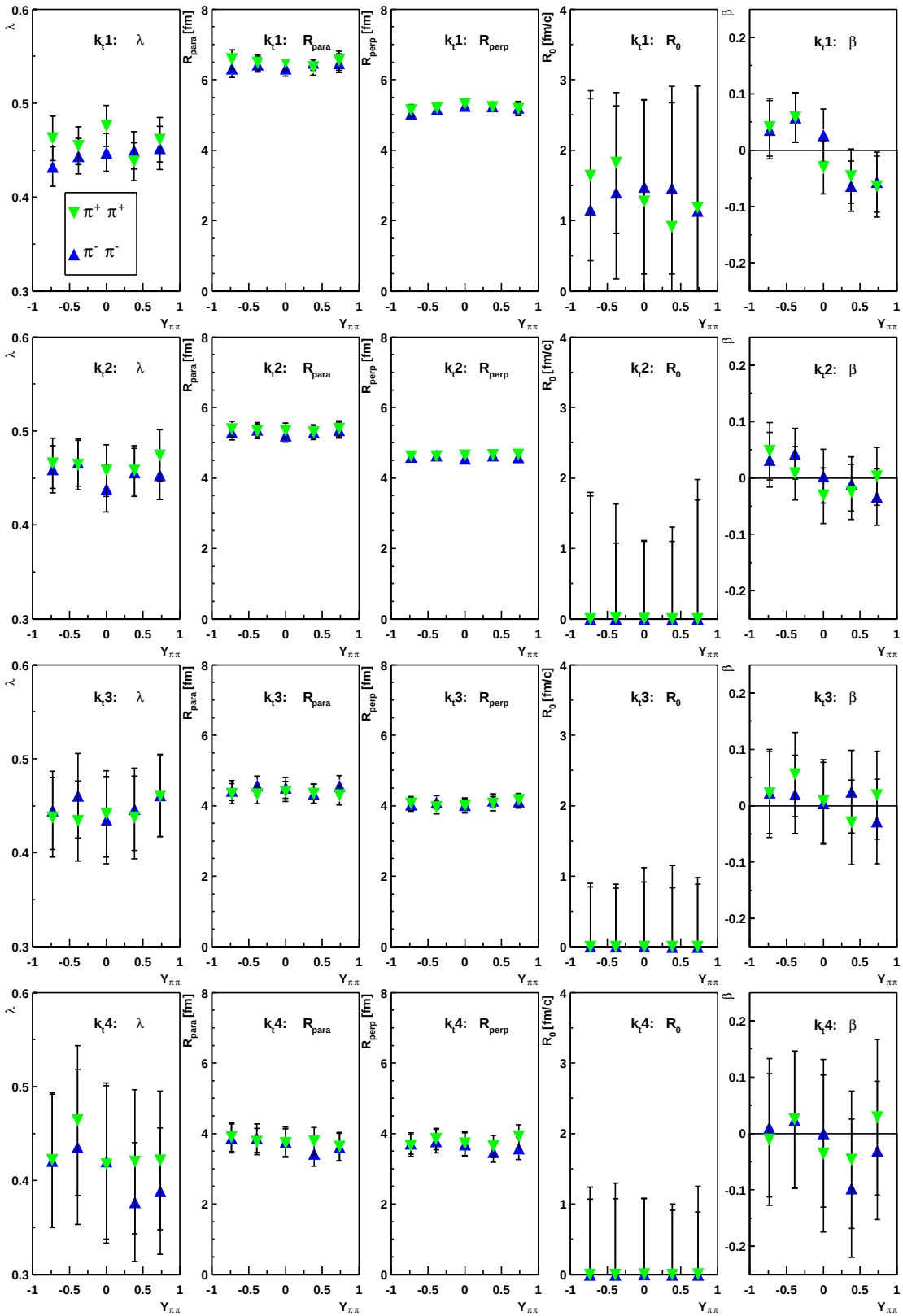

Figure 5.7

Dependence of YKP fit parameters on $Y_{\pi\pi}$.

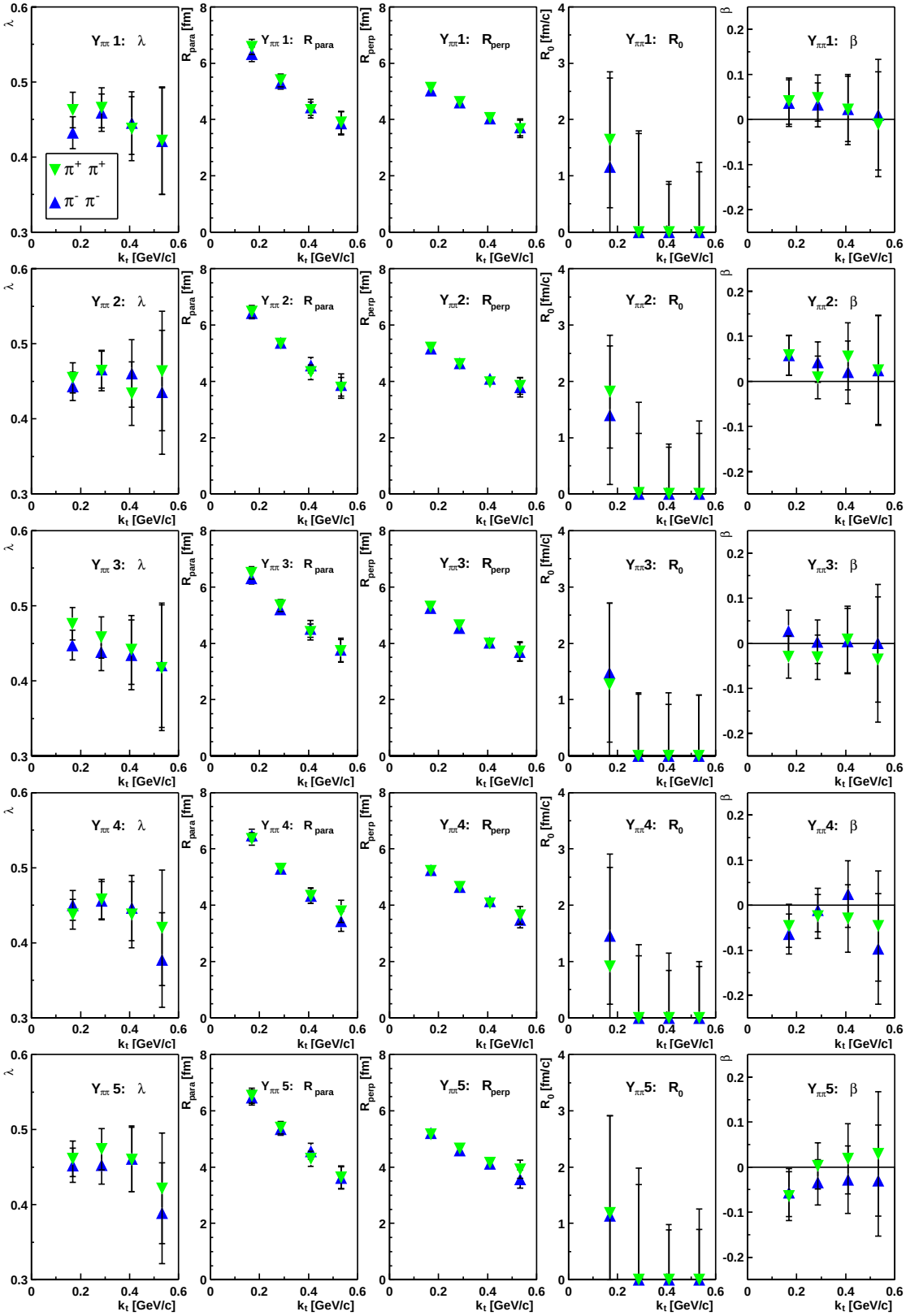

Figure 5.8

Dependence of YKP fit parameters on k_t.

5.6 Results for the PB parametrization

The PB fit parameters are obtained using the same analysis settings as used for the YKP parametrization. In figure 5.9 the dependence of λ, R_{side}, R_{out}, R_{long}, and $R_{outlong}$ on longitudinal pair rapidity $Y_{\pi\pi}$ is plotted in four bins of transverse momentum k_t

$$k_t 1: \quad 0.1 < k_t < 0.2 \quad \text{GeV/c}$$
$$k_t 2: \quad 0.2 < k_t < 0.3 \quad \text{GeV/c}$$
$$k_t 3: \quad 0.3 < k_t < 0.4 \quad \text{GeV/c}$$
$$k_t 4: \quad 0.4 < k_t < 0.5 \quad \text{GeV/c}$$

As above, the k_t coordinate corresponds to the center of gravity in the corresponding $k_t - Y_{\pi\pi}$ bin. Fit parameters for $\pi^+\pi^+$ correlation functions are represented by green and for $\pi^-\pi^-$ correlations by blue symbols. No systematic differences between these two are observed. The five HBT fit parameters are constant over all $Y_{\pi\pi}$ bins. The fit procedure yields values between ~0.35 and ~0.45 for the λ parameter and the radii R_{side}, R_{out} and R_{long} range from ~3.0 to 6.5 fm. The cross term $R_{outlong}$ equals zero in nearly all bins.

Figure 5.10 shows the dependence of the fit parameters on k_t in the five bins of longitudinal pair rapidity $Y_{\pi\pi}$.

$$Y_{\pi\pi} 1: \quad -1.0 < Y_{\pi\pi} < -0.6$$
$$Y_{\pi\pi} 2: \quad -0.6 < Y_{\pi\pi} < -0.2$$
$$Y_{\pi\pi} 3: \quad -0.2 < Y_{\pi\pi} < 0.2$$
$$Y_{\pi\pi} 4: \quad 0.2 < Y_{\pi\pi} < 0.6$$
$$Y_{\pi\pi} 5: \quad 0.6 < Y_{\pi\pi} < 1.0$$

The λ parameter and all three radius parameters R_{side}, R_{out} and R_{long} decrease with increasing k_t. R_{long} drops from ~6.5 fm to ~4.0 fm, R_{out} from ~5.5 fm to 3.0 fm and R_{side} from ~5.5 fm to 4.0 fm. For higher transverse momenta the ratio of R_{out} over R_{side} drops below unity, this behaviour corresponds to the vanishing R_0 parameter in the YKP parametrization. The meaning of these results will be discussed in chapter 6. All fit parameters are tabulated in appendix B.

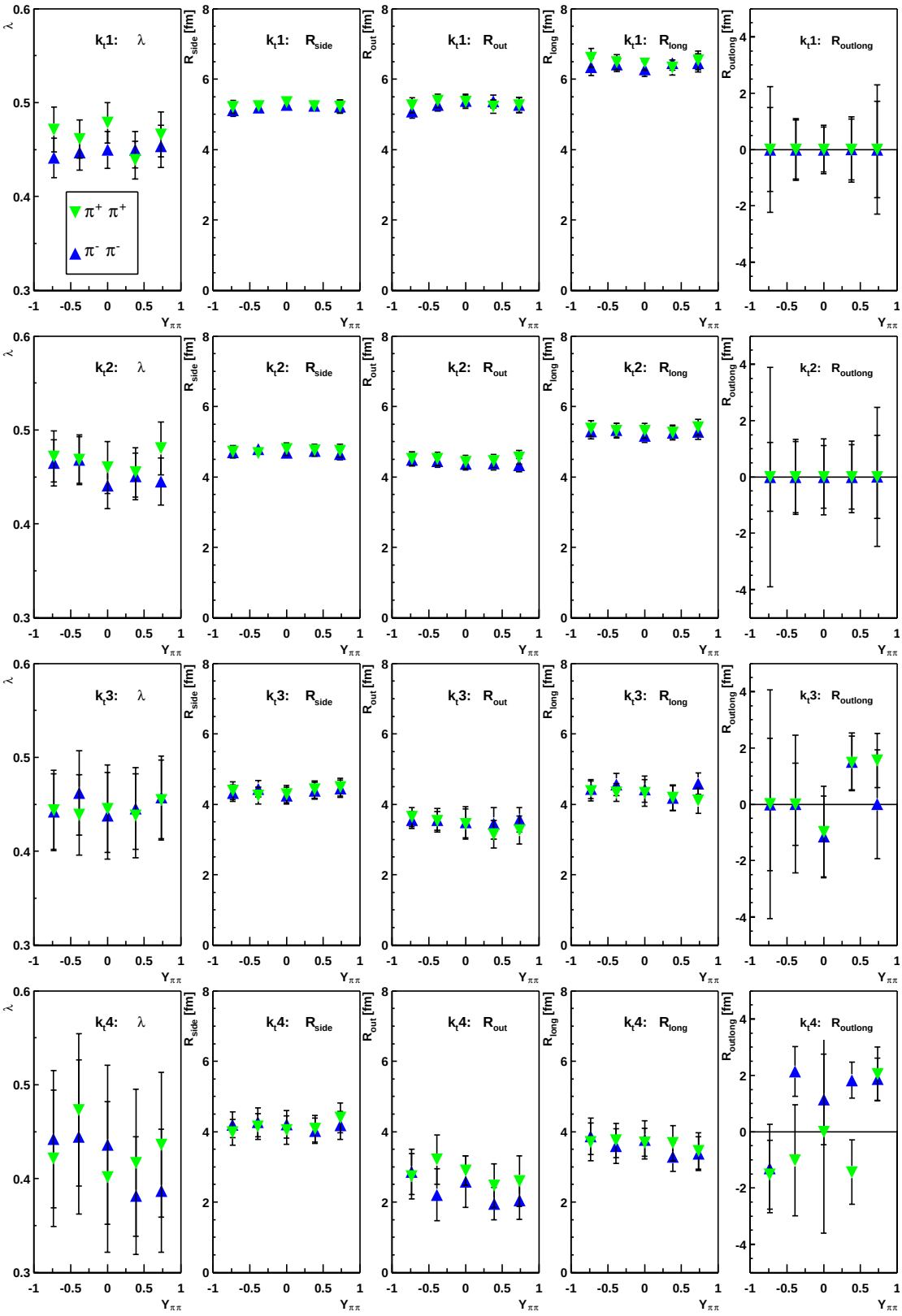

Figure 5.9

Dependence of PB fit parameters on $Y_{\pi\pi}$.

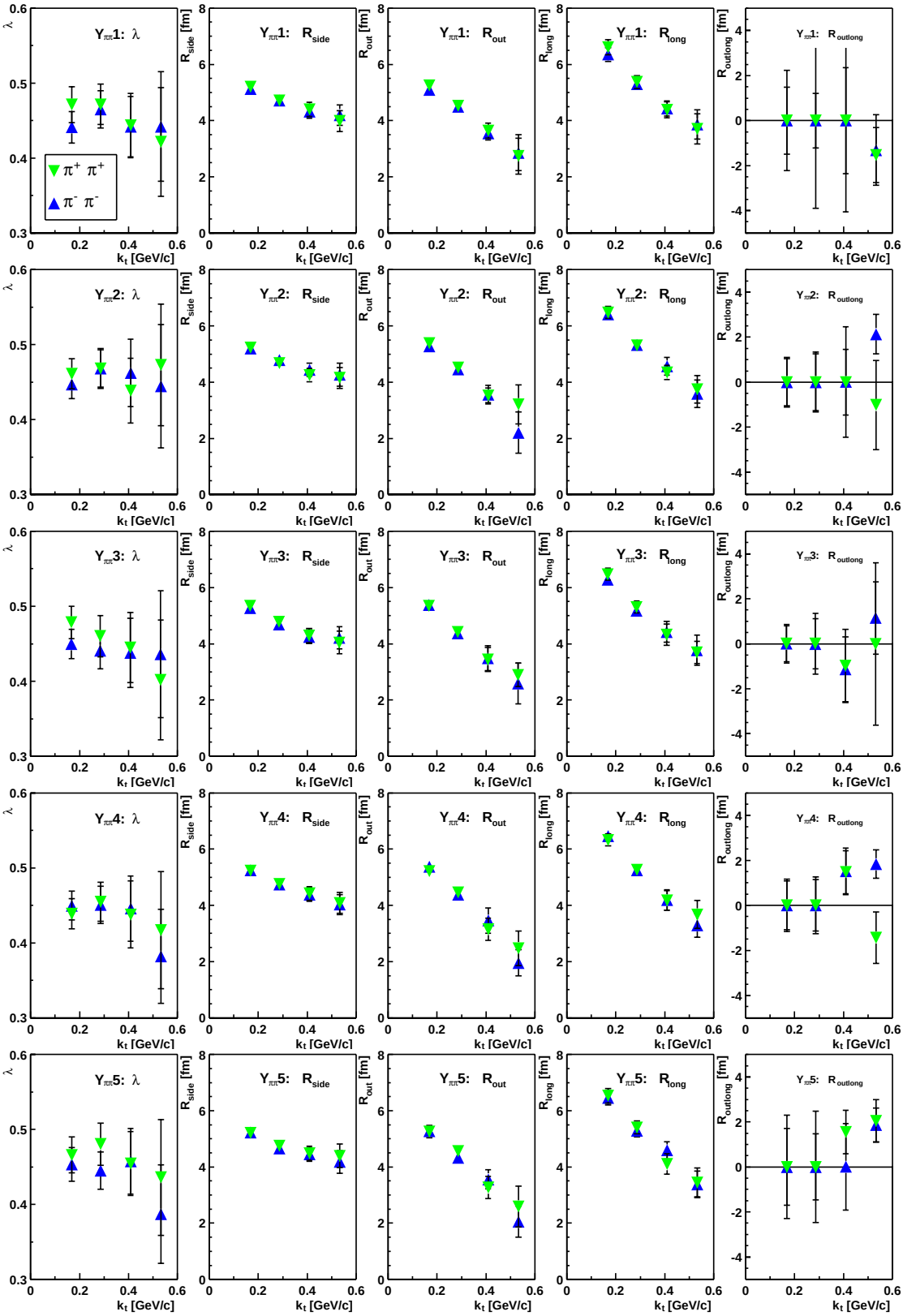

Figure 5.10

Dependence of PB fit parameters on k_t .

5.7 Consistency of PB and YKP parametrization

YKP parameters can be compared under certain assumptions to PB parameters. As described in chapter 2.9 this comparison serves as a consistency check since both parametrizations are applied to correlation functions from the same source.

In figure 5.11 we show the fit results of $\pi^-\pi^-$ correlation functions in the central $Y_{\pi\pi}$ bin in both parametrizations. The fit parameters for λ, for the transverse radii R_{side} and R_{perp}, as well as for the longitudinal radii R_{long} and R_{para} show compatible values as expected from equation 2.42. Comparing the remaining radii is not very meaningful, because the parameter R_0 vanishes and the ratio of R_{out} to R_{side} drops below unity.

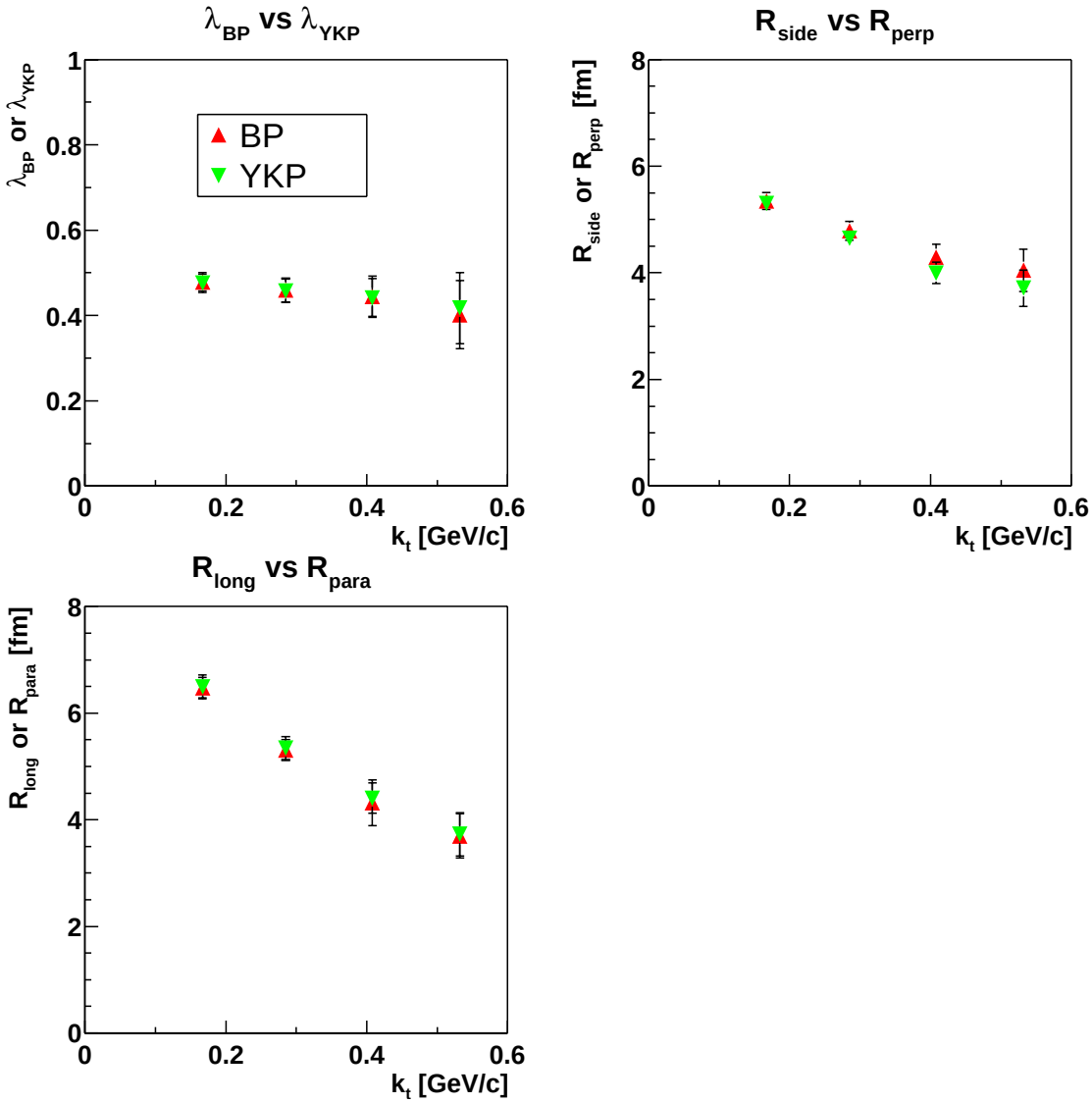

Figure 5.11

YKP and PB fit parameters in the central $Y_{\pi\pi}$ bin.

6. Discussion

6.1 Dependencies of HBT parameters on $Y_{\pi\pi}$

The measured HBT radii do not depend on longitudinal pair rapidity $Y_{\pi\pi}$ as shown in figures 5.7 and 5.9. In figure 6.1 we directly compare the k_t dependence of the PB radii in all five $Y_{\pi\pi}$ bins and find only small differences.

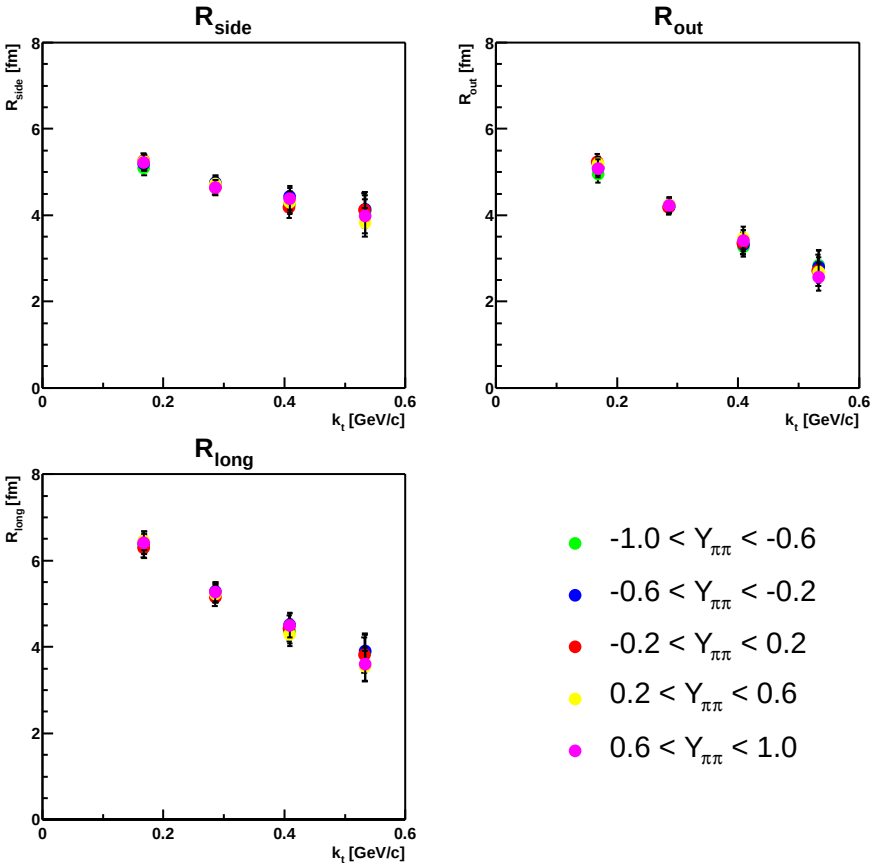

Figure 6.1

Dependence of PB HBT radii on k_t in different $Y_{\pi\pi}$ bins.

The STAR TPC records only particles in a relatively small window around midrapidity. Measurements presented here cover only two units of rapidity, whereas the gap between the two projectile nucleons reaches nearly ten units of rapidity. In the measured momentum region the single particle rapidity distribution is flat [Adl01b], i.e. we do not see the finite extension of the source in longitudinal direction.

Therefore we can expect to find uniform longitudinal 'slices' of the source. The subdivision of the sample into intervals of pair rapidity corresponds to a set of such slices around midrapidity [Won94]. The fact that the correlation function and hence the radii are very similar in all examined rapidity bins, reflects the uniformity of the source function around midrapidity.

An important information about the longitudinal behaviour of the source function is given by the parameter β of the YKP parametrization. According to figure 5.7, β is close to zero in all k_t–$Y_{\pi\pi}$ bins. In figure 6.2 we show a different representation of this parameter, namely the dependence of the Y_{YKP} rapidity

$$Y_{YKP} = \frac{1}{2} \ln \frac{1+\beta}{1-\beta} + Y_{\pi\pi} \qquad 6.1$$

on pair rapidity $Y_{\pi\pi}$ for four k_t intervals. It can be shown, that the longitudinal velocity of a source element follows closely Y_{YKP} [Wu98]. The dependence of Y_{YKP} on $Y_{\pi\pi}$ is therefore determined by the longitudinal expansion. A linear relation corresponds to a strong longitudinal or even a boost invariant expansion, whereas for static sources Y_{YKP} would be constant.

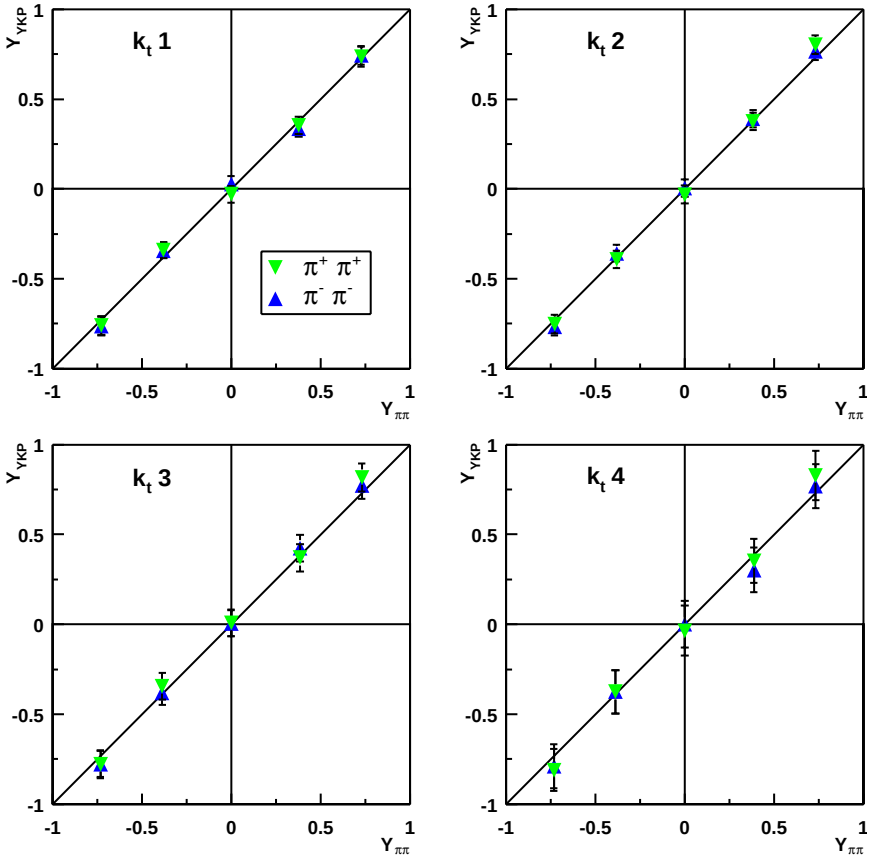

Figure 6.2

Dependence of Y_{YKP} on $Y_{\pi\pi}$.

k_t–intervals are the same as in figure 5.7.

In our measurements the parameter β vanishes in the LCMS system, and with it the first term in equation 6.1. Hence Y_{YKP} is proportional to $Y_{\pi\pi}$ indicating a strong longitudinal expansion. The same method also showed strong longitudinal expansion at lower energies, e.g. [App98].

The crossterm $R_{outlong}$ in the PB parametrization vanishes if longitudinal boost invariance is assumed, but also for symmetric collisions at midrapidity [Hei99a]. In this analysis we find it to be close to zero in all momentum regions. Since we are studying a symmetric system the crossterm vanishes as expected. No further conclusions can be drawn from this observable.

6.2 Life time of the source

The life time τ of the source is defined as the time from the initial overlap of the projectile nuclei until the kinematic freeze out. Makhlin and Sinyukov [Mak88] found a simple relation between the m_t dependence of R_{long} and the lifetime τ of a longitudinally boost invariant source at temperature T:

$$R_{long}(m_t) \approx \tau \sqrt{\frac{T}{m_t}} \qquad 6.2$$

In general, HBT parameters measure only regions of homogeneity and therefore relations to source parameters like temperature and life time are not self−evident. One has to consider that any space−momentum correlation, like collective flow, alters the two particle correlation function. Provided the space−momentum correlations depend on m_t, the HBT parameters will also change with transverse pair momentum. In this case the dependence of the measured radii on m_t may allow to quantify the underlying space−momentum correlation.

To find relation 6.2 it is necessary to choose a Bjorken profile [Bjo83] for the longitudinal flow for which the longitudinal velocity gradient is related to the total proper time τ [Hei99]. The second term T/m_t accounts for the thermal smearing which weakens the strict space−momentum correlation introduced by the velocity field.

In figure 6.3 we show for the $\pi^-\pi^-$ correlation function the dependence of the parameter R_{long} on transverse mass m_t and a fit of relation 6.2. We find at freeze out a temperature of ~120 MeV and a life time of ~8 fm.

These values are close to measurements at lower energies at the SPS, e.g. [App98]. It is not evident, why the correlation functions at different energies look so similar, considering the fact that the initial conditions at RHIC and at the SPS are significantly different [Bro02].

Corrections to equation 6.2 were given in [Her95] or [Cha95] indicating that the relation between length of homogeneity and life time of the source is sensitive to the specific model used to describe the evolution of the collision.

Recent calculation reproduce the $1/m_t$ dependence, while extracted values for R_{long} are systematically larger than the measured ones [Hir02][Sof01][Sof02][Lin02]. Various explanations for this discrepancy are presently discussed, e.g.:

- If the system is not in perfect thermal equilibrium after chemical freeze out, temperature and velocity fields fluctuate and single particle spectra as well as two particle correlation functions must be interpreted in a different way [Dum02].
- Ideal hydrodynamics used to describe the collective effects might not be appropriate, a correction due to the viscosity of nuclear matter reduces the R_{long} parameter considerably [Tea02].
- Thermal freeze out happens very early close to the chemical freeze out [Hei02a].
- The longitudinal expansion of the source might be significantly stronger than the boost invariant Bjorken expansion [Hei02].
- Early chemical freeze out reduces the life time of the source and thus gives smaller values for the parameter R_{long} [Hir02].

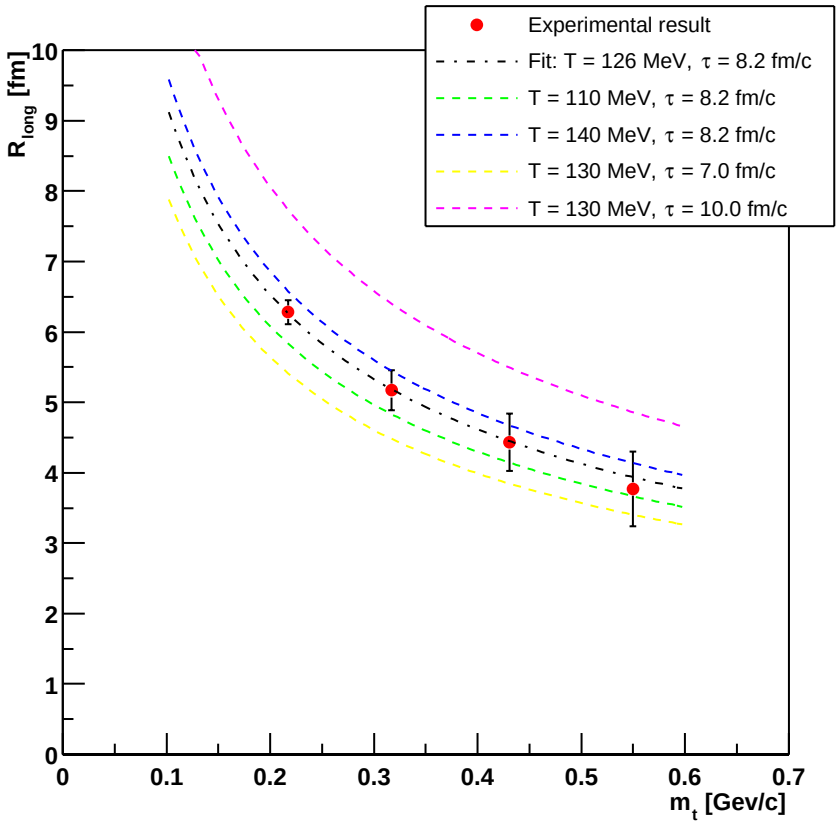

Figure 6.3

m_t dependence of the parameter R_{long} for the $\pi^-\pi^-$ correlation function in the central rapidity bin and fit according to equation 6.2.

6.3 Transverse expansion

Just as longitudinal expansion affects R_{long}, transverse flow causes an m_t dependence of the parameter R_{side}. To derive the quantitative relation, one has to consider again a specific source function. Using the emission function 2.43 introduced in chapter 2.10, R_{side} is related to the strength of the transverse expansion η_f and the geometric radius R_G by [Cha95][Sch99][Csö96]

$$R_{side}(m_t) \approx \frac{R_G}{\sqrt{1+\frac{\eta_f^2}{T} m_t}} \qquad 6.3$$

In case of R_{side} the transverse collective flow is the space−momentum correlation that tends to reduce the length of homogeneity. The thermal smearing on the other hand enlarges the region of homogeneity. It is represented in equation 6.3 by the factor m_t/T.

Transverse flow must be built during the collision, while longitudinal flow is already given at the beginning due to the incomplete stopping of the two nuclei. Therefore the effects from transverse flow are generally weaker than from longitudinal flow and equation 6.3 is different from the corresponding relation 6.2 in the longitudinal case. In simulations the HBT radius R_{side} at low m_t equals nearly the geometric size R_G of the source [Hei99]. Consequently, R_{side} equals R_G for vanishing transverse mass in equation 6.3.

In figure 6.4 we show the measured dependence of R_{side} on m_t in the central rapidity bin for $\pi^-\pi^-$ pairs and a fit according to equation 6.3. To put the geometric radius of $R_G \approx 7.4\,\mathrm{fm}$ into perspective, we relate the two−dimensional rms width of the collision region $R_{RMS}^{source} = \sqrt{2}\,R_G \approx 10\,\mathrm{fm}$, to the two−dimensional rms widths of a cold gold nucleus R_{hs}^{Au}. The hard sphere radius of gold $R_{hs} \approx 7\,\mathrm{fm}$ yields a two−dimensional transverse rms width of $R_{hs}^{Au} = \sqrt{3/5}\,R_{hs} \approx 5.4\,\mathrm{fm}$. This means the initial volume of the overlapping nuclei increases roughly by a factor of two until freeze out [Tom02].

Compared to measurements at SPS ($R_G \approx 6.5\,\mathrm{fm}$)[Ada02][App98] we find a somewhat higher value for R_G, which could be caused by stronger transverse expansion or a longer life time of the source.

The strength of the transverse expansion over temperature $\eta_f^2/T \approx 4.5$ is only slightly higher than at SPS ($\eta_f^2/T \approx 4.0$)[Ada02][App98]. One would expect, that the transverse expansion velocity increases with initial energy density, and hence larger values for η_f^2/T at higher beam energies. In order to derive a mean transverse velocity $\nabla_\perp$ from the paramater η_f^2/T an additional information is needed to resolve

the ambiguity between temperature T and collective expansion strength η_f^2. An elegant solution is to consider single particle m_t spectra and the dependence of R_{side} on m_t simultaneously.

When discussing single particle spectra one faces also the problem, how to disentangle transverse expansion from temperature [Sch94][Xu01]. Using both measurements simultaneously, means to establish an additional condition, which further constraints the set possible values for transverse expansion and temperature. This procedure was successfully applied to data at SPS [Ada02] and the mean transverse velocity was found to be $\nabla_\perp \approx 0.3-0.5$. Prelimary calculations with STAR data using a similar method yield a mean transverse velocity of $\nabla_{infinite} \approx 0.6$ [Cer02].

The decrease of the radius R_{side} with increasing transverse momentum m_t is reproduced by most calculations, e.g. [Zsc02][Sof01]. But the absolute size of R_{side} derived from models is lower than the experimentally measured values and the dependence is usually weaker in simulations than in reality.

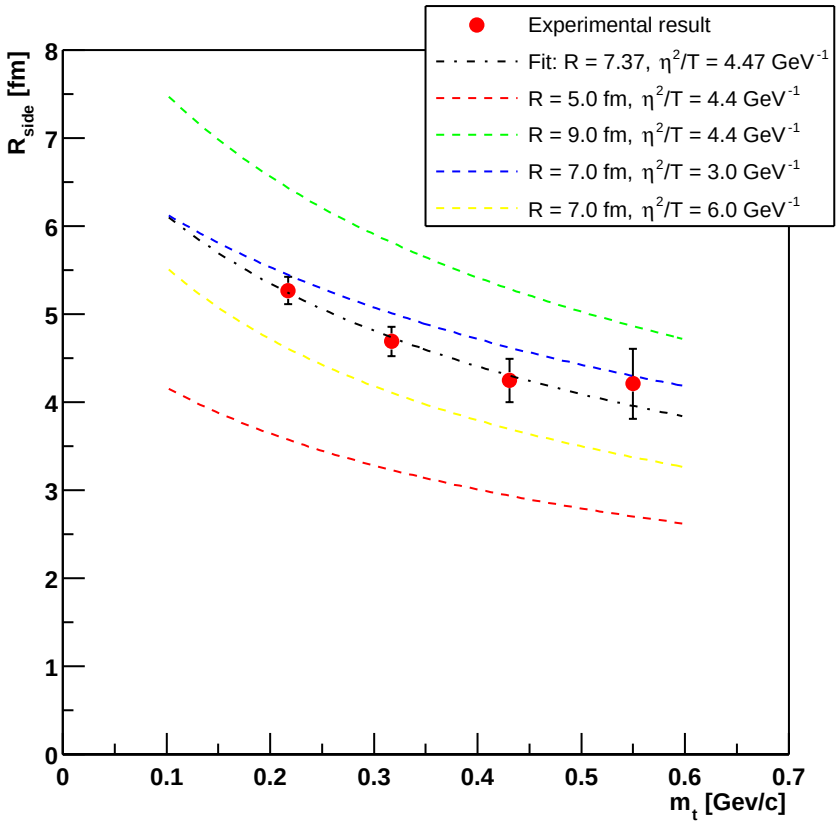

Figure 6.4

m_t dependence of R_{side} for the $\pi^-\pi^-$ correlation function in the central rapidity bin and fit according to equation 6.3.

Just as for the parameter R_{long}, it is not clear to which degree approximation 6.3 is valid. Closer examination of the assumptions that yield the simple relation 6.3 might help to eliminate the discrepancies between experiment and theory. But the weak dependence of extracted HBT parameters on initial energy density requires a careful

review of the interpretation of two particle correlations.

6.4 Emission duration

An important parameter characterizing the thermal freeze out process is the emission duration $\Delta\tau$. During the freeze−out particle interactions do not cease at exactly the same time. It is rather assumed, that the last interactions happen at times t_i close to the lifetime τ of the source. The emission duration $\Delta\tau$ is defined as the width of the distribution t_i. In the YKP parametrization this quantity is directly related to the parameter R_0 [Chap95a]

$$\Delta\tau \approx R_0 \qquad 6.4$$

The values for R_0 can be taken from figure 5.7: R_0 equals zero except for the lowest k_t bin.

In the PB parametrization $\Delta\tau$ is not directly accessible. According to equation 2.28 R_{side} is only sensitive to spatial quantities, whereas R_{out} contains a temporal contribution. Hence it is possible to extract $\Delta\tau$ from the ratio R_{out} over R_{side}. The relation is approximately given by [Pra86] [Pra94][Ber89]

$$\Delta\tau \approx R_{out} - R_{side} \qquad 6.5$$

In figure 6.5 we show the ratio R_{out} over R_{side} in the central rapidity bin. It drops below unity at higher transverse momenta, which corresponds to unphysical emission times according to equation 6.5.

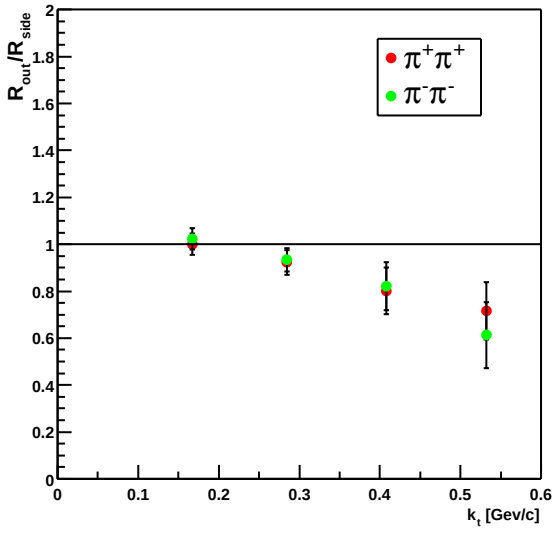

Figure 6.5

R_{out} over R_{side} in the central $Y_{\pi\pi}$ bin.

Measurements at lower beam energies yielded finite values for the source parameter $\Delta\tau$. Emission durations up to 3 fm/c were found at the AGS [Lis00] and at the SPS, using the PB [Ada02] as well as the YKP parametrization [App98]. But model calculations predict higher values for $\Delta\tau$ already at these energies (see for instance [Bea98]). Values of up to 1400 fm/c for the emission duration were experimentally found at very low energies [Lis94], but these reactions are dominated by completely different physical processes.

The "null result at RHIC" [Gyu02], i.e. the vanishing emission duration at $\sqrt{S_{NN}} = 130\,\mathrm{GeV}$, is apparently a novel feature of AA collisions at very high energies. The experimental finding was not anticipated and it is since discussed under the title "RHIC puzzle" [Dum02].

Early predictions suggested this ratio as a possible signature for the formation of a Quark Gluon Plasma. It was claimed however, that the large latent heat of a QGP would lead to a *prolongated* emission duration [Ber89][Pra86][Pra94][Gyu96] and hence to *larger* values for R_{out} over R_{side}. In figure 6.6 we show the ratio R_{out} over R_{side} extracted from model calculations based on hydrodynamics [Gyu96]. Assuming a first order phase transition, the parameter R_{out} is up to ten times larger than R_{side}(thick lines), depending on the initial conditions of the collision. If in contrast an ideal gas scenario without phase transition is considered (thin lines), the ratio remains close to unity nearly independent of the initial conditions.

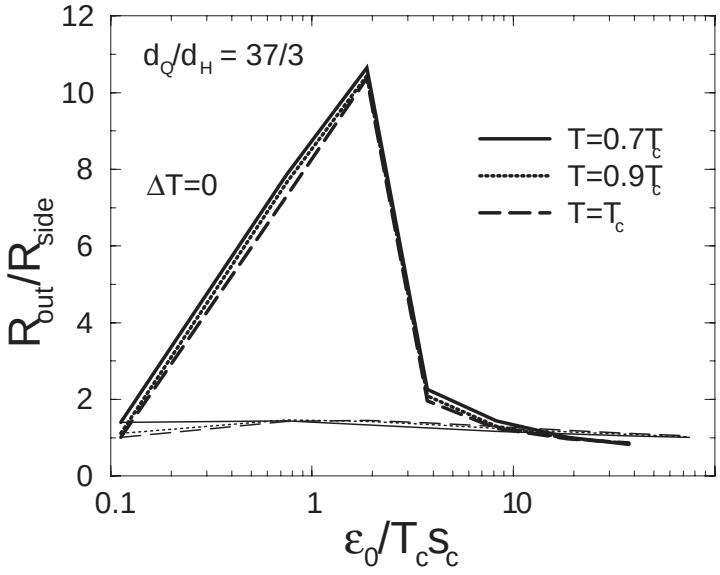

Figure 6.6

R_{out} over R_{side} derived from a hydrodynamical model [Gyu96]. The ratio is given as a function of the initial energy density ϵ_0 in units of the critical temperature T_c times the critical entropy density s_c. In this example the number of degrees of freedom in the QGP phase is $d_Q = 37$ and in the gas phase $d_H = 3$. A first order phase transition is assumed: $\Delta T = 0$. Thick (thin) lines correspond to calculations with (without) phase transition for different temperatures T.

After the first preliminary experimental results became public [Fli00][Lau01], many possible scenarios were suggested to explain the measurement [Hir02][Csö02][Tea02], so far a comprehensive and conclusive explanation sill is missing.

An example of a recent calculation is presented in [Sof01]. The first stage of the collision, when the hot and compressed nuclear matter forms a QGP phase, is described by a hydrodynamical model. At a critical temperature T_C the fluid freezes out into hadrons. A microscopic model is applied to simulate the rescattering of hadrons in the gas phase until the particles leave the interaction region. In figure 6.7 the ratio R_{out} over R_{side} at chemical and at thermal freeze out is shown, assuming two different values for T_C. Due to rescattering in the hadron gas the ratio increases at higher k_t, and it is always well above unity.

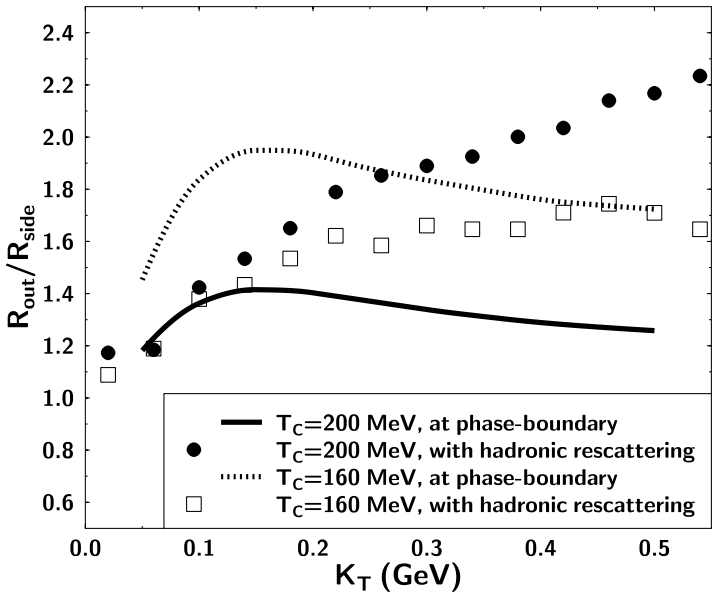

Figure 6.7

R_{out} over R_{side} dependence on transverse momentum from a recent model study [Sof01]. The ratio is above unity in the considered momentum region.

Most of the source functions assume a transparent source, i.e. particles are emitted from the entire source volume. Already at SPS energies the validity of this assumptions was discussed [Hei98]. If the source is assumed to be not transparent but opaque, i.e. particles are emitted from a surface at a fixed radius, especially the ratio R_{out} over R_{side} will be affected. A very preliminary calculation [McL02] indeed shows, that applying this freeze out condition allows to explain the experimental data.

Another reason for the discrepancy between experiment and theory is discussed in [Lin02]. In this model the approximation of the source function by a gaussian functions yields HBT radii which are up to two times larger than the radii directly derived from the source function assumed in the model. This makes it difficult to extract any information about the emission duration from the measured HBT radii.

1. Possible difficulties in using the ratio R_{out}/R_{side} as a measure for the emission duration were also discussed at lower energies. As pointed out in [Hei99] the

emission duration is the most model dependent parameter and should be interpreted with care. Fields et al. [Fie95] found at SPS energies that only for small transverse momenta this method yields the actual emission duration. At higher momenta the correlation function is strongly altered by space−momentum correlations (flow) and hence the interpretation of HBT parameters depends on the implementation of this effect into the source model. Consequently, extraction of the emission duration should only be attempted at low k_t.

6.5 Comparison to published results from RHIC

The analysis presented here is based on a reanalysis of the experimental data, which were already subject to an HBT study [Lau01][Adl01a]. The main difference between them is the improved event reconstruction of the dataset used for this analysis. Figure 6.8 shows that the extracted HBT parameters of the two independent analyses agree within statistical errors.

The Phenix collaboration has published results of an HBT study at $\sqrt{S_{NN}} = 130\,\mathrm{GeV}$ [Adc02]. Because of the different acceptance of the Phenix detector, their results extend to higher transverse momenta k_t. In figure 6.8 we compare the results from the two experiments. In the overlap region they agree well.

Preliminary results from the PHOBOS collaboration are compatible with the shown HBT radii [Man02].

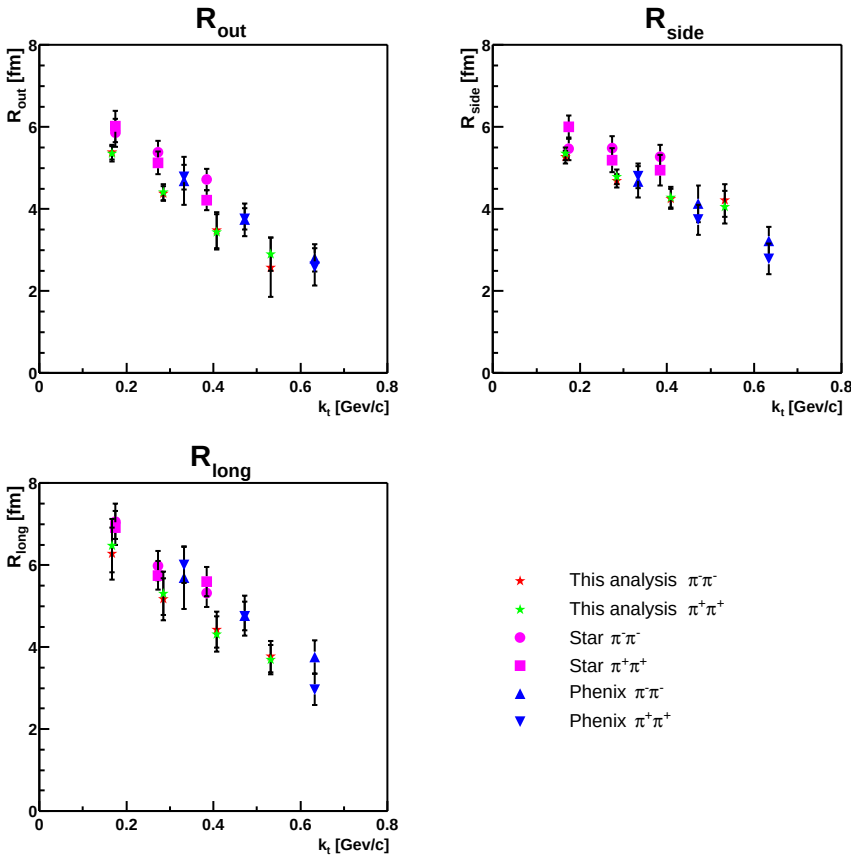

Figure 6.8

HBT radii at $\sqrt{S_{NN}} = 130\,\mathrm{GeV}$ *from different experiments and different analyses.*

6.6 HBT radii from AGS to RHIC

Most of the global observables, for example the total multiplicity, change significantly with beam energy, i.e. with the initial conditions of the heavy ion collision. The evolution of a collision at RHIC should therefore be completely different from low energy collisions at the AGS. At RHIC for instance, the initial energy density is sufficient to easily produce very heavy strange objects like the Ω particle [Cai01], whereas at lower energies these are rare. Another example is the anisotropy of the collision measured by the elliptic flow parameter v_2. It increases considerably between the highest energies at the SPS and RHIC top energy [Adl01c]. Besides these two examples there is other evidence, that the scenario changes when going from AGS to RHIC energies [QM01][QM02].

In contrast, the HBT radii change apparently very little with the beam energy. Figure 6.9 summarizes the HBT radii measured in different experiments at the AGS [Lis00], the SPS [Blu02] and at RHIC. Absolute values are similar for all energies and all radii decrease with increasing transverse momentum.

A closer inspection shows a slight increase of R_{long} with beam energy. According to equation 6.2 this corresponds to a larger life time of the system. If the system evolves from a higher initial energy density, the cool down of nuclear matter takes probably longer which increases the life time of the source.

Absolute values of the parameter R_{side} change surprisingly little with beam energy. According to equation 6.3 R_{side} is determined by the geometrical extension of the source, the strength of the transverse expansion and the temperature at freeze out. Since the interplay between these factors is not known, it is hard to make any prediction about the absolute size of R_{side}. But according to equation 6.3 the dependence of R_{side} on transverse momentum is determined by the transverse expansion. The weak increase of R_{side} at high energies, corresponds to a weak transverse expansion at higher energies. This is counter−intuitive and in contradiction with current model predictions.

The discussion of the dependence of R_{out} on beam energy is rather complicated, since this HBT radius mixes contributions from temporal and spatial components. The experimental results show no clear systematic behaviour. Using the ratio R_{out} over R_{side} as measure for the emission duration of the freeze out process yields only satisfying results at lower energies, it fails at RHIC energies.

Since many experimental uncertainties and model dependent assumptions influence the λ parameter we will not discuss it in detail. The fact, that it is well above unity at all experiments, corresponds to a clearly pronounced Bose Einstein enhancement in two particle correlations in heavy ion collisions at all energies studied so far.

The measured HBT radii can be used to associate a freeze out volume to heavy ion collisions at different energies. Based on multiplicities of the most frequent particles and the cross sections between them it is possible, to derive the mean free path length λ_f of pions in this volume [Ada02a][Tom02]. If a univeral freeze out density at a critical λ_f of ~2.5 fm is assumed the weak dependence of the HBT radii on beam energy can be explained. However, this model does not include the expansion of the source, and it is therefore perhaps an oversimplification.

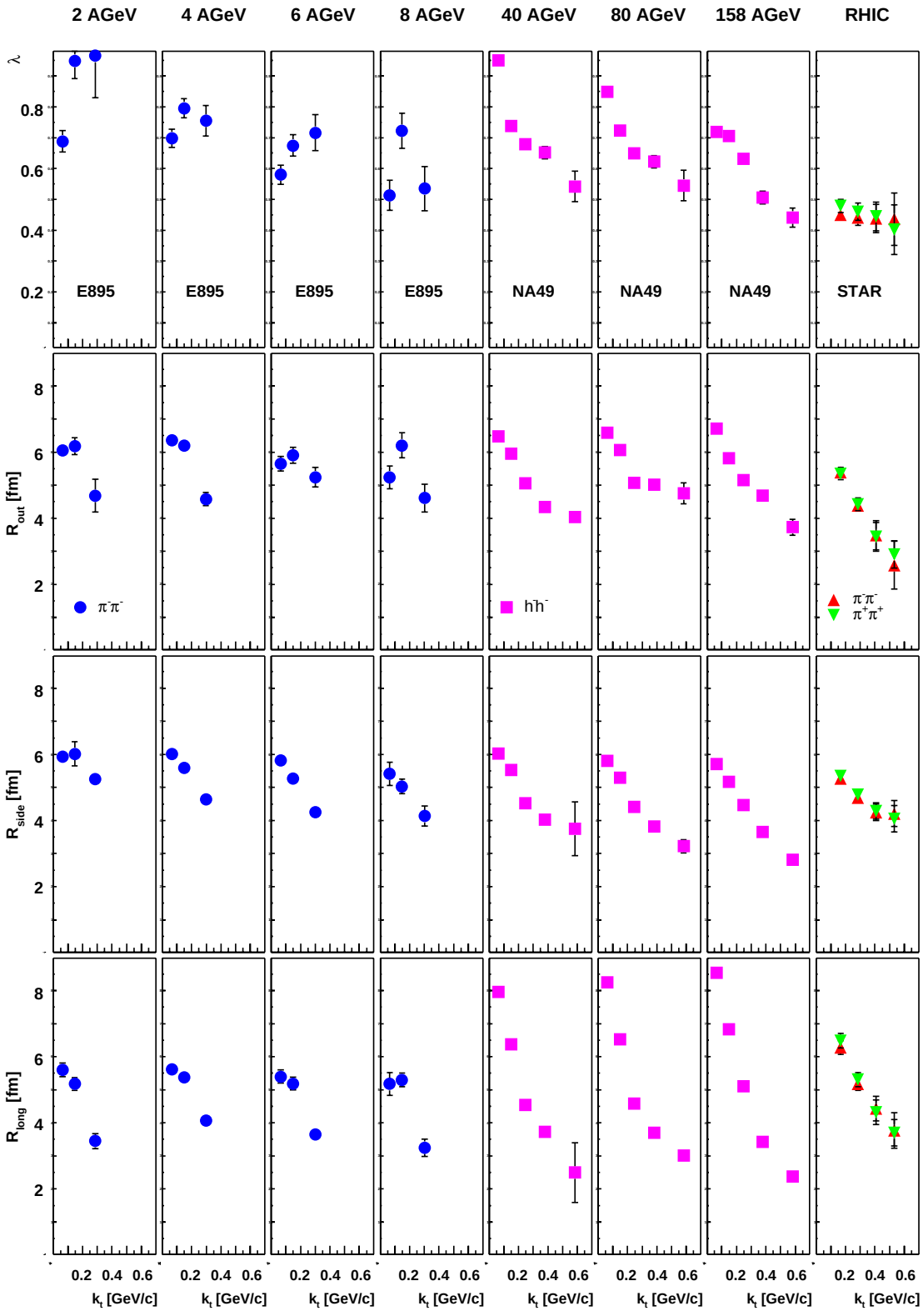

Figure 6.9

Dependence of HBT radii (PB parametrization) on transverse momentum at various beam energies at AGS [Lis00], SPS [Blu02] and RHIC.

6.7 Final considerations

Systematical uncertainties on the experimental as well as on the theoreticall side make the determination of HBT radii a difficult task. Many things, which possibly change the correlation function, were considered and if necessary a correction was applied. Nevertheless, the uncertainty in the extracted values for the HBT radii is high compared to the precision, required in many model calculations.

One aspect which was not discussed in this analysis is the contribution of long lived resonaces to the two particle correlation function. Some pions are not emitted directly from the source, but they are produced by resonace decays. These do not contribute to the HBT effect, since they are usually emitted at larger distances and at later times. It is certainly impossible to distinguish experimentally pions which are decay products of long lived resonaces from "thermal" pions. This effect might cause deviations of the correlation function from a Gaussian shape and may hence interfere with a proper fit. It might even produce a halo like emission function which would require a completely different fit function [Wie97]. In a recent review [Tom02] it is argued however that the contributions from resonace decays are small and therefore it is neglected in this analysis.

Another problem represents a correct treatment of the coulomb effect. The two particle correlation due to the coulomb effect could only be calculated, if the emission times and points were known. But this information is given by exactly the source function, which we are looking for with the study of the Bose Einstein correlations. After all, the correction method applied here is acceptable, since the finally extracted HBT radii are compatible to the radius assumed for the coulomb source. In some analyses this consistency is ensured by simultaneously considering the HBT correlations and the coulomb correction in the fit procedure [Blu02]. Another approach is to use the experimetally measured $\pi^+\pi^-$ correlations, which are only due to the coulomb force, to quantify the correction for the like sign correlations, e.g. [App98]. This method doesn't solve the problem either, since the correlation function due to the attractive coulomb force equals not exactly the inverse of the correlation function in the repulsive case and the topology of $\pi^+\pi^-$ pairs is quite different from the topology of like sign pairs.

A fraction of particles used to construct the correlation function are not thermal pions obeying Bose−Einstein statistics. For example, with the particle identification in the TPC it is hard to distinguish between pions and electrons. Also pions from resonace decays do not contribute to the Bose−Einstein enhancement. The coulomb correction however is applied to each particle pair, and hence the correlation function is overcorrected in this sense. But since it is not known which fraction of the detected pions contributes to HBT effect, it is hard to take this effects into account.

7. Conclusion and outlook

In this thesis we presented an analysis of the two pion correlation function in AuAu collisions at $\sqrt{S_{NN}} = 130\,\mathrm{GeV}$. The experimental data were collected with the STAR detector at the RHIC collider in Brookhaven.

The correlation functions were studied in different momentum regions using the Pratt−Bertsch as well as the Yano−Koonin−Podgoretskii parametrization. The analysis was performed for negative and positive charged pions separately. No significant difference between these two cases was observed.

The correlation functions show no systematic dependence on the longitudinal pair rapidity. The linear dependence of the YKP rapidity on longitudinal pair rapidity indicates strong longitudinal expansion, it is compatible with longitudinal boost invariance of the source.

The dependence of the parameter R_{long} on transverse momentum is related to the life time of the system. Fitting the Mahklin−Sinyukov approximation to the data yields a life time of ~8 fm/c. This result is close to measurements at lower energies. The life time was expected to increase with beam energy, since the system is assumed to be larger at freeze out when it started from a higher initial energy density.

The dependence of the HBT radius parameter R_{side} on transverse momentum is determined by the strength of the transverse expansion. Fitting a simple approximation to the measured dependence we extract the strength of the transverse expansion over temperature $\eta_f^2/T \approx 4.5$. This result is compatible with a moderate mean transverse expansion velocity of v_t~0.6. In order to resolve ambiguities in the interpretation of this parameter, one had to consider single particle transverse momentum spectra and the dependence of R_{side} on transverse momentum simultaneously. Simply comparing the R_{side} dependence on transverse momentum at different beam energies yields the counter−intuitive observation, that with increasing initial energy density the transverse expansion velocity does not increase.

The most puzzling result however is the vanishing emission duration. The parameter R_0 in the YKP parametrization and the ratio R_{out} over R_{side} in the PB parametrization are used to determine the emission duration. Both methods yield consistently very small or even vanishing values for the emission duration. The ratio R_{out} over R_{side} drops below unity, applying the usual first order approximation to derive the emission duration yields unphysical results. The observation of this "explosive" freeze out comes as a surprise, especially since early predictions suggested large values of the emission duration as a signature for the formation of a QGP. The theoretical implications of this experimental result are currently intensely discussed.

In summary, the weak dependence of the measured HBT radii on beam energy and the vanishing emission duration do not fit into a comprehensive picture of the evolution of a heavy ion collision at high energies.

The existing STAR data are subject to several more sophisticated analyses [Ray02]. Three particle correlations allow to test the chaoticity of the source [Wil02]. HBT

with kaons or protons will help to quantify collective effects [Lop02]. We will gain more insight into the last stages of the collision by studying the correlations of non−identical particles [Ret02a]. Flow analyses allow to determine the reaction plane for each event, this information can be used to test the azimuthal dependence of HBT radii [Wel03].

Besides the ongoing analyses, future runs at the RHIC collider will expand the systematics of "soft" physics in AA collisions. HBT radii will be measured at various beam energies and probably also for lighter systems. The STAR detector system will be expandend, yielding a higher acceptance, higher momentum resolution and better particle identification capabilities. With these improvements the quality of the measurements will further increase. Along with the progress in model calculations this will eventually allow to draw a more comprehensive conclusive picture of the evolution of a heavy ion collision at RHIC energies.

In 2007 the LHC collider at CERN will generate heavy ion collision at $\sqrt{S_{NN}} = 5500\,\mathrm{GeV}$. Large detector systems, like ALICE, will measure several thousand particles produced with each central collision. Results obtained at this energy will hopefully help us to understand better what we currently observe at RHIC.

8. Appendix

8.1 Appendix A

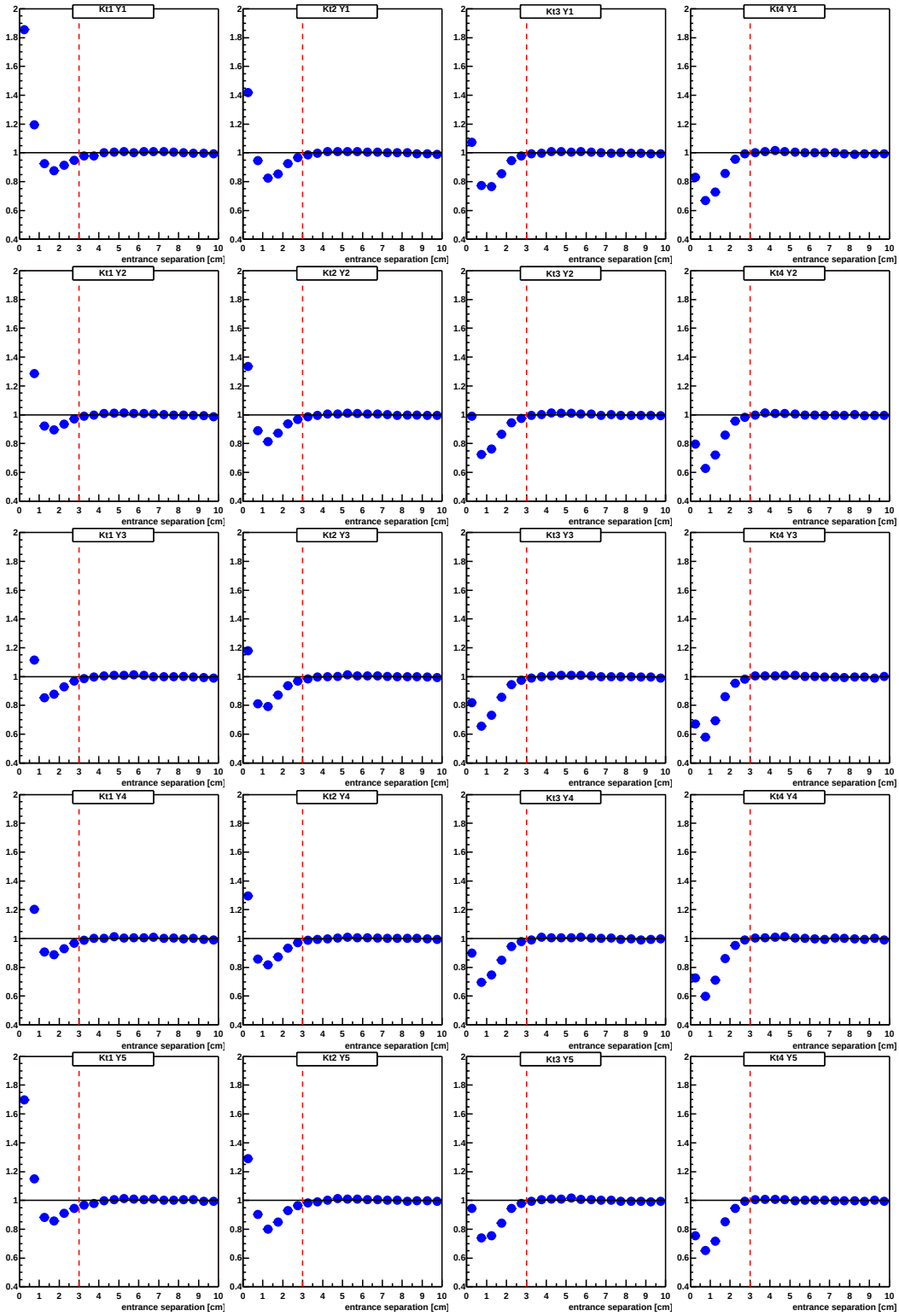

Entrance separation correlation function in different $k_t - Y_{\pi\pi}$ bins.

For explanation see chapter 4.4.1 (naming of the bins according to chapter 5.6).

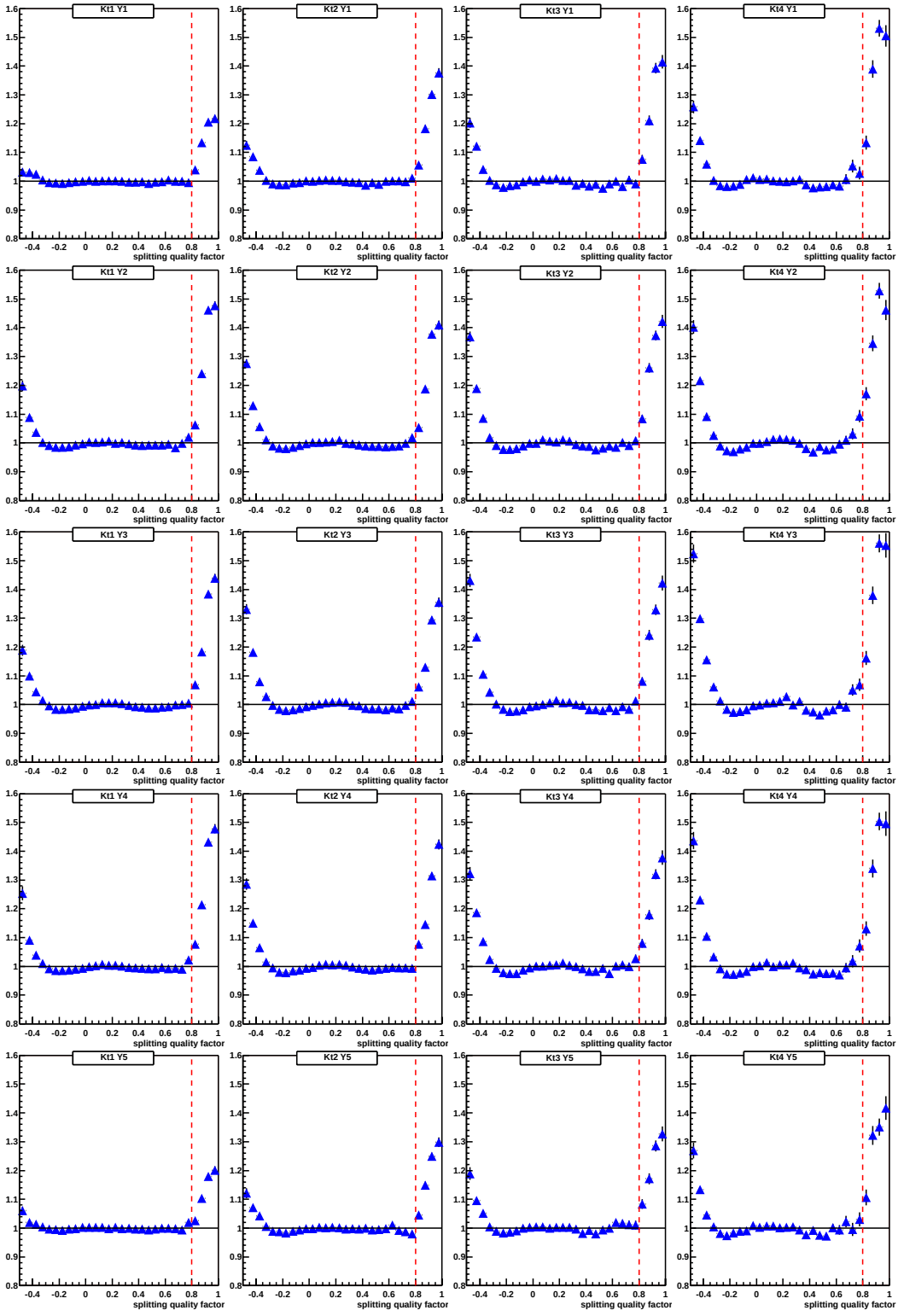

Splitting quality correlation function in different $k_t - Y_{\pi\pi}$ bins.

For explanation see chapter 4.4.2 (naming of the bins according to chapter 5.6).

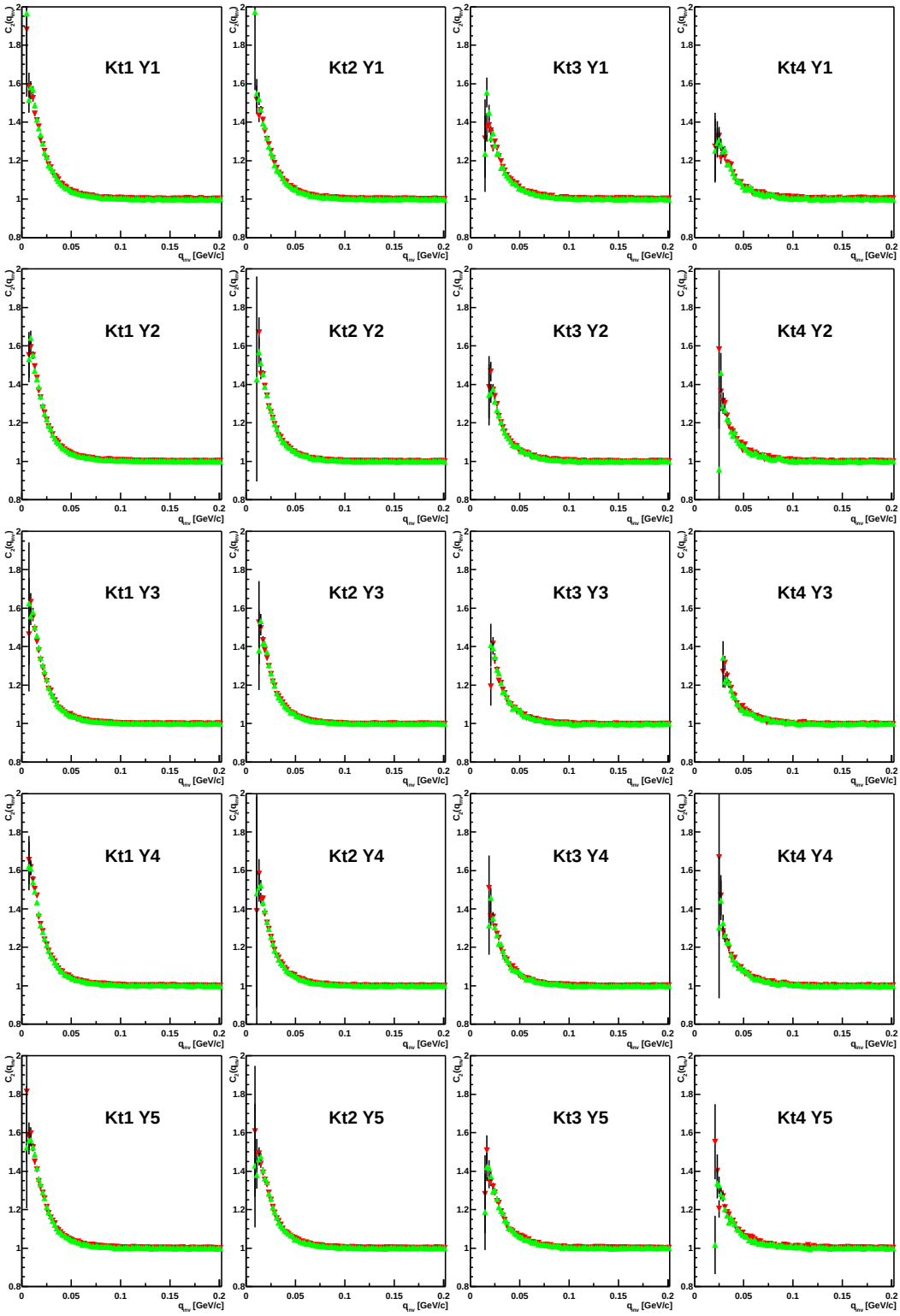

Q_{inv} correlation function in different k_t−$Y_{\pi\pi}$ bins (bins are named according to chapter 5.6). For explanation see chapter 5.1.

8.2 Appendix B

Table B1:

$\pi^+\pi^+$ correlation function

YKP parametrization

$<Y_{\pi\pi}>$	$<k_t>$	λ	R_{para}	R_{perp}	R_0	β
−0.728	0.168	0.463 ±0.0237	6.58 ±0.271	5.13 ±0.176	1.64 ±1.2	0.0407 ±0.0514
−0.73	0.286	0.466 ±0.0266	5.39 ±0.226	4.61 ±0.139	0 ±1.8	0.0476 ±0.0511
−0.732	0.409	0.438 ±0.0424	4.34 ±0.282	4.06 ±0.205	0 ±0.898	0.0217 ±0.0779
−0.733	0.533	0.422 ±0.0715	3.89 ±0.405	3.66 ±0.309	0 ±1.24	−0.0107 ±0.117
−0.379	0.168	0.455 ±0.0201	6.48 ±0.219	5.19 ±0.151	1.82 ±0.998	0.058 ±0.0444
−0.382	0.286	0.464 ±0.0262	5.33 ±0.208	4.61 ±0.132	0.0182 ±1.61	0.00842 ±0.0473
−0.386	0.409	0.434 ±0.0425	4.32 ±0.258	3.96 ±0.194	0 ±0.888	0.0554 ±0.0743
−0.388	0.533	0.464 ±0.0797	3.77 ±0.368	3.84 ±0.301	0 ±1.3	0.0246 ±0.121
0	0.167	0.476 ±0.0216	6.49 ±0.221	5.3 ±0.152	1.27 ±1.44	−0.0303 ±0.047
0	0.285	0.458 ±0.0276	5.34 ±0.217	4.65 ±0.142	0 ±1.12	−0.0314 ±0.0493
0	0.408	0.441 ±0.0458	4.4 ±0.286	4 ±0.2	0 ±0.918	0.0081 ±0.0739
0	0.532	0.417 ±0.0837	3.73 ±0.404	3.71 ±0.341	0.00337 ±1.07	−0.0356 ±0.139
0.378	0.168	0.438 ±0.02	6.35 ±0.22	5.21 ±0.157	0.91 ±1.99	−0.0459 ±0.0481
0.382	0.286	0.458 ±0.0263	5.3 ±0.212	4.65 ±0.135	0 ±1.1	−0.0248 ±0.0487
0.385	0.409	0.437 ±0.044	4.33 ±0.275	4.06 ±0.2	0 ±0.838	−0.0296 ±0.0748
0.387	0.533	0.42 ±0.0768	3.78 ±0.392	3.64 ±0.315	0 ±0.999	−0.0463 ±0.122
0.728	0.168	0.461 ±0.0237	6.54 ±0.268	5.17 ±0.182	1.18 ±1.73	−0.0645 ±0.0542
0.73	0.286	0.474 ±0.0275	5.4 ±0.229	4.66 ±0.143	0 ±1.69	0.00299 ±0.0512
0.732	0.409	0.46 ±0.0431	4.3 ±0.276	4.15 ±0.199	0 ±0.887	0.0185 ±0.078
0.733	0.533	0.422 ±0.0738	3.64 ±0.404	3.92 ±0.33	0 ±1.25	0.0289 ±0.138

Table B2:

$\pi^-\pi^-$ correlation function

YKP parametrization

$<Y_{\pi\pi}>$	$<k_t>$	λ	R_{para}	R_{perp}	R_0	β
−0.728	0.168	0.433 ±0.0212	6.32 ±0.255	5.03 ±0.168	1.16 ±1.57	0.0363 ±0.0514
−0.73	0.286	0.459 ±0.025	5.29 ±0.215	4.6 ±0.132	0.00124 ±1.75	0.0324 ±0.0488
−0.732	0.409	0.445 ±0.0416	4.43 ±0.281	4.03 ±0.193	0 ±0.849	0.0231 ±0.0725
−0.733	0.533	0.421 ±0.071	3.86 ±0.407	3.72 ±0.3	0 ±1.07	0.0104 ±0.123
−0.379	0.168	0.444 ±0.0191	6.43 ±0.213	5.17 ±0.147	1.4 ±1.23	0.0577 ±0.0435
−0.382	0.286	0.466 ±0.0251	5.37 ±0.197	4.64 ±0.128	0 ±1.08	0.0428 ±0.045
−0.386	0.409	0.461 ±0.045	4.57 ±0.275	4.09 ±0.192	0.00278 ±0.83	0.0202 ±0.0694
−0.388	0.533	0.436 ±0.0826	3.87 ±0.399	3.79 ±0.338	0 ±1.08	0.0244 ±0.122
0	0.167	0.448 ±0.02	6.32 ±0.214	5.26 ±0.153	1.48 ±1.24	0.0267 ±0.0464
0	0.285	0.439 ±0.0249	5.21 ±0.2	4.55 ±0.132	0 ±1.1	0.00325 ±0.0481
0	0.408	0.435 ±0.0464	4.51 ±0.297	4.02 ±0.204	0.00199 ±1.12	0.00469 ±0.0724
0	0.532	0.421 ±0.083	3.77 ±0.414	3.69 ±0.326	0 ±1.08	0.000272 ±0.131
0.378	0.168	0.45 ±0.0197	6.49 ±0.218	5.24 ±0.152	1.46 ±1.21	−0.0636 ±0.0444
0.382	0.286	0.456 ±0.0255	5.3 ±0.202	4.64 ±0.133	0 ±1.3	−0.0105 ±0.0481
0.385	0.409	0.446 ±0.0437	4.34 ±0.274	4.14 ±0.195	0 ±1.15	0.0249 ±0.0736
0.387	0.533	0.377 ±0.0631	3.43 ±0.354	3.47 ±0.283	0 ±0.913	−0.097 ±0.123
0.728	0.168	0.452 ±0.0228	6.47 ±0.265	5.2 ±0.177	1.14 ±1.77	−0.0567 ±0.0534
0.73	0.286	0.453 ±0.0258	5.36 ±0.228	4.59 ±0.138	0 ±1.98	−0.0337 ±0.0501
0.732	0.409	0.461 ±0.0438	4.57 ±0.285	4.13 ±0.198	0 ±0.983	−0.0278 ±0.0749
0.733	0.533	0.389 ±0.0671	3.62 ±0.393	3.58 ±0.319	0 ±0.89	−0.0299 ±0.123

Table B3:

$\pi^+\pi^+$ correlation function

PB parametrization

$<Y_{\pi\pi}>$	$<k_t>$	λ	R_{side}	R_{out}	R_{long}	$R_{outlong}$
−0.728	0.168	0.471 ±0.024	5.21 ±0.185	5.26 ±0.212	6.61 ±0.267	0.0014 ±1.49
−0.73	0.286	0.472 ±0.0271	4.71 ±0.175	4.52 ±0.195	5.37 ±0.223	0.0 ±1.22
−0.732	0.409	0.444 ±0.0429	4.39 ±0.253	3.64 ±0.27	4.38 ±0.282	0.0022 ±4.07
−0.733	0.533	0.421 ±0.0727	3.98 ±0.37	2.74 ±0.644	3.71 ±0.539	0.0 ±1.22
−0.379	0.168	0.461 ±0.0203	5.23 ±0.156	5.38 ±0.187	6.48 ±0.216	0.0 ±1.1
−0.382	0.286	0.468 ±0.0265	4.67 ±0.165	4.51 ±0.186	5.31 ±0.205	0.0012 ±1.33
−0.386	0.409	0.439 ±0.0429	4.25 ±0.238	3.53 ±0.261	4.34 ±0.253	0.0 ±1.46
−0.388	0.533	0.473 ±0.0811	4.15 ±0.365	3.21 ±0.7	3.75 ±0.491	0.0 ±1.98
0.0	0.167	0.479 ±0.0217	5.35 ±0.16	5.35 ±0.188	6.48 ±0.218	0.0 ±0.793
0.0	0.285	0.46 ±0.0277	4.79 ±0.178	4.42 ±0.194	5.31 ±0.213	0.0018 ±1.35
0.0	0.408	0.445 ±0.0467	4.29 ±0.248	3.44 ±0.432	4.32 ±0.376	0.0 ±1.62
0.0	0.532	0.402 ±0.0801	4.05 ±0.401	2.9 ±0.414	3.7 ±0.397	0.0 ±3.61
0.378	0.168	0.439 ±0.0199	5.23 ±0.163	5.22 ±0.191	6.33 ±0.217	0.0 ±1.08
0.382	0.286	0.455 ±0.0262	4.76 ±0.171	4.45 ±0.188	5.26 ±0.209	0.0 ±1.15
0.385	0.409	0.438 ±0.0446	4.42 ±0.247	3.15 ±0.391	4.18 ±0.349	1.47 ±0.957
0.387	0.533	0.417 ±0.0783	4.08 ±0.374	2.47 ±0.618	3.68 ±0.496	0.0 ±1.14
0.728	0.168	0.466 ±0.0239	5.22 ±0.191	5.26 ±0.217	6.53 ±0.264	0.0013 ±1.71
0.73	0.286	0.48 ±0.0281	4.75 ±0.18	4.56 ±0.196	5.4 ±0.227	0.0 ±1.47
0.732	0.409	0.455 ±0.0427	4.49 ±0.25	3.27 ±0.399	4.11 ±0.357	1.56 ±0.965
0.733	0.533	0.436 ±0.0772	4.39 ±0.418	2.59 ±0.723	3.45 ±0.516	2.05 ±0.947

Table B4:

$\pi^-\pi^-$ correlation function

PB parametrization

$<Y_{\pi\pi}>$	$<k_t>$	λ	R_{side}	R_{out}	R_{long}	$R_{outlong}$
−0.728	0.168	0.441 ±0.021	5.12 ±0.172	5.09 ±0.197	6.35 ±0.245	0.0 ±2.23
−0.73	0.286	0.465 ±0.0247	4.71 ±0.164	4.49 ±0.18	5.29 ±0.207	0.0 ±3.9
−0.732	0.409	0.442 ±0.0403	4.32 ±0.235	3.55 ±0.244	4.43 ±0.269	0.0 ±2.36
−0.733	0.533	0.442 ±0.0731	4.2 ±0.365	2.86 ±0.644	3.87 ±0.521	0.0 ±1.56
−0.379	0.168	0.447 ±0.0188	5.19 ±0.151	5.27 ±0.176	6.42 ±0.206	0.0 ±1.04
−0.382	0.286	0.468 ±0.0248	4.79 ±0.16	4.45 ±0.172	5.33 ±0.19	0.0 ±1.26
−0.386	0.409	0.462 ±0.045	4.44 ±0.238	3.55 ±0.331	4.56 ±0.312	0.0128 ±2.45
−0.388	0.533	0.444 ±0.0821	4.27 ±0.41	2.21 ±0.738	3.59 ±0.488	2.14 ±0.883
0.0	0.167	0.45 ±0.0197	5.27 ±0.155	5.39 ±0.184	6.28 ±0.207	0.0 ±0.859
0.0	0.285	0.441 ±0.0245	4.69 ±0.165	4.38 ±0.178	5.17 ±0.192	0.0 ±1.12
0.0	0.408	0.438 ±0.046	4.25 ±0.245	3.49 ±0.44	4.43 ±0.372	0.0 ±1.43
0.0	0.532	0.436 ±0.0847	4.21 ±0.395	2.58 ±0.728	3.77 ±0.543	1.15 ±1.61
0.378	0.168	0.45 ±0.0194	5.25 ±0.154	5.37 ±0.183	6.46 ±0.212	0.0022 ±1.16
0.382	0.286	0.451 ±0.0249	4.74 ±0.162	4.38 ±0.187	5.25 ±0.194	0.0 ±1.27
0.385	0.409	0.446 ±0.0435	4.39 ±0.242	3.46 ±0.447	4.19 ±0.365	1.51 ±1.03
0.387	0.533	0.382 ±0.0628	4.03 ±0.358	1.95 ±0.464	3.29 ±0.412	1.83 ±0.633
0.728	0.168	0.454 ±0.0225	5.22 ±0.181	5.27 ±0.211	6.46 ±0.258	0.0 ±2.29
0.73	0.286	0.445 ±0.0251	4.65 ±0.172	4.33 ±0.187	5.29 ±0.218	0.002 ±2.47
0.732	0.409	0.457 ±0.0438	4.45 ±0.246	3.56 ±0.344	4.59 ±0.305	0.006 ±1.93
0.733	0.533	0.387 ±0.0657	4.18 ±0.4	2.05 ±0.55	3.38 ±0.479	1.87 ±0.755

9. Bibliography

[Ada02] D. Adamová et al., nucl−ex/0207005 (2002)

[Ada02a] D. Adamová et al., nucl−ex/0207008 (2002)

[Adc02] K. Adcox et al., Phys. Rev. Lett **88** (2002) 192302

[Adl01] C. Adler et al., NIM **A 470** (2001) 488−499

[Adl01a] C. Adler et al. Phys. Rev. Lett. **87** (2001) 082301

[Adl01b] C. Adler et al., Phys. Rev. Lett. **87** (2001) 112303

[Adl01c] C. Adler et al. Phys. Rev. Lett. **87** (2001) 182301

[Adl02] C. Adler, Ph.D. thesis, IKF University of Frankfurt, in preparation

[App98] H. Appelshäuser et al., Eur. Phys. J., **C 2** (1998) no.4, 661

[Arn83] G. Arnison et al., Phys. Letters **122 B** (1983)

[Bas99] S.A. Bass et al., J. Phys. **G 25** No 3, (1999), R1−R57

[Bea98] I.G. Bearden et al., Phys. Rev. **C 58** (1998) 1656

[Ber89] G.F. Bertsch, Nucl. Phys. **A 498** (1989) 173c

[Bjo83] J.D. Bjorken, Phys. Rev. **D 27** (1983) 140

[Bla99] J.−P. Blaizot, Proc. of QM99, Nucl. Phys. **A 661** (1999), 3c

[Blu93] W. Blum and L. Rolandi , "Particle Detection with Drift Chambers", Springer Verlag, Berlin, (1993)

[Blu02] C. Blume et al., "Results on Correlations and Fluctuations from the NA49 collaboration", Proc. of QM02, to be published in Nucl. Phys. A

[Boa90] D.H. Boal et al., Rev. Mod. Phys. **62** (1990) 553

[Bra01] P. Braun−Munzinger, nucl−ex/0007021 (2001)

[Bro02] W. Broniowski and W. Florkowski, nucl−th/0208061 (2002)

[Cai01] H. Caines, Proc. of QM01, Nucl. Phys. **A 698** (2002) 112c

[Cal01] M. Calderon, Ph.D. Thesis, Yale University (2001)

[Cha95] S. Chapman, P. Scotto and U. Heinz, Heavy Ion Physics **1** (1995) 1

[Cha95a] S. Chapman, J. Nix and U. Heinz, Phys. Rev **C 52** (1995) 2694

[Cre86] M. Creutz, "Quarks, Gluons and Lattices", Cambrige Univ. Press, Cambridge, (1986)

[Csö94] T. Csörgö and L. Csernai, Phys. Lett. **B 333** (1994) 494

[Csö95] T. Csörgö and B. Lörstad, Nucl. Phys. **A 590** (1995) 465

[Csö96] T. Csörgö and B. Lörstad, Phys. Rev. **C 54** (1996) 1390

[Csö02] T. Csörgö and A. Ster, nucl−th/0207016

[Cse94] L.P. Csernai, "Introduction to Relativistic Heavy Ion Collisions", John Wiley & Sons, Chichester, (1994)

[Dum02] A. Dumitru, nucl−th/020611 (2002)

[Fey88] R.P. Feynman, "QED", Princetion Univ. Press, Princeton, (1988)

[Fli00] D. Flierl, Contribution of the STAR Collaboration at the APS Division of Nuclear Physics meeting, October 4−7, 2000, Williamsburg,Virgina

[Fie95] D.E. Fields, Phys. Rev. **C 52** (1995) 986

[Gol59] G. Goldhaber et al., Phys. Rev. Lett. **3** (1959) 181

[Gol60] G. Goldhaber, S. Goldhaber, W. Lee and A. Pais, Phys. Rev. **120** (1960) 300

[Gre89] W. Greiner and T. Schäfer, "Quantenchromodynamik", Verlag Harri Deutsch, Frankfurt am Main (1989)

[Gyu79] M. Gyulassy et al., Phys. Rev. **C 20** (1979) 2267

[Gyu96] M. Gyulassy and D. Rischke, Nucl. Phys. **A 608** (1996) 479

[Gyu02] M. Gyulassy and D. Rischke, "Why is the Null HBT result at RHIC so Interesting ?", Proc. Budapest ’02 Workshop on Quark and Hadron Dynamics, to be published in Heavy Ion Physics

[Han54] R. Hanburry Brown and R.Q. Twiss, Phil. Mag. **45 (**1954) 663

[Han58] R. Hanburry Brown and R.Q. Twiss, Nature **177** (1956) 27;
ibid. **178** (1956) 1046; Proc. Roy. Soc. **A 242** (1957) 300;
ibid. **243** (1957) 291; ibid. **248** (1958) 199; ibid. **248** (1958) 222

[Har02] J.W. Harris, Proc. of QM01, Nucl. Phys. **A 698** (2002) 64c

[Hei98] H. Heiselberg and A. Vischer, Eur. Phys. J. **C1** (1998) 593

[Hei97] U.Heinz and Q.H. Zhang, Phys. Rev. **C 56** (1997) 426

[Hei99] U.Heinz and B. Jacak, Annu. Rev. Nucl. Part. Sci. **49** (1999) , pp.529−579

[Hei99a] U. Heinz and U. Wiedemann, Phys. Rep. **319** (1999) 145

[Hei00] U. Heinz and M. Jacob, CERN press release, (2000)

[Hei02] U. Heinz and P. Kolbl, hep−ph/0204061 (2002)

[Hei02a] U. Heinz and P. Kolbl, Nucl .Phys., **A 702** (2002) 269

[Her95] M. Herrmann and G.F. Bertsch, Phys. Rev **C 51** (1995) 328

[Hir02] T. Hirano and K. Tsuda, QM02, nucl−th/0208068 (2002)

[Hoo96] G. t’Hooft, "In Search for the Ultimate Building Blocks", Cambridge Univ. Press, Cambridge (1996)

[Jac62] J.D. Jackson, "Classical Electrodynamics", J. Wiley & Sons, London (1962)

[Kar01] F. Karsch, "Lattice QCD at High Temperature and Density", hep−lat/0106019

References [Nim03DAQ] to [Nim03TRI] will be published in "Nuclear Instruments and Methods" in a special volume dedicated to RHIC

[Nim03DAQ] J. Landgraf et al., "An Overview of the STAR DAQ System"

[Nim03EMC] T. Cormier et al., "The STAR Barrel Electromagnetic Calorimeter"

[Nim03EEMC] S. Vigdor et al., "The STAR Endcap Electromagnetic Calorimeter"

[Nim03FTPC] P. Seyboth et al., "The Forward Time Projection (FTPC) Chamber in STAR"

[Nim03L3] C. Adler et al., "The STAR Level−3 Trigger System"

[Nim03OV] J. Harris et al., "STAR Detector Overview"

[Nim03RICH] J. Dunlop et al., "Identification of High p_t Particles with the STAR−RICH detector"

[Nim03SSD] J. Baudot et al., "The STAR Silicon Strip Detector (SSD)"

[Nim03SVT] R. Bellwied et al., "The STAR Silicon Vertex Tracker: A Large Area Silicon Drift Detector"

[Nim03TPC] J. Thomas et al., "The STAR Time Projection Chamber: A Unique Tool for Studying High Multiplicity Events at RHIC"

[Nim03TRI] H. Crawford et al., "The STAR Trigger"

[Kop72] G. Kopylov et al., Sov. J. Nucl. Phys. **15** (1972) 219

[Lan00] S. Lange et al., NIM **A 453** (2000) 397

[Lau01] F. Laue for the STAR collaboration, Nucl. Phys. **A 698** (2002) 177c

[Lin02] Z. Lin etal, nucl−th/0204054 (2002)

[Lis94] M. Lisa et al., Phys. Rev. **C 49** (1994) 2788

[Lis96] M. Lisa, "The STAR TPC Clusterfinder/Hitfinder", STAR Note 238, 7 February 1996

[Lis99] M. Lisa, Proc. of QM99, Nucl. Phys. **A 661** (1999) 444c

[Lis00] M. Lisa et al., Phys. Rev. Lett. **84** (2000) 2798

[Lop02] M. López Noriega, "Identical Particle Interferometry at STAR", Proc. of QM02, to be published in Nucl. Phys. **A**

[Mak88] A. Makhlin and Y. Sinyukov, Z. Phys. **C 39** (1988) 69

[Man02] S. Manly for the PHOBOS collaboration, Proceedings of Quark Matter 2002, to be published in Nucl. Phys. A

[McL02] L. McLerran and S. Padula, nucl−th/0205028

[Mes61] A. Messiah, "Quantum Mechanics Vol I", North Holland, (1961)

[Min94] Application Software Group CERN, Function Minimization and Error Analysis, (CERN Program Library Long Writeup D506), (1994)

[Mis73] C.W. Misner et al., "Gravitation", WH Freeman & Co, (1973)

[Pra86] S. Pratt, Phys. Rev. **D 33** (1986) 72

[Pra94] S. Pratt, Phys. Rev. **C 49** (1994) 2722

[Pod83] M. Podgorestikii, Sov. J. Nucl. Phys. **37** (1983) 272

[Ray02] L. Ray, "Correlations, Flutuations and Flow Measurements from the STAR Experiment", Proceedings of QM02, to be published in Nucl. Phys. **A**

[Ros02] T. Roser, Proc. of QM01, Nucl. Phys. **A 698** (2002) 23c

[Ret02] F. Retiere, Proc. of QM01, Nucl. Phys. **A 698** (2002) 408c

[Ret02a] F. Retiere, "Non identical particle correlation analysis as a probe of transverse flow", Proc. of QM02, to be published in Nucl. Phys. **A**

[QM01] Proc. of the Quark Matter Conference 2001, Nucl. Phys. **A698**

[QM02] Proc. of the Quark Matter Conference 2002, to be published in Nucl. Phys. **A**

[Sch94] E. Schnedermann and U. Heinz, Phys. Rev. **C 50** (1994) 1675

[Sch99] R. Scheibl and U. Heinz, Phys. Rev. **C 59** (1999) 1585

[Shu73] E. Shuryak, Phys. Lett. **B44** (1973) 387

[Shu80] E. Shuryak, Phys. Reports **61**, (1980)

[Sof01] S. Soff et al., Phys. Rev. Lett. **86** (2001) 3981

[Sof02] S. Soff et al., nucl−th/209055 (2002)

[Tea02] D. Teaney, nucl−th/0209024 (2002)

[Tom02] B. Tomasik and U. Wiedemann, "Central and Non−central HBT from AGS to RHIC", hep−ph/0210250 (2002)

[Vig99] S. Vigdor, "The RHIC Spin Program: Snapshots of Progress", hep−ex/9905034 (1999)

[Wei97] R.M. Weiner., "*Bose−Einstein Correlations in Particle and Nuclear Physics"*, Wiley, Chichester, (1997)

[Wei00] R.M. Weiner, "*Introduction to Bose−Einstein Correlations and Subatomic Interferometry"*, Wiley, Chichester, (2000)

[Wei00a] R.M. Weiner, Phys. Rep. **327**, (2000) 249

[Wel03] R. Wells, Ph.D. thesis, Ohio State University, in preparation

[Wie97] U. Wiedemann and U. Heinz, Phys. Rev. **C 56** (1997) 610

[Wie99] U. Wiedemann, Proc. of QM99, Nucl. Phys. **A 661** (1999) 65c

[Wil02] R. Willson, "Measurement of Source Chaoticity for Particle Emission in Au+Au Collisions at $\sqrt{S_{NN}} = 130\,\mathrm{GeV}$ using 3−Particle HBT Correlations", Proc. of QM02, to be published in Nucl. Phys. **A**

[Won94] C. Wong, "Introduction to High Energy Heavy Ion Collisions",

World Scientific Publishing, Singapore (1994)

[Wu98] Wu et al., Eur. Phys. J. **C1** (1998) 599

[Zsc02] D. Zschiesche et al., Phys. Rev. **C 65** (2002) 064902

[Yan78] F. Yano and S. Koonin, Phys. Lett. **B 78** (1978) 556

[Xu01] N. Xu and M. Kaneta for the STAR collaboration, Nucl. Phys. **A698** (2002) 306c

Danksagung

Zuerst möchte ich mich bei Prof. Stock für die optimalen Bedingungen, unter denen diese Arbeit entstehen konnte, bedanken.

Bei allen Mitgliedern der STAR Kollaboration bedanke ich mich für die gelungene Durchführung des Experimentes. Neben dem Spokesman John Harris gebührt der STAR HBT Gruppe und ihrem Protagonisten Mike Lisa besonderer Dank.

Bei Raimond Snellings möchte ich mich für die Einladung nach Berkeley und für viele Diskussionen bedanken.

Bei allen Kollegen der L3 Gruppe bedanke ich mich für die erfolgreiche Zusammenarbeit. Insbesondere natürlich bei den "Frankfurtern" Christof Struck, Sören Lange und natürlich bei meinem zeitweiligen Mitbewohner Jens Berger. Der nächsten Schicht, Thomas Dietel und Thorsten Kollegger, wünsche ich weiterhin viel Erfolg und einen angenehmen Aufenthalt in Amerika.

Bei allen Mitarbeitern des IKF bedanke ich mich, insbesondere bei Werner Amend, Peter Dinkelaker, Roland Bramm, Alexander Wetzler, Herbert Ströbele und Marek Gazdzicki.

Ein besonderer Dank gilt Clemens Adler für all seine zynischen Kommentare und seine stete Bereitschaft, Kaffee trinken zu gehen.

Zuletzt bedanke ich mich bei meiner Familie, die mir ermöglicht hat, diesen Weg einzuschlagen und die mich immer unterstützt hat.

Zuallerletzt bedanke ich mich bei Beate und bei Anouk Maximilian Widukind, für Alles.

Lebenslauf

Dominik Bernhard Flierl

Rubenheimer Str. 89 a

66399 Erfweiler−Ehlingen

geboren am 5.11.1971 in Blieskastel

1978−1982 Grundschule Erfweiler−Ehlingen

1982−1991 Von der Leyen Gymnasium Blieskastel

1991−1994 Studium der Physik an der Universität des Saarlandes Saarbrücken

1994−1998 Studium der Physik an der Johann Wolfgang Goethe Universität in Frankfurt am Main

1998 Diplom in Physik,

Titel der Diplomarbeit: "Bestimmung der transversalen Expansion in einer Schwerionenreaktion durch die Analyse von Zweiteilchenkorrelationen"

Betreuer: Prof. Röhrich und Prof. Stock

1998 Beginn der Promotion bei Prof. Stock

Titel der Dissertation:

"Two pion correlations at the STAR experiment"

Gutachter: Prof. Stock und Prof. Ströbele